

MULTISCALE MODELING AND SIMULATION:
INCORPORATION OF MESOPLASTICITY
BETWEEN ATOMISTIC AND CONTINUUM

By
YANG LIU

MASTER OF SCIENCE
Wuhan University of Technology
June, 2003

BACHELOR OF SCIENCE
Wuhan University of Technology
June, 2000

Submitted to the Faculty of the
Graduate College of
Oklahoma State University
in partial fulfillment of
the requirements for
the Degree of
DOCTOR OF PHILOSOPHY
August, 2007

MULTISCALE MODELING AND SIMULATION:
INCORPORATION OF MESOPLASTICITY
BETWEEN ATOMISTIC AND CONTINUUM

Dissertation Approved:

Ranga Komanduri

Thesis Advisor

Hongbing Lu

Demir Coker

Lionel Raff

A. Gordon Emslie

Dean of the Graduate College

© Copyright

By

YANG LIU

August, 2007

Acknowledgements

Firstly, I want to express my deepest appreciation and thanks to my advisors, Dr. Ranga Komanduri and Dr. Hongbing Lu, for their academic advice, generous financial support for my Ph. D study and invaluable friendship. My sincere appreciation extends to Dr. Demir Coker for his guidance, motivation and friendship. I thank Dr. Lionel Raff for he introduces me the concepts of Molecular Dynamics simulation technique. Other researchers in the multi-scale simulation project, including Dr. Bo Wang and Dr. Samit Roy, and graduate students, have given me considerable help and are highly appreciated. I sincerely thank Dr. M. Yoshino of Tokyo Institute of Technology for discussions and suggestion on the mesoplasticity model. I appreciate Dr. Zhenbing Hou's discussions with me on the metal cutting concept. In addition, I want to thank Dr. Afshin Ghajar, the Director of Graduate Studies in the Department of Mechanical and Aerospace Engineering for his kind concerns for both my study and living. Thanks goes to all the graduate students who have worked with me.

In addition, the support from other faculty members and staff at the School of Mechanical and Aerospace Engineering is deeply appreciated.

The work was supported by a grant from the Air Force Office of Scientific Research (AFOSR) through a DEPSCoR grant (No. F49620-03-1-0281). I thank Dr. Craig S. Hartley, Dr. Jamie Tiley Jr. and Dr. Brett Conner, Program Managers for the Metallic Materials Program at AFOSR through the course of the project for their interest in and support of this work. The work was partly supported by NSF CMS-0555902.

My appreciation goes to my husband, Dr. Jin Ma for his love, understanding and support at times of difficulties as well as his suggestions for my study. My special appreciation goes to my son, Bryan S. Ma for the joy he has brought to our family. I am grateful to my parents and brother for their encouragement and love.

Table of Contents

Chapter	Page
Chapter 1 Introduction	1
Chapter 2 Problem Statement	4
Chapter 3 Combined Numerical Simulation and Nanoindentation for Determining Mechanical Properties of Single-Crystal Copper at Mesoscale.....	9
3.1 Introduction	9
3.2 Mesoplasticity model	13
3.2.1 Fundamentals of mesoplasticity	13
3.2.2 Hardening models of slip systems	19
3.2.3 Numerical implementation	20
3.3 Nanoindentation tests	25
3.4 Combined FEM/nanoindentation approach	26
3.5 Results and discussion.....	28
3.5.1 Nanoindentation	28
3.5.2 Determination of mesoplastic parameters	29
3.5.3 Mechanical behavior of single crystal copper at mesoscale.....	35
3.5.4 Effect of friction on nanoindentation behavior	38
3.5.5 Effect of spherical indenter radius on the mechanical properties of single crystal copper.....	41
3.6 Conclusions	48

Chapter 4 Orientation Effects in Nanoindentation of Single Crystal Copper	51
4.1 Introduction	51
4.2 Literature review	52
4.3 Numerical simulations.....	60
4.4 Experimental setup and test conditions	64
4.5 Results and discussion.....	65
4.5.1 Nanoindentation using a Spherical Indenter.....	66
4.5.2 Nanoindentation using a Berkovich Indenter	76
4.6 Conclusions	80
Chapter 5 Discrete Dislocation Method at the Mesoscale	82
5.1 Introduction	82
5.2 Coupling between the GIMP and DD	85
5.2.1 Numerical formulation	85
5.2.2 Model verification	91
5.3 Coupling of GIMP, DD and MD.....	96
5.3.1 Dislocation detection and passing from atomistic region to continuum region.....	96
5.3.2 Coupling algorithm.....	98
5.4 Multiscale simulation of nanoindentation	103
5.4.1 Simulations at 0° K temperature.....	103
5.4.2 Finite temperature.....	105
5.5 Conclusions	108
Chapter 6 MD Simulations of Atomic Friction	110

6.1 Introduction	110
6.2 MD simulation of friction	112
6.3 Numerical results.....	114
6.4 Conclusions	122
Chapter 7 Conclusions and Future Work.....	124
7.1 Conclusions	125
7.2 Multiscale simulation of orthogonal machining.....	126
7.3 Extension of multiscale simulation to 3D	131
References.....	133

List of Tables

Table	Page
Table 3-1. Hardening matrix of dislocation interaction (Bassani and Wu, 1991).	20
Table 3-2. Material parameters of single crystal copper.....	32
Table 5-1. Material parameters for the discrete dislocation calculations (Cleveringa <i>et al.</i> , 1999)	91

List of Figures

Figure	Page
Fig. 1-1: Schematic of simulations at various levels (Lu, <i>et al.</i> , 2006)	2
Fig. 3-1: Various slip systems of an FCC lattice (Yoshino, 2003)	14
Fig. 3-2: Decomposition of the deformation gradient \mathbf{F} (Yoshino, 2003)	15
Fig. 3-3: The relationship between $\dot{\gamma}^{(k)}$ and $\tau^{(k)}$	17
Fig. 3-4: Algorithm for the user material subroutine	21
Fig. 3-5: Nanoindentation system: MTS Nano XP	25
Fig. 3-6: Schematic of nanoindentation of a single crystal copper	26
Fig. 3-7: FEM mesh used for the nanoindentation simulations	28
Fig. 3-8: Experimental load-displacement curves in nanoindentation	29
Fig. 3-9: Effects of m on the load-displacement curves	30
Fig. 3-10: Effects of τ_{in} on the load-displacement curves	31
Fig. 3-11: Comparison between numerical and experimental load-displacement curves	32
Fig. 3-12: Comparison on the load-displacement curves from nanoindentation test and simulations with various mesh size	34
Fig. 3-13: Stress-strain curve for single-crystal copper at microscale	34
Fig. 3-14: Distributions of out-of-plane displacements at two stages of indentation	35

Fig. 3-15: Comparison of FEM and AFM images of the out-of-plane displacement at an indentation depth of 310 nm.....	36
Fig. 3-16: Shear stress σ_{xz} distributions in the (100) plane at two stages of indentation.....	36
Fig. 3-17: σ_{yy} distributions in the (001) section at two stages of indentation.....	37
Fig. 3-18: Pile-up of the indentation region in the (001) section after unloading	38
Fig. 3-19: Distributions of shear strain (total shear strain on all the slip systems) in the (001) section at two stages of indentation.....	38
Fig. 3-20: Comparisons of the pile-up profiles for different COF at 285 nm indentation depth	39
Fig. 3-21: Load-displacement curves for different COFs	41
Fig. 3-22: (a) Results of simulation showing the variation of mean pressure, P_m with indent radius, a for different indenter radii, R ; (b) Results of simulation showing the variation of the mean pressure, P_m with a/R for different indenter radii.....	43
Fig. 3-23: AFM image of the indent impressions made with a Berkovich indenter.....	44
Fig. 3-24: (a) Results of FEM simulation showing the variation of the indentation force, F with indent diameter, $2a$ for different indenter radii, R ; (b) Results of indentation experiments showing the variation of the indentation force, F with indent diameter, $2a$ for different indenter radii, R	46
Fig. 4-1: Comparisons between numerical and experimental load-displacement curves on copper samples of	

different crystallographic orientations made with a spherical indenter (tip radius 3.4 μm)	67
Fig. 4-2: Distributions of out-of-plane displacements at different orientations on a copper sample using a spherical indenter (tip radius 3.4 μm).	69
Fig. 4-3: AFM images of the indent impressions made on copper workpiece with a spherical indenter (tip radius 3.4 μm) at different crystallographic orientations	70
Fig. 4-4: Shear stress σ_{xz} distributions on the indented planes of different orientations in the indentation of copper	71
Fig. 4-5: Distributions of shear strain (total shear strain on all the slip systems) on the mid-section of the copper workpiece	72
Fig. 4-6: Comparisons of the pile-up profiles of indents made on copper samples with a spherical indenter (tip radius 3.4 μm).....	74
Fig. 4-7: Experimental results on the variation of mean pressure, P_m with a/R on copper samples of different orientations for three spherical indenters of different radii	75
Fig. 4-8: Comparisons between numerical and experimental load-displacement curves for different orientations of copper with a Berkovich diamond indenter	77
Fig. 4-9: Distributions of out-of-plane displacements at different orientations on copper using a Berkovich diamond indenter	78

Fig. 4-10: AFM images of the indent impressions made on copper at different crystallographic orientations with a Berkovich diamond indenter	79
Fig. 4-11: Comparisons of the pile-up profiles of indents made on copper at different crystallographic orientations with a Berkovich diamond indenter	80
Fig. 5-1: Illustration of a dislocation source and a pair of dislocation dipole	89
Fig. 5-2: Flow chart of dislocation dynamics calculation.....	90
Fig. 5-3: Schematic of initial model setup for uniaxial tension.....	92
Fig. 5-4: Distribution of the dislocation sources.....	92
Fig. 5-5: Distribution of the normal stress σ_{xx} at step 50, 000	93
Fig. 5-6: Distribution of dislocations at step 50,000.....	93
Fig. 5-7: Total σ_{yy} field in the tension specimen at step 50,000.....	93
Fig. 5-8: Schematic of initial model setup for bending	94
Fig. 5-9: Distribution of the dislocation sources.....	95
Fig. 5-10: Distribution of dislocations at step 280, 000.....	95
Fig. 5-11: Distribution of the normal stress, σ_{xx} at step 280, 000	95
Fig. 5-12: Passing of atomic dislocations to the continuum region (Shilkrot <i>et al.</i> , 2004).....	98
Fig. 5-13: Illustration of coupled GIMP and MD simulations. The circles represent atoms and the squares (smaller than physical size)	

represent material points. The material points connect to	
each other without a gap to represent the continuum (Ma <i>et al.</i> , 2006)	99
Fig. 5-14: Illustration of the domain decomposition and	
refinement for the coupling simulation of 2D indentation	
using GIMP, DD and MD	100
Fig. 5-15: Flowchart of the coupling algorithm for each increment.....	101
Fig. 5-16: Flowchart for the parallel process of dislocation dynamics.....	102
Fig. 5-17: 2D modeling of an indentation problem with a wedge indenter.....	103
Fig. 5-18: (a) Load-displacement curve using a wedge indenter; (b)-(f)	
Workpiece showing the indent and generation of dislocations at different stage of	
indentation.....	104
Fig. 5-19: Instantaneous temperatures as a function of time	
at different indentation velocities.....	106
Fig. 5-20: Load-displacement curves at different temperatures	
using a wedge indenter.....	107
Fig. 5-21: Slip patterns at different temperatures	
when the indentation depth is 18 Å.....	108
Fig. 6-1: Applied boundary conditions for the MD simulations	
of the atomic friction problem	114
Fig. 6-2: Evolution of the slip pulses over time for $V_{x0} = 0.006$ and $r = 1.6$	115
Fig. 6-3: Comparison of the velocity and energy distributions	
at $V_{x0} = 0.01$ for three break radii, r , namely, 1.2, 1.4, and 1.6	117

Fig. 6-4: Comparison of the velocity and energy distributions	
at $V_{x0} = 0.006$ for three break radii, r , namely, 1.2, 1.4, and 1.6	118
Fig. 6-5: Comparison of the velocity and energy distributions	
at $V_{x0} = 0.004$ for three break radii, r , namely, 1.2, 1.4, and 1.6	119
Fig. 6-6: Comparison of the velocity and energy distributions	
at $V_{x0} = 0.002$ for three break radii, r , namely, 1.2, 1.4, and 1.6	120
Fig. 6-7: Comparison of the velocity and energy distributions	
at $V_{x0} = 0.0005$ for three break radii, r , namely, 1.2, 1.4, and 1.6	121
Fig. 7-1: The sticking-sliding friction law	127
Fig. 7-2: The temperature distribution at the steady state at	
$\alpha = 33^\circ$, $v = 227$ m/min, $t = 0.1$ mm	129
Fig. 7-3: The total contact length and the	
sticking length at the steady state for $\alpha = 33^\circ$, $v = 227$ m/min, $t = 0.1$ mm	129
Fig. 7-4: Schematic of the setup of the orthogonal metal cutting	130
Fig. 7-5: Simulated dislocation microstructure	
(a) Dislocation microstructure developed in copper during	
plastic deformation, as observed in an electron microscope.	
Dark regions contain large number of dislocation lines,	
whereas light regions contain no dislocations.	
(b) Dislocation microstructure developed during plastic	
deformation in a dislocation dynamics simulation	
by ParaDiS (Bulatove, <i>et al.</i> , 2004).	131

Chapter 1

Introduction

Material behavior at all scales spanning from atomistic to continuum involves such processes as elastic deformation, dislocation generation and multiplication, cleavage, void/microcrack formation and their growth into macrocracks, and final failure. In recent times, multiscale modeling has received increasing attention due to its potential linkage between structure-property relationships from nano- to macro-levels (King *et al.*, 1995; Shenoy *et al.*, 1999; Ogata *et al.*, 2001; Smith *et al.*, 2001; Shilkrot *et al.*, 2002). The essence of multiscale modeling of the properties of materials is the ability to develop a description of material behavior on a macroscopic scale from models based on atomic scale or vice versa (Hartley, 2003). Fig. 1-1 is a schematic of the various computer simulation methods used in the development of scaling laws as a function of spatial and temporal variables. At the subatomic level, quantum mechanics or *ab initio* calculations are made to develop the potential-energy functions. With increase in length (or time) scale, material behavior is modeled using molecular dynamics (MD) and Monte Carlo (MC) simulations, then to micro or mesoplastic, and finally to continuum mechanics, such as finite element method (FEM). Mesoplasticity serves as an appropriate formalism that bridges atomistic mechanisms of deformation and fracture to macroscopic behavior. This reinforces the importance of studying the material behavior under mesoscale, which is the subject of this investigation.

This work is primarily focused on developing and applying scaling laws at the mesoscale, including the mesoplasticity formulation and the discrete dislocation technique, as well as applying these methodologies to the framework of multiscale simulations.

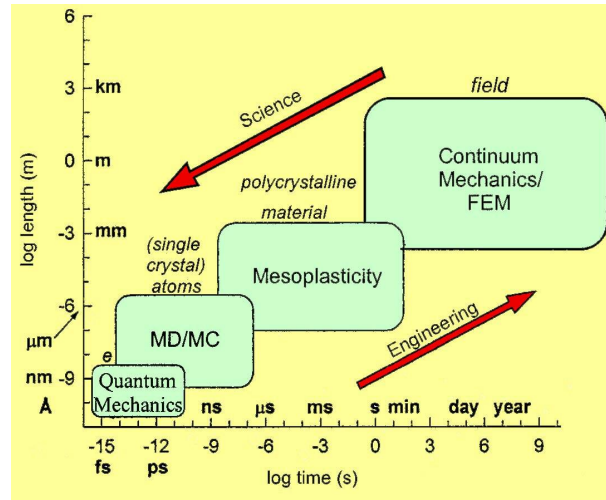


Fig. 1-1: Schematic of simulations at various levels (Lu, *et al.*, 2006)

The thesis is divided into the following seven chapters. Chapter 2 is the problem statement. Chapter 3 describes the combined numerical simulation and nanoindentation method for determining mechanical properties of single-crystal copper at the mesoscale. A mesoplasticity constitutive model for FCC crystals is presented (Yoshino *et al.*, 2001) and validated by comparing nanoindentation simulation results with experimental ones. Chapter 4 presents experimental and numerical results of nanoindentation for different orientations on single crystal copper. The surface patterns after unloading as well as the load-displacement curves from both simulation and experiments are studied. Chapter 5 presents the discrete dislocation method for material simulations at the mesoscale. A multiscale simulation framework coupling the generalized interpolation material point (GIMP) method, discrete dislocations (DD), and molecular dynamics (MD) is described.

Multiscale simulation of nanoindentation in 2D using a wedge indenter is performed and the results are analyzed. Chapter 6 presents the atomic scale friction. Parametric studies on the simulation parameters, including the shearing velocity and break radius are conducted through MD simulations to investigate the frictional behavior at the interface of the two plates. Chapter 7 discusses the general conclusions and future work. Each chapter has an introductory remarks specific to the topic and conclusions of the findings.

Chapter 2

Problem Statement

Scaling laws governing the mechanical behavior of materials from atomistic (nano) to continuum (macro) via mesoplastic (micro), are very important to numerous applications, such as the development of a new class of aircraft engine material, or the manufacturing of numerous components for microelectro-mechanical systems (MEMS), mainly because the information on the mechanical behavior of materials at nanolevel is not presently available as inputs to nanotechnology. Also, for applications where two length scales of different orders of magnitude are involved, it may be possible to extend the knowledge accumulated over time on material behavior at the macro level to the atomistic level, via mesoplastic level.

In this investigation, multiscale modeling and simulations of material properties are addressed considering nanoindentation as an example. This application is chosen because of the extensive use of this technique for determining a wide range of material properties, including modulus, yield strength, and hardness. It may be noted that the scaling laws to be developed would be generic in nature and can be applied to other material processing techniques.

It is well known that many macroscopic phenomena have their origins in the microscopic or even atomistic phenomena. For example, the coalescence of microcracks leading to gross fracture has microscopic origin. Similarly, the tip of a microcrack has its

origin at the atomistic level. The main objective of this investigation is to develop a fundamental understanding of indentation at various scales and develop a computer simulation code that would bridge the gap from atomistic to continuum, via mesoplastic or microscopic behavior. The mesoplasticity model will be implemented in a user-defined subroutine in 3D ABAQUS/Explicit, and a combined FEM/nanoindentation approach will be used to determine the material properties of single-crystal copper in different crystallographic orientations. The anisotropy of single crystal copper will be considered through modeling nanoindentation of single-crystal copper in three orientations, namely, (100), (011) and (111) orientation. Nanoindentation experiments will be conducted and the experimental results will be compared to the numerical results.

Connecting atomistic mechanisms of deformation and fracture to macroscopic behavior requires appropriate formalism that bridges the length scales of these processes over several orders of magnitude. According to Hartley (2003), the essence of multiscale modeling of the properties of a material is the ability to develop a description of material behavior on a macroscopic scale from models based on atomic scale mechanisms or vice versa. Applied to deformation of crystalline materials, this takes the form of translating the behavior of individual dislocations or finite groups into a description of the global response of a mass of material to externally applied loads and displacements. Any such model is subjected to restrictions imposed by the geometry of the crystal lattice, active slip systems, the orientations, and the shapes of grains within the material.

In the case of deformation processes involving discrete number of dislocations that are too small to be described adequately by mesoplasticity models, the question arises as to how one links the atomistic behavior to the macroscopic behavior taking into

account the defect structure. This will be accomplished by including discrete dislocation formulation in which inhomogeneous deformation are treated explicitly by drawing the constitutive input directly from the atomic scale rather than from continuum. Discrete dislocation modeling will be conducted and coupled to continuum scale modeling. When it comes to the interactions of the dislocations, the long-range forces will be modeled by linear elastic fields outside a dislocation core radius of about five Burgers vectors from a dislocation. Within a distance of several Burgers vectors from the core, the short-range interactions of dislocations include the nucleation, immobilization and annihilation and they will be modeled by a set of constitutive rules.

Chapter 3 presents a combined FEM/nanoindentation approach to determine the material parameters of single crystal copper incorporating mesoplastic constitutive model. The 3D FEM model developed in this study is used to simulate nanoindentation on a (100)-oriented single crystal copper with a spherical indenter. Concurrently, nanoindentation tests were conducted on a single crystal copper. Through fitting numerical solution with the experimental load-displacement data, the parameters in the mesoscale constitutive model are determined. Using these parameters, the stress-strain relationship is determined in the uniaxial stress-state at the sub-micrometer scale. The plausible size effect involved in nanoindentation with indenter radii (3.4 μm to 1000 μm) on material hardness is investigated.

Chapter 4 presents experimental and numerical results on nanoindentation of single-crystal copper in three crystallographic orientations, namely, (100), (011) and (111) using a spherical indenter (3.4 μm radius) and a Berkovich indenter. The simulation

results are compared with the experimental results for the load-displacement relationship, the pile-up profiles, and the surface topographies.

Chapter 5 presents the discrete dislocation method, which can effectively model the dislocations and their interactions at the mesoscale. In coupling with continuum mechanics (GIMP), discrete dislocations are assumed to be in the infinite elastic medium. Principle of superposition is used to solve the problem in the domain of interest (van der Giessen and Needleman, 1995). The GIMP and DD coupling will be tested for the case of simple tension and bending problems and then be coupled with MD to formulate a full multi-scale simulation framework. Dislocations from MD simulation can be detected and passed onto the continuum. The coupling algorithm will be used to simulate indentation on Cu (111) plane with a wedge indenter. Dislocation nucleation and subsequent propagation of dislocations will be observed from the indentation simulation.

Chapter 6 presents the modeling of atomic friction between two plates of the same material (model material) at a temperature of 0°K using MD simulations by the pairwise Lennard-Jones (L-J) interaction potential. The interface will be assumed to be atomically smooth and the friction/interaction governed by a break radius that is significantly less than the cut-off radius. Parametric studies on the simulation parameters, including the shearing velocity (V_{x0}) and break radius (r) will be conducted numerically to investigate the frictional behavior at the interface of the two plates.

Chapter 7 presents conclusions and future work. Generic conclusions based on the investigation of nanoindentation at various length scales encompassing atomistic to continuum via mesoplasticity are presented. Two topics are suggested for future work. One is modeling of orthogonal metal cutting using the multiscale simulation model

encompassing MD, DD, and GIMP, which is introduced in Chapter 5. The other one is to extend 2D multiscale simulation algorithm into 3D.

Chapter 3

Combined Numerical Simulation and Nanoindentation for Determining Mechanical Properties of Single-Crystal Copper at Mesoscale

3.1 Introduction

Ductile, single crystal materials are of considerable interest in many applications including micro-electro-mechanical systems (MEMS), optical, and telecommunication systems. Single crystals possess anisotropic material properties that depend on the crystal orientation. The conventional tensile tests are difficult to conduct at nano- and micro-scales to determine orientation dependent behavior. Indentation can be an alternative approach to tension/compression to investigate the mechanical behavior of single crystals. Flom and Komanduri (2002) conducted indentation and scratching experiments on single crystal and polycrystalline materials. They showed marked anisotropies in the slip systems surrounding the indentations depending on the crystal orientation and direction of scratching. Recently, the nanoindentation technique (Oliver and Pharr, 1992) has become a useful tool to determine the mechanical properties of very small volume of material under consideration.

Lim *et al.* (1998) and Lim and Chaudhri (1999) conducted nanoindentation tests to investigate the effect of indenter load (1-100 mN) and radius of the spherical indenter (7 μm , 30 μm , 200 μm , and 500 μm) on the nano and microhardness of polycrystalline work-hardened and annealed oxygen-free copper (OFC) specimens. For the annealed OFC, they reported a gradual increase in normal pressure or Meyer hardness, P_m with

a/R , where a and R are the radii of the indent and the indenter, respectively. A similar variation was observed in the present investigation. Lim *et al.* (1998) also reported that P_m versus a/R data points for indenters of radii 60 μm , 200 μm , and 500 μm all fall on the same curve. The equation for the best fit is given by $P_m = 0.623 (a/R)^{0.498}$. However, for indenters of smaller radii used (7 μm and 30 μm), the P_m values were higher than for the larger indenters (60 μm , 200 μm , and 500 μm). Also, among the two smaller indenters, for a given a/R value, the indenter with the smaller radius gave higher values of normal pressure than for the indenter with the larger radius. From this, the authors concluded that the higher Meyer hardness, P_m indicates a scaling effect for the two smaller radii indenters. For the work-hardened OFC, they reported an initial increase in P_m with a/R , reaching a steady state value beyond a/R of 0.15. They also reported the value of normal pressure, P_m , for a given value a/R to be the same for indenters of radii 200 μm and 500 μm but for 7 μm it was only slightly higher than from 200 and 500 μm . From this, the authors concluded that for nanoindentation and microindentation of work-hardened copper, no scaling effects were found as far as P_m versus a/R relationship is concerned. It will be shown in the present investigation that size effect is not present for a range of indenter radii used for the work-hardened single crystal copper through measurement and simulation. It may also be noted that Lim and Chaudhri (1999) and Lim *et al.* (1998) conducted nanoindentation studies on polycrystalline copper specimens (OFC), both annealed and work-hardened, using a Berkovich diamond indenter as well as spherical indenters of different radii, namely, 7, 30, 60, 200, and 500 μm . In situations where indenter radius was much smaller than the grain size and indentation was made in the

middle of a grain, their results might represent the behavior of a single crystal copper, but each grain is constrained by the adjacent grains. The grain size of OFC was reported to be in the range of 30 to 100 μm . While the 100 μm grains may be adequate for the smaller radii, for example, 7 and 30 μm indenters to justify that indentation was made on a single crystal, for radii larger than this, the boundaries would influence the flow of material so that indentation can no longer be considered to be on a single crystal unless the depth of indent is kept small. Also, as the sample used by Lim and Chaudhri (1999) and Lim *et al.* (1998) is a polycrystalline material, the orientations of grains change from one grain to another and it is not known what the orientation of the sample is for any grain.

Since nanoindentation tests can now be carried out with ease while maintaining accuracy as high as a few μN in load and 0.1 nm in displacement, material characterization at sub-micrometer scale is possible. However, the three-dimensional nanoindentation problem spanning from a sub-micrometer scale to a millimeter scale needs to be solved to determine how the microstructure (crystal orientation, active slip systems, etc.) is linked to the load-displacement relationships.

Mesoplastic constitutive relationships have been investigated by many researchers, including the pioneering works of Hill and Rice (1972) and Asaro and Needleman (1985). Using mesoplastic theory, Peirce *et al.* (1982) analyzed numerically the non-uniform and localized deformation in ductile single crystals subjected to tensile loading. Huang (1991) developed a material user subroutine incorporating mesoplasticity in the ABAQUS implicit program. The theoretical framework of Hill and Rice (1972) has been implemented in the two-dimensional subroutine. Kalidindi *et al.* (1992) developed an implicit time-integration procedure mainly based on the constitutive model of Asaro

and Needleman (1985). Kalidindi *et al.* (1992) simulated the load-displacement curve in plane-strain forging of copper that captures major features of the experimental data. They reported jumps in the calculated curve although no jumps were observed in the experimental data. Yoshino *et al.* (2001) applied mesoplasticity theory in 2D FEM to simulate the dislocation generation and propagation during indentation of single crystal silicon. Kysar (2001) studied the crack growth along a copper/sapphire bi-crystal interface.

With increasing computational power at reducing costs, mesoplastic constitutive relation can be implemented in some FEM codes to solve complex three-dimensional problems. For example, Fivel *et al.* (1998) developed a 3D model to combine discrete dislocations with FEM for nanoindentation simulation on single crystal copper. They, however, did not include the unloading portion of the load-displacement curve and did not compare simulation results with nanoindentation data. Wang *et al.* (2004) studied the dependence of nanoindentation pile-up patterns and micro-textures on the crystallographic orientation on single crystal copper using a conical indenter. They, however, reported an order of magnitude deviation of the numerical load-displacement results from the experimental data. Most of these studies used the material properties of single crystal data obtained from tensile testing at macro-scale. However, it is essential to address these parameters at the submicrometer scale when micro- or meso-scale behavior is of concern. To date, quantitative agreement between the results of mesoplastic/elastic coupling simulation and nanoindentation/micro-tension results does not exist. It is the objective of this investigation to provide this information.

In this chapter, a combined FEM/nanoindentation approach is presented to determine the material properties of single crystal copper incorporating mesoplastic constitutive model. This model is implemented in a user-defined subroutine in 3D ABAQUS/Explicit. The anisotropy of single crystal copper is considered using a linear elasticity model with cubic symmetry at the continuum scale. The 3D multiscale FEM model developed in this study involves both mesoplasticity and elasticity and is used to simulate nanoindentation with a spherical indenter. Concurrently, nanoindentation tests were conducted on a single crystal copper. Through fitting numerical solution with the experimental load-displacement data, the parameters in the mesoscale constitutive model are determined. Using these parameters, the stress-strain relationship can be determined in the uniaxial stress-state at the sub-micrometer scale, or to solve other mesoplastic problems. Using this relationship, we have investigated the effect of indenter radius (3.4 μm to 1000 μm) on material hardness in nanoindentation by FEM simulations.

3.2 Mesoplasticity model

3.2.1 Fundamentals of mesoplasticity

Based on the experimental observations, Taylor and Elam (1923) concluded that the plastic deformation in a face-centered cubic (FCC) crystal is confined into well-defined slip systems. Fig. 3-1 shows the slip systems of an FCC lattice, where the 4 triangles indicate the $\{111\}$ family of slip planes and the 3 arrows on each slip plane indicate $\langle 110 \rangle$ family of slip directions. They form the 12 slip systems that govern the macroscopic distortion of a crystal.

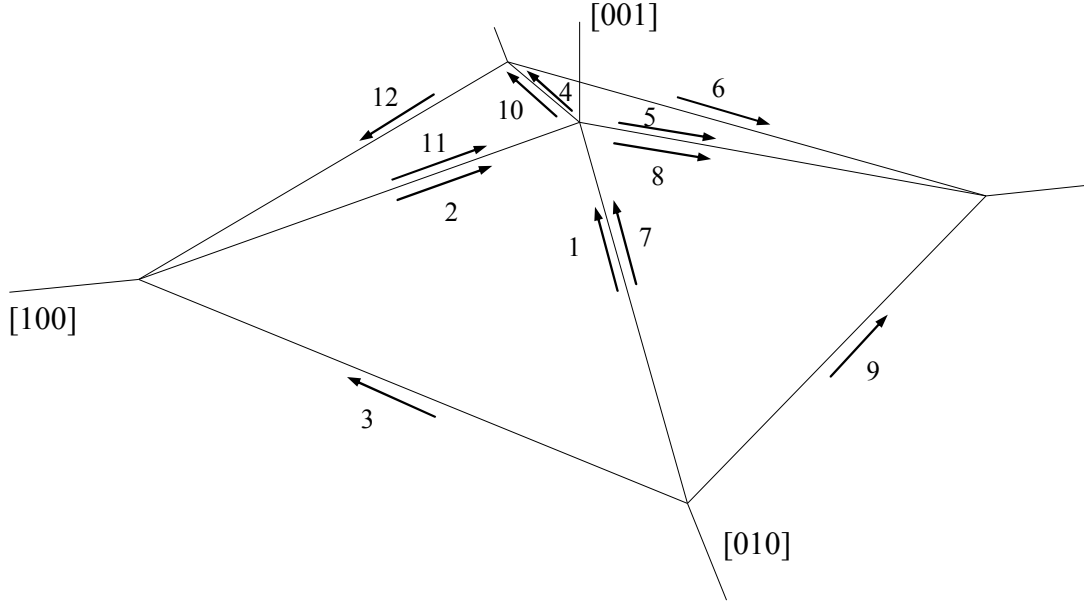


Fig. 3-1: Various slip systems of an FCC lattice (Yoshino, 2003)

The mesoplasticity constitutive theory used in this investigation is a rate-dependent plastic crystallographic theory developed by Peirce *et al.* (1983). The hardening moduli used in this thesis is proposed by Yoshino *et al.* (1997). Standard tensor notation is used throughout the following description. The deformation gradient, \mathbf{F} , can be written in the form,

$$\mathbf{F} = \mathbf{F}^e \mathbf{F}^p \quad (3-1)$$

Considering three stages of deformation of a crystalline lattice as shown in Fig. 3-2, the left lattice represents the initial stage when the lattice is not deformed, and the upper lattice shows the final stage of deformation after the lattice is distorted and rotated by plastic and elastic deformation. The lower right lattice indicates an intermediate stage where the lattice is distorted only by plastic shear deformation. The plastic deformation from the first stage to the intermediate stage is associated with \mathbf{F}^p , and elastic deformation and rotation from the intermediate stage to the final stage is associated with

\mathbf{F}^e . In Fig. 3-2, $\mathbf{n}^{(k)}$ denotes normal vectors of slip plane, and $\mathbf{b}^{(k)}$ denotes those of slip direction, which are the unit Burgers vectors. k is the index of slip system and it varies from 1 to 12. For an FCC crystal, $\mathbf{n}^{(k)}$ and $\mathbf{b}^{(k)}$ are:

$$\mathbf{n}^{(1-3)} = \frac{1}{\sqrt{3}}(1,1,1) \quad \mathbf{n}^{(4-6)} = \frac{1}{\sqrt{3}}(-1,-1,1),$$

$$\mathbf{n}^{(7-9)} = \frac{1}{\sqrt{3}}(-1,1,1) \quad \mathbf{n}^{(10-12)} = \frac{1}{\sqrt{3}}(1,-1,1) \quad (3-2)$$

$$\begin{aligned} \mathbf{b}^{(1)} &= \frac{1}{\sqrt{2}}(0,1,-1) & \mathbf{b}^{(2)} &= \frac{1}{\sqrt{2}}(-1,0,1) & \mathbf{b}^{(3)} &= \frac{1}{\sqrt{2}}(1,-1,0), \\ \mathbf{b}^{(4)} &= \frac{1}{\sqrt{2}}(0,-1,-1) & \mathbf{b}^{(5)} &= \frac{1}{\sqrt{2}}(1,0,1) & \mathbf{b}^{(6)} &= \frac{1}{\sqrt{2}}(-1,1,0), \\ \mathbf{b}^{(7)} &= \frac{1}{\sqrt{2}}(0,1,-1) & \mathbf{b}^{(8)} &= \frac{1}{\sqrt{2}}(1,0,1) & \mathbf{b}^{(9)} &= \frac{1}{\sqrt{2}}(1,-1,0), \\ \mathbf{b}^{(10)} &= \frac{1}{\sqrt{2}}(0,-1,-1) & \mathbf{b}^{(11)} &= \frac{1}{\sqrt{2}}(-1,0,1) & \mathbf{b}^{(12)} &= \frac{1}{\sqrt{2}}(1,1,0) \end{aligned} \quad (3-3)$$

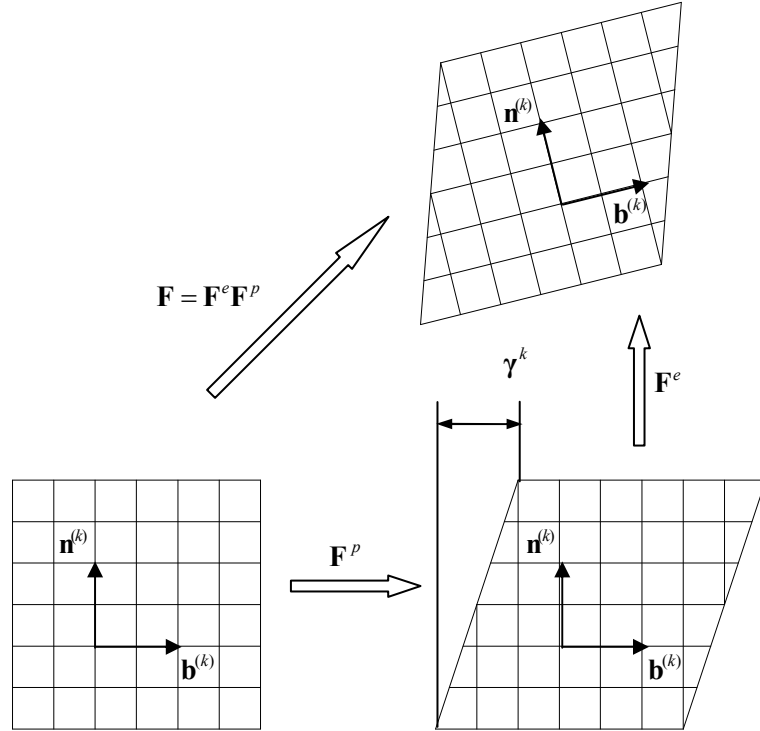


Fig. 3-2: Decomposition of the deformation gradient \mathbf{F} (Yoshino, 2003)

The velocity gradient takes the form:

$$\mathbf{L} = \dot{\mathbf{F}} \mathbf{F}^{-1} = \dot{\mathbf{F}}^e \mathbf{F}^{e-1} + \mathbf{F}^e \dot{\mathbf{F}}^p \mathbf{F}^{p-1} \mathbf{F}^{e-1} \quad (3-4)$$

\mathbf{L} can also be expressed as

$$\mathbf{L} = \mathbf{D} + \mathbf{\Omega}, \quad (3-5)$$

where \mathbf{D} is the symmetric rate of stretching and $\mathbf{\Omega}$ is the skew symmetric spin tensor. \mathbf{D} and $\mathbf{\Omega}$ both can be decomposed into elastic parts (\mathbf{D}^e and $\mathbf{\Omega}^e$) and plastic parts (\mathbf{D}^p and $\mathbf{\Omega}^p$):

$$\mathbf{D} = \mathbf{D}^e + \mathbf{D}^p \quad (3-6)$$

$$\mathbf{\Omega} = \mathbf{\Omega}^e + \mathbf{\Omega}^p \quad (3-7)$$

The elastic parts correspond to elastic deformations and lattice rotations whereas the plastic parts represent the plastic shear slips of the lattice. In the context of the deformation of FCC crystals, \mathbf{D}^p and $\mathbf{\Omega}^p$ are related to the plastic shear strain rate on each slip system given by

$$\mathbf{D}^p = \sum_{k=1}^{12} \mathbf{P}^{(k)} \dot{\gamma}^{(k)} \quad (3-8)$$

$$\mathbf{P}^{(k)} = \frac{1}{2} (\mathbf{b}^{(k)} \otimes \mathbf{n}^{(k)} + \mathbf{n}^{(k)} \otimes \mathbf{b}^{(k)}) \quad (3-9)$$

$$\mathbf{\Omega}^p = \sum_{k=1}^{12} \mathbf{W}^{(k)} \dot{\gamma}^{(k)} \quad (3-10)$$

$$\mathbf{W}^{(k)} = \frac{1}{2} (\mathbf{b}^{(k)} \otimes \mathbf{n}^{(k)} - \mathbf{n}^{(k)} \otimes \mathbf{b}^{(k)}) \quad (3-11)$$

where \otimes indicates the dyadic product of two tensors or vectors, and $\dot{\gamma}^{(k)}$ is the shear strain rate.

When stress $\boldsymbol{\sigma}$ is applied, the resolved shear stress $\tau^{(k)}$ on each slip system can be computed by

$$\tau^{(k)} = \mathbf{P}^{(k)} \boldsymbol{\sigma} \quad (3-12)$$

According to Schmid's law (Schmid, 1931), a slip system will not be activated until $\tau^{(k)}$ overcomes the current shear strength of the system.

$\dot{\gamma}^{(k)}$ in Eq. (3-8) and Eq. (3-10) is expressed as a power-law proposed by Huchinson (1976)

$$\dot{\gamma}^{(k)} = \dot{\gamma}_0 \operatorname{sgn}(\tau^{(k)}) \left| \frac{\tau^{(k)}}{\tau_0^{(k)}} \right|^{\frac{1}{m}} \quad (3-13)$$

where m is the rate sensitivity exponent, $\dot{\gamma}_0$ is shear strain rate at a reference condition and it is the same for all the slip systems. $\tau_0^{(k)}$ denotes the current strength of the slip system. Fig. 3-3 illustrates the relationship between $\dot{\gamma}^{(k)}$ and $\tau^{(k)}$. When $m = 1$, $\tau^{(k)}$ varies linearly with $\dot{\gamma}^{(k)}$. If $\tau^{(k)} < \tau_0^{(k)}$, for a small m , $\dot{\gamma}^{(k)} \rightarrow 0$, as if its slip system is kept inactive. Therefore the equation satisfies the Schmid's law.

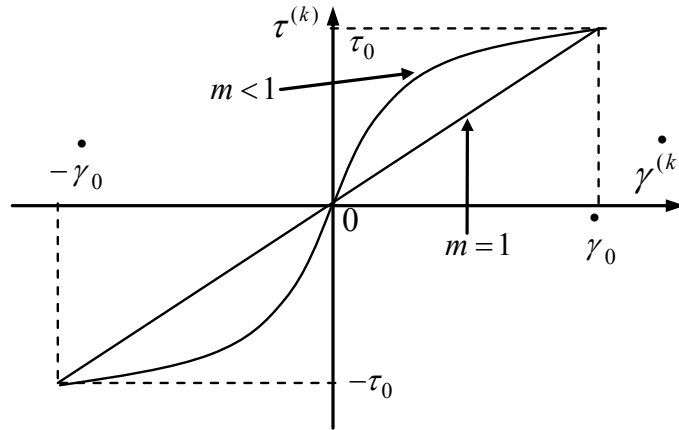


Fig. 3-3: The relationship between $\dot{\gamma}^{(k)}$ and $\tau^{(k)}$

With the assumption that the crystal elasticity is unaffected by slip, the elastic constitutive equation is given by

$$\overset{\nabla}{\boldsymbol{\sigma}}^e + \boldsymbol{\sigma}(\mathbf{I} : \mathbf{D}^e) = \mathbf{C}^e : \mathbf{D}^e \quad (3-14)$$

where $\overset{\nabla}{\boldsymbol{\sigma}}^e$ is the Jaumann rate of the Cauchy stress $\boldsymbol{\sigma}$ and it is a co-rotational stress rate on the coordinate system that rotates with the lattice. \mathbf{I} is the identity tensor. \mathbf{C}^e is the tensor of elastic moduli having the major and minor symmetries, and for cubic crystals it is defined by

$$[\mathbf{C}^e] = \begin{bmatrix} C_{11} & C_{12} & C_{13} & 0 & 0 & 0 \\ C_{12} & C_{22} & C_{23} & 0 & 0 & 0 \\ C_{13} & C_{23} & C_{33} & 0 & 0 & 0 \\ 0 & 0 & 0 & C_{44} & 0 & 0 \\ 0 & 0 & 0 & 0 & C_{55} & 0 \\ 0 & 0 & 0 & 0 & 0 & C_{66} \end{bmatrix} \quad (3-15)$$

To derive the constitutive law on the coordinate system that rotates with the material,

$$\overset{\nabla}{\boldsymbol{\sigma}}^e = \overset{\nabla}{\boldsymbol{\sigma}} + \boldsymbol{\Omega}^p \cdot \boldsymbol{\sigma} - \boldsymbol{\sigma} \cdot \boldsymbol{\Omega}^p \quad (3-16)$$

where $\overset{\nabla}{\boldsymbol{\sigma}}$ is the co-rotational stress rate on the coordinate system that rotates with the material. In this simulation, since the code deals with the metallic materials, volume change by plastic deformation is small compared to the total strain. Hence, $\mathbf{I} : \mathbf{D}^e$ in Eq. (3-14) is negligible. Thus, by combining equations (3-6), (3-8), (3-10), (3-14) and (3-16), the following constitutive equation of mesoplasticity FEM is obtained

$$\overset{\nabla}{\boldsymbol{\sigma}} = \mathbf{C}^e : \mathbf{D} - \sum_{k=1}^{12} [(\mathbf{W}^{(k)} \cdot \boldsymbol{\sigma} - \boldsymbol{\sigma} \cdot \mathbf{W}^{(k)}) + \mathbf{C}^e : \mathbf{P}^{(k)}] \dot{\gamma}^{(k)} \quad (3-17)$$

3.2.2 Hardening models of slip systems

In Eq. (3-13), $\tau_0^{(k)}$ is equivalent to the critical shear stress of the Schmid's law, and represents variation of material strength due to work hardening. It evolves as the material strain hardens. Since work-hardening of slip systems depends on shear deformation, variation of $\tau_0^{(k)}$ is estimated by

$$\Delta \tau_0^{(k)} = \sum_{i=1}^{12} h_{ki} |\Delta \gamma^i| \quad (3-18)$$

where h_{ki} contains the hardening moduli. The diagonal components of h_{ki} represent the self-hardening moduli, whereas the off diagonal ones represent the latent hardening moduli. The hardening moduli used in this thesis was proposed by Yoshino *et al.* (1997) and tested in this investigation. As the hardening rate of a slip system depends on the geometric relationship between the active slip systems, anisotropic hardening rule shown by Eq. (3-19) is used.

$$h_{ki} = \alpha \delta_{ki} + \beta H_{ki} \quad (3-19)$$

where α and β are material parameters.

H_{ki} represents the strength of the obstacles created by dislocation interactions on separate slip systems and they are defined by Table 3-1. It has five independent parameters, taking into account, the interactions of dislocations in various slip systems. In this study, the hardening law has included both self-hardening and latent-hardening of each slip system as well as the interactions of dislocations among different slip systems.

Table 3-1. Hardening matrix of dislocation interaction (Bassani and Wu, 1991).

	1	2	3	4	5	6	7	8	9	10	11	12
1	-	C	C	H	S	G	N	G	G	H	G	S
2	C	-	C	S	H	G	G	H	S	G	N	G
3	C	C	-	G	G	N	G	S	H	S	G	H
4	H	S	G	-	C	C	H	G	S	N	G	G
5	S	H	G	C	-	C	G	N	G	G	H	S
6	G	G	N	C	C	-	S	G	H	G	S	H
7	N	G	G	H	G	S	-	C	C	H	S	G
8	G	H	S	G	N	G	C	-	C	S	H	G
9	G	S	H	S	G	H	C	C	-	G	G	H
10	H	G	S	N	G	G	H	S	G	-	C	C
11	G	N	G	G	H	S	S	H	G	C	-	C
12	S	G	H	G	S	H	G	G	H	C	C	-

(N) no-junction, (H) Hirth lock, (C) coplanar junction, (G) glissile junction, (S) sessile junction. $N = H = C = 8$, $G = 15$, $S = 20$

3.2.3 Numerical implementation

Based on the theory presented in the previous two sections, the mesoplastic constitutive model is implemented in a commercial finite element code (ABAQUS/Explicit), using a user-defined subroutine VUMAT (ABAQUS Manual, 2003). Details of the numerical implementation are described in the following. User-defined mechanical material behavior is provided by means of an interface whereby any mechanical constitutive model can be added to the library and solution-dependent state variables are updated (ABAQUS Manual, 2003). In user subroutine VUMAT all strain measures are calculated with respect to the midstep configuration and all tensor quantities are defined in the co-rotational coordinate system that rotates with the material. When the subroutine is called for blocks of material calculation elements, it is provided with the state variables at the start of the increment (stress, solution-dependent state variables).

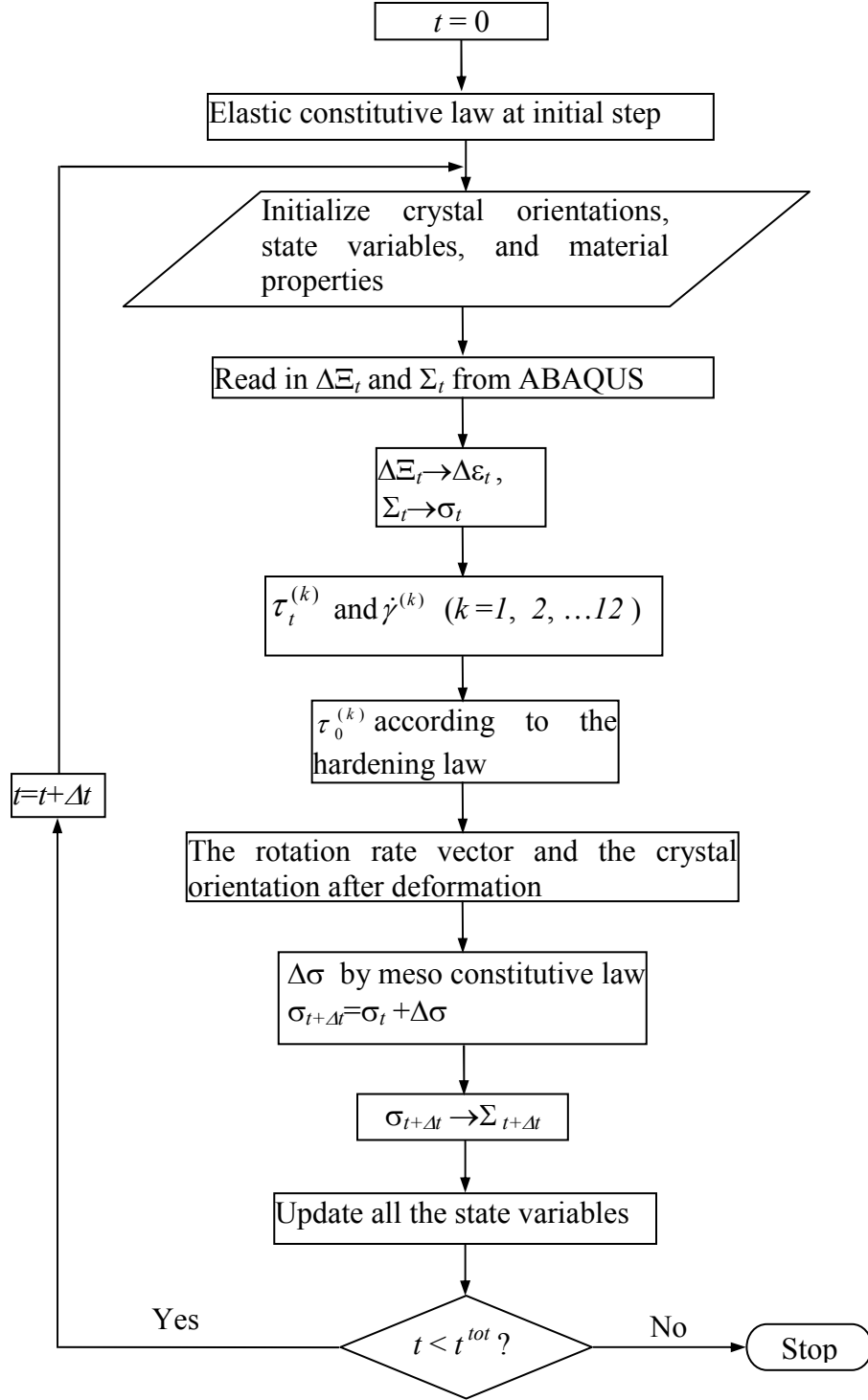


Fig. 3-4: Algorithm for the user material subroutine

Once the calculations within the increment are completed, the values for the new stresses and the new state variables are returned.

The computational scheme used for this subroutine with the mesoplastic constitutive model is shown in Fig. 3-4. To account for arbitrary crystal orientations, two coordinate systems are introduced in the calculation — specimen (global) coordinate and crystalline (local) coordinate systems. The global coordinate system is fixed with the reference configuration. The local coordinate system is aligned with the crystal lattice and rotates in the same way as the lattice. The mesoplastic constitutive calculations are performed in the local coordinate system. In this coordinate system, the incremental stress is computed and transformed into the global system. At the end of each incremental step, the stress and state variables are updated for use in the main program in ABAQUS. Then, the next displacement increment is applied and a new strain increment is generated. This loop is repeated until the computation at all incremental time steps is completed. The detailed steps involved in the computation are given in the following:

Step1: At the beginning of each increment at time t , the crystal orientation, represented by a rotation matrix \mathbf{R}

$$[R] = \begin{bmatrix} R_{11} & R_{12} & R_{13} \\ R_{21} & R_{22} & R_{23} \\ R_{31} & R_{32} & R_{33} \end{bmatrix} \quad (3-20)$$

is initialized in terms of the three Euler angles (ϕ, θ, ψ) , which may be used in order to describe any orientation of the crystal lattice according to Euler's rotation theorem. The first rotation is by an angle ϕ about the z -axis, the second is by an angle θ about the y -axis, and the third is by an angle ψ about the z -axis again.

$$\mathbf{R} = \mathbf{LMN} \quad (3-21)$$

where \mathbf{L} , \mathbf{M} and \mathbf{N} are defined by Eqs. (3-22), (3-23), and (3-24), respectively.

$$[\mathbf{L}] = \begin{bmatrix} -\sin \phi & \cos \phi & 0 \\ -\cos \phi & -\sin \phi & 0 \\ 0 & 0 & 1 \end{bmatrix} \quad (3-22)$$

$$[\mathbf{M}] = \begin{bmatrix} 1 & 0 & 0 \\ 0 & \cos \theta & \sin \theta \\ 0 & -\sin \theta & \cos \theta \end{bmatrix} \quad (3-23)$$

$$[\mathbf{N}] = \begin{bmatrix} \sin \psi & -\cos \psi & 0 \\ \cos \psi & \sin \psi & 0 \\ 0 & 0 & 1 \end{bmatrix} \quad (3-24)$$

In the subsequent steps, \mathbf{R} is used to construct the transformation matrices of the strain and stress between the specimen coordinate and the crystalline coordinate. The material properties of single crystal copper are defined in the ABAQUS input file. During the first step of running, purely elastic constitutive law must be applied for ABAQUS to perform the data checking on the user's constitutive relation. After that, the user defined constitutive model is executed incrementally.

Step 2: The global strain increment $\Delta \Xi_t$, the time increment Δt , global stress Σ_t and the solution-dependent state variables ($\tau_0^{(k)}$, $\gamma^{(k)}$, R_{ij}) are given to the subroutine from the main program in ABAQUS. The user-defined subroutine transforms $\Delta \Xi_t$ and Σ_t to the strain increment $\Delta \epsilon_t$ and the stress σ_t of the crystalline coordinate system in terms of the transformation matrix.

$$\sigma_t = \Psi \Sigma_t \quad (3-25)$$

where Ψ is coordinate system translation matrix defined as:

$$[\Psi] = \begin{bmatrix} R_{11}R_{11} & R_{12}R_{12} & R_{13}R_{13} & 2R_{11}R_{12} & 2R_{12}R_{13} & 2R_{13}R_{11} \\ R_{21}R_{21} & R_{22}R_{22} & R_{23}R_{23} & 2R_{21}R_{22} & 2R_{22}R_{23} & 2R_{23}R_{21} \\ R_{31}R_{31} & R_{32}R_{32} & R_{33}R_{33} & 2R_{31}R_{32} & 2R_{32}R_{33} & 2R_{33}R_{31} \\ R_{11}R_{21} & R_{12}R_{22} & R_{13}R_{23} & R_{11}R_{22} + R_{12}R_{21} & R_{23}R_{12} + R_{13}R_{22} & R_{11}R_{23} + R_{13}R_{21} \\ R_{21}R_{31} & R_{22}R_{32} & R_{23}R_{33} & R_{21}R_{32} + R_{31}R_{22} & R_{22}R_{33} + R_{23}R_{32} & R_{21}R_{33} + R_{31}R_{23} \\ R_{11}R_{31} & R_{12}R_{32} & R_{13}R_{33} & R_{12}R_{31} + R_{11}R_{32} & R_{33}R_{12} + R_{13}R_{32} & R_{11}R_{33} + R_{13}R_{31} \end{bmatrix} \quad (3-26)$$

Then, $\tau^{(k)}$ is computed using Eq.(3-12) and $\dot{\gamma}^{(k)}$ is computed by Eq. (3-13) by looping for all the 12 slip systems.

Step 3: The current strength $\tau_0^{(k)}$ evolves as the slip on the active slip system accumulates and the inactive systems possibly burst out. With the hardening moduli in Eq. (3-19), the incremental strength is evaluated by Eq. (3-18). In Eq. (3-18), $|\Delta\gamma^i|$ is computed by integrating the shear strain rate with respect to the time increment. Since crystal lattice rotates by plastic deformation at the rate of $\mathbf{\Omega}^p$, the crystal orientation tensor after deformation is updated by

$$\mathbf{R}' = \mathbf{T} \cdot \mathbf{R} \quad (3-27)$$

where

$$\mathbf{T} = \mathbf{I} - \mathbf{\Omega}dt - \frac{1}{2}\mathbf{\Omega}^T\mathbf{\Omega}dt^2. \quad (3-28)$$

Step 4: The Jacobian matrix, $\partial\Delta\sigma/\partial\Delta\epsilon$, is computed for the constitutive model by the tangent modulus method. The incremental stress is computed and transformed back to the specimen coordinate system. At the end of the incremental step, the stress (e.g. $\Sigma_{t+\Delta t}$) and state variables are updated and returned to the main program in ABAQUS. Then, the

next displacement increment is applied and the new strain increment is generated. Steps 1 through 4 are repeated until all incremental time steps are completed.

3.3 Nanoindentation tests

An MTS Nano Indenter (XP system) (shown in Fig. 3-5) was used for nanoindentation tests on single crystal copper specimen to obtain load-displacement relationships. The system can reach a maximum indentation depth of 500 μm and a maximum load of 500 mN. The load resolution is 50 nN and the displacement resolution is 0.2 nm. All nanoindentation tests were performed in air at room temperature (23° C). The tests do not start until a thermal equilibrium state is reached and the drift of the indenter tip drops below a set value, typically, 0.05 nm/s. After the indenter tip has made contact with the specimen surface, the indentation load is gradually applied to the surface of the specimen. The indentation load and displacement are recorded simultaneously at a sampling rate of five data points per second. Spherical diamond indenter with a radius of 3.4 μm was used in the nanoindentation tests.

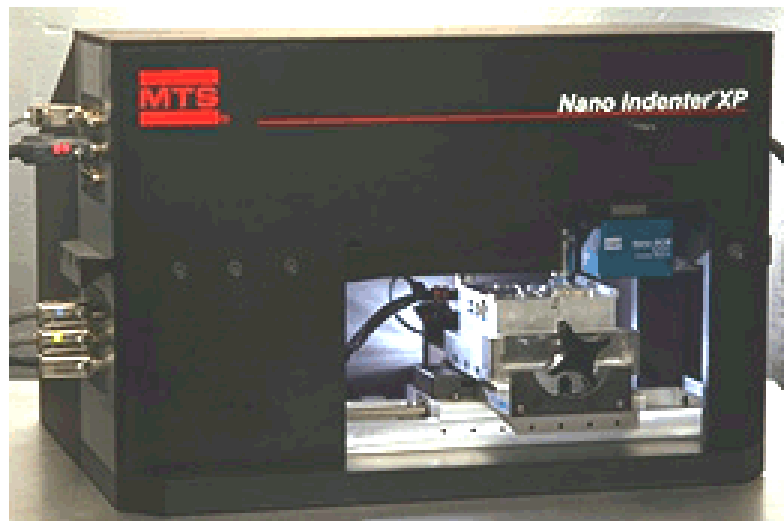


Fig. 3-5: Nanoindentation system: MTS Nano XP

A specimen of single-crystal copper ($10 \times 10 \times 1$ mm) was cut from an ingot using electrical discharge machining (EDM). The surface was chemo-mechanically polished to a surface roughness, R_a of 9.08 nm. Each free surfaces in the specimen corresponds to the $\langle 100 \rangle$ direction, and the upper and lower surfaces are the (100) faces. Fig. 3-6 is a schematic of the nanoindentation setup.

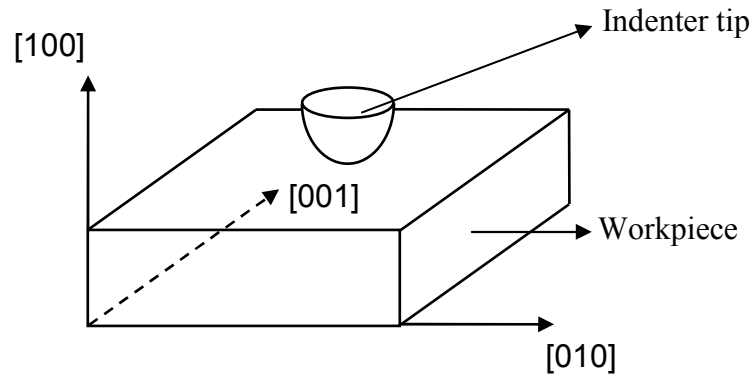


Fig. 3-6: Schematic of nanoindentation of a single crystal copper

3.4 Combined FEM/nanoindentation approach

This section describes the combined FEM/nanoindentation approach used to determine the material properties for single crystal copper incorporating the mesoplastic constitutive model. Various parameters in the mesoplastic model are determined through a fitting procedure that allows good correlation in the load-displacement relationship between the simulation results and the nanoindentation data. Nanoindentation provides the load-displacement curve as well as some basic material parameters, such as Young's Modulus and surface hardness. On the other hand, for a single-crystal copper, the mesoplastic constitutive model and the elastic model are used in the finite element analysis to simulate the nanoindentation tests and to obtain numerical load-displacement relationships. If the load-displacement relationship determined from the numerical

analysis and experiment agrees, the parameters in the mesoplastic model would be suitable for the single-crystal copper.

We next turn to the description of FEM analysis of nanoindentation on a single crystal copper. The size of the workpiece in the FEM model is $15 \times 15 \times 10 \text{ }\mu\text{m}$. Although this is much smaller than the actual dimensions of the specimen used in nanoindentation, it is much larger than the maximum indentation depth ($\sim 300 \text{ nm}$). So, the condition of indentation into a half-space is justified. The 3D finite element mesh is shown in Fig. 3-7 (a). There are 2,688 eight-node brick elements and 3,208 nodes in this model. The size of the smallest elements is 140 nm . Since the primary focus in the specimen is the material directly underneath the indenter, a very fine mesh is used near the indenter tip and a coarser mesh for the remaining region. Fig. 3-7 (b) shows the mesh in the vicinity of the indenter. The dimensions of the nanoindentation involve multiple length scales, which are reflected in the simulations. This is implemented in the simulations using constitutive equations at two length scales, namely, meso- and continuum-scales. Therefore, the workpiece is partitioned into two parts and the corresponding constitutive relationships are assigned. The dimensions of the region where mesoplastic constitutive model is applied are $6 \times 6 \times 10 \text{ }\mu\text{m}$.

The nanoindentation, as shown in Fig. 3-6, is simulated on a single-crystal copper specimen oriented in the $[100]$ direction. The indenter used is a rigid sphere with a radius, R of $3.4 \text{ }\mu\text{m}$. A frictionless contact pair, implemented by two contact surfaces with associated nodes between the indenter and the workpiece is defined. All nodes on the bottom surface of the workpiece are constrained along the $[100]$ direction and a constant velocity is applied to simulate the indenter motion during both loading and unloading.

Since explicit dynamic finite element analysis is conducted, the time step increment is determined based on the smallest element dimension in the mesh and the dilatational wave speed. In this study, a fixed time step increment 60 ps ($1 \text{ ps} = 10^{-12} \text{ s}$) is chosen as a compromise between stability of the dynamic simulation and the overall computational time. A total time step increments of 66,967 in the simulation are used, including loading, intermediate transition, and unloading. The intermediate transition step entails ramping down the velocity to remove the numerical discontinuities in the resistance force caused by the sudden change in the direction of the indenter motion.

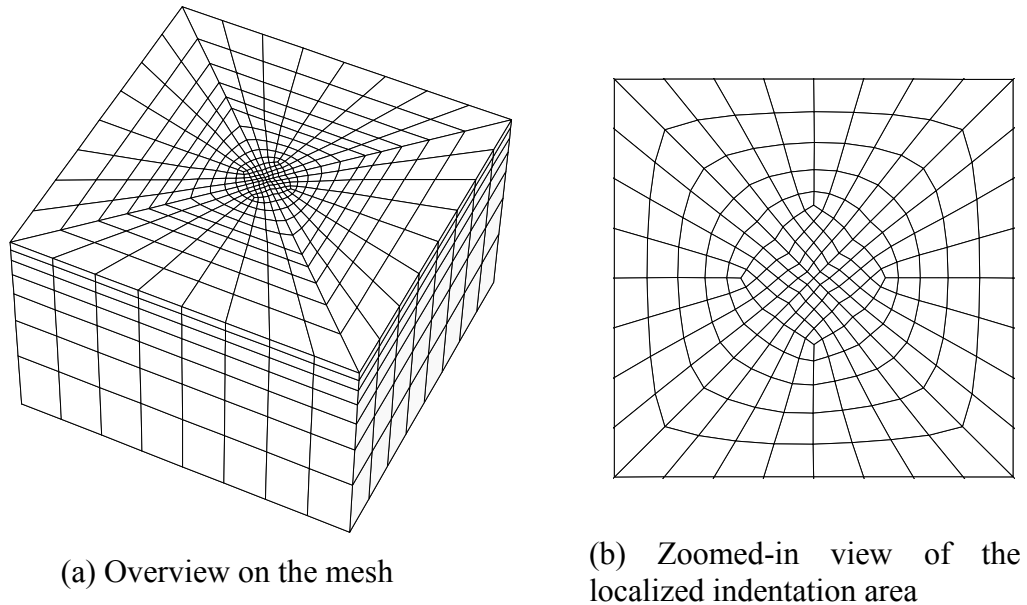


Fig. 3-7: FEM mesh used for the nanoindentation simulations

3.5 Results and discussion

3.5.1 Nanoindentation

The nanoindentation tests were conducted on a single crystal copper specimen. The maximum indentation displacement was 310 nm. For each indentation displacement, nanoindentation tests were conducted at four different locations to ensure repeatability of

the experimental data. The actual load-displacement results are shown in Fig. 3-8. These four curves are very close to each other and the maximum deviation in load at the maximum displacement is 0.07 mN. Loading involves nonlinearity induced by the nonlinear material behavior and increasing contact area (geometric nonlinearity). Unloading is purely elastic. However, as the contact area decreases with decrease in indentation displacement, geometric effects lead to a nonlinear unloading curve.

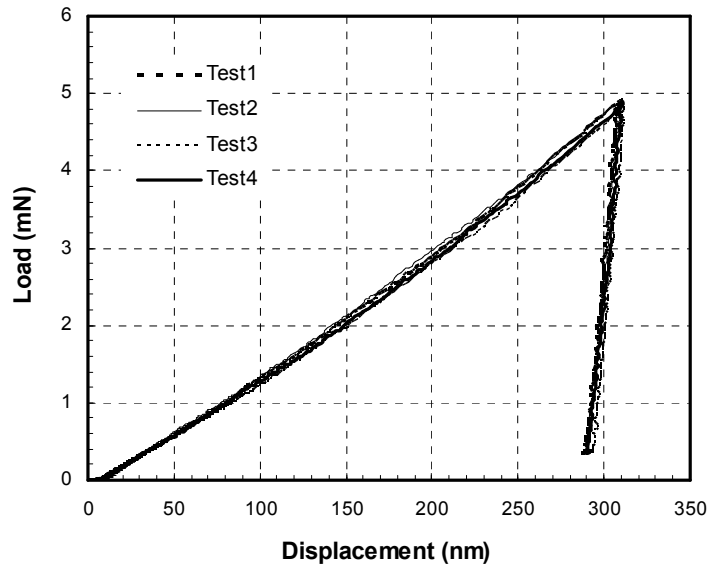


Fig. 3-8: Experimental load-displacement curves in nanoindentation

3.5.2 Determination of mesoplastic parameters

The finite element computational scheme, as described in section 3.2.3, is implemented in ABAQUS and used to model the nanoindentation problem. As stated in 3.2.1, mesoplastic constitutive equations used herein depend on the plastic strain rate, as shown in Eq. (3-13). In the numerical algorithm, m is a numerical parameter that is adjusted to satisfy the Schmid's law. When $m = 0$, Schmid's law is satisfied accurately. However, this condition is difficult to implement in computations due to numerical instability. To resolve this problem, m should be slightly larger than zero, such as 0.02.

With such a small value of m , the shear stress that activates a slip system almost corresponds to the yield shear stress. The condition $m = 1.0$ implies that shear stress $\tau^{(k)}$ is proportional to sliding rate $\dot{\gamma}^{(k)}$. Additionally, in Eq. (3-13), the initial value of the current strength $\tau_0^{(k)}$ is the same in all slip systems and is given as a user input parameter τ_{in} . $\tau_0^{(k)}$ evolves as the material strain hardens. As τ_{in} decreases, the slip system becomes easier to activate. As a result, higher plastic deformation incurs at a given indentation force.

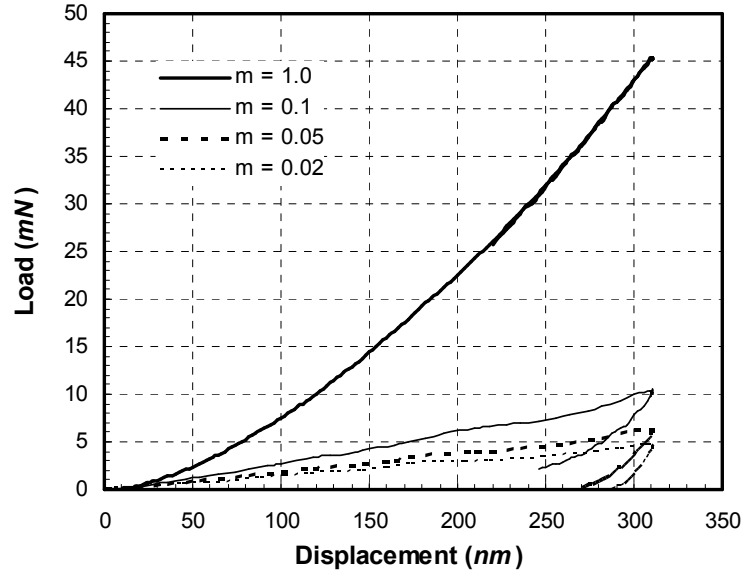


Fig. 3-9: Effects of m on the load-displacement curves

In order to study the effects of m and τ_{in} on the simulated load-displacement curves, serial of simulations were conducted and the results shown in Fig. 3-9 and 3-10. In Fig. 3-9, τ_{in} is kept constant at 34.8 MPa in order to observe the effect of m . For $m = 1.0$, the unloading portion of the load-displacement curve overlaps with the loading portion. As m decreases, the plastic strain rate increases due to lower resistant forces. As

a result, the plastic deformation becomes more pronounced. In Fig. 3-10, m is kept constant of 0.02 in order to observe the dependence of the load-displacement curve on τ_{in} . We use $\tau_{in} = 34.8$ MPa as a benchmark. $\tau_{in} = 52.2$ MPa is equal to one and half times the benchmark value, whereas $\tau_{in} = 69.6$ MPa is two times the benchmark value. Fig. 3-10 shows that the load-displacement curve moves lower as τ_{in} is smaller. This is because the slip system is easier to be activated and hence a larger plastic deformation occurs under a given indentation force. In both Fig. 3-9 and 3-10, the unloading curves are parallel to each other because the unloading is associated with purely elastic recovery.

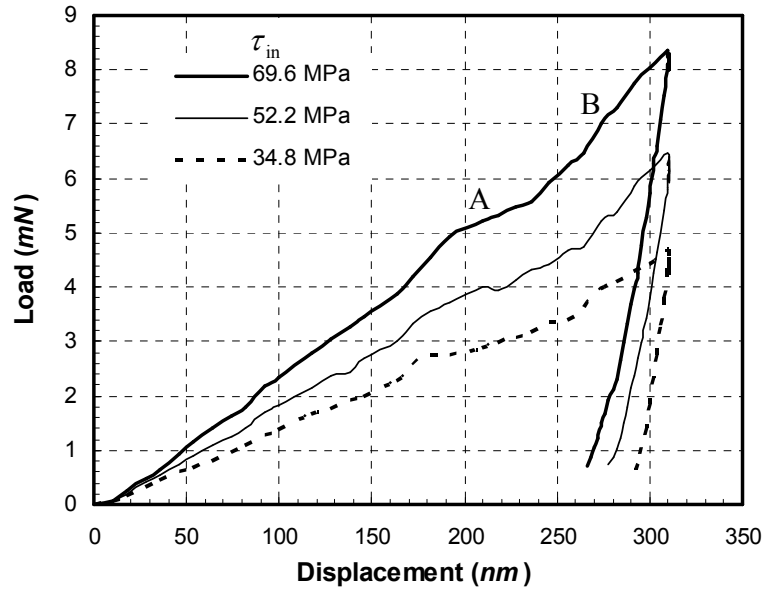


Fig. 3-10: Effects of τ_{in} on the load-displacement curves

Through multiple trial runs, using the parameters given in Table 3-2, a reasonably good agreement between the numerical and experimental load-displacement curves can be achieved as shown in Fig. 3-11. It can be seen that the numerical model has captured major features as well as the magnitude of the experimental data. The resisting force on the indenter increases as the indentation depth increases and drops drastically upon

withdrawal of the indenter. The simulated curve agrees reasonably well with the experimental curve at loading/unloading.

Table 3-2. Material parameters of single crystal copper

C_{11} (GPa)	C_{12} (GPa)	C_{44} (GPa)	τ_{in} (MPa)	$\dot{\gamma}_0$	α (MPa)	β (MPa)	m
145	127.4	75.4	34.8	1.0	4.0	0.6	0.02

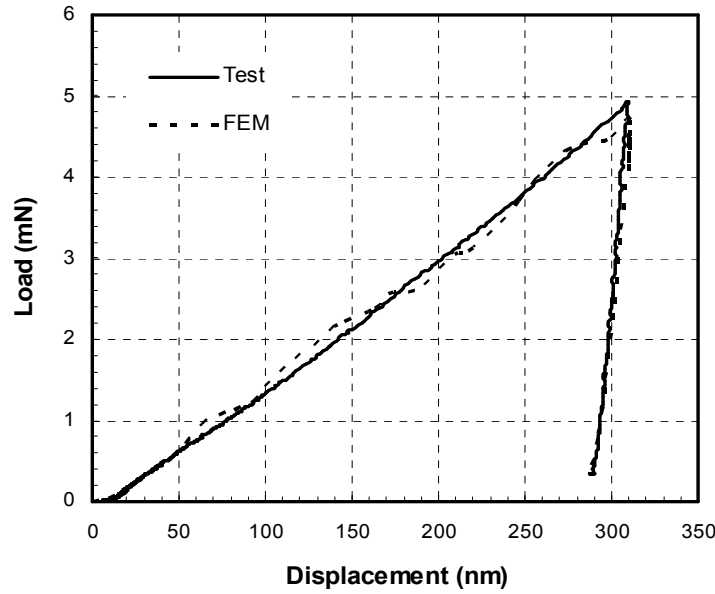


Fig. 3-11: Comparison between numerical and experimental load-displacement curves

Although there is good overall agreement between the experimental and the simulation results, the loading portion of the simulation curve is not smooth, despite various attempts to obtain a smoother curve. While the dynamic characteristics of the simulation might explain partially the bumps in the curve, it cannot explain all, as most portions of the curve are still fairly smooth. It may be noted that similar non-smooth loading curves in indentation were also reported by others (Kalidindi *et al.*, 1992; Smith *et al.*, 2001). Smith *et al.* (2001) attributed this problem to the finite size of the elements. Kalidindi *et al.* (1992) postulated that these jumps can be minimized by using a finer

mesh on the surface of the sample. The jagged load-displacement curve presented here shows a trend similar to what others have observed at the meso-scale. However, further investigation is needed to determine if there is an underlying mechanism for the jagged load-displacement curve, or, if it is only due to computational limitations.

To investigate the sensitivity of the mesh size on the convergence of the numerical solution, the mesh with the smallest element size of 140 nm was used as a benchmark. Three additional mesh sizes, namely, 10% smaller, 10% larger, and 50% larger were tested for the same model and the simulation results were compared. As can be seen from Fig. 3-12, for the case of 50% larger element size (curve Simulation_mesh4), increased oscillations with amplitude of ~ 0.5 mN were observed in the load-displacement curve and the maximum deviation from the benchmark curve (Simulation_mesh1) was 9.3%. For the cases of 10% large (curve Simulation_mesh3), it exhibited the same basic features as the 50% larger one. The 10% smaller curve (Simulation_mesh2) is close to the benchmark curve, and the maximum deviation between the two curves was 5.6%. Based on the sensitivity analysis, it is concluded that the simulation results have converged with respect to the mesh spacing for the benchmark mesh size used.

Additionally, since the current model size is large enough with respect to the nanoindentation depth of 310 nm, only the dimensions of the part with mesoplasticity were changed to test the numerical results. Two different cases, namely, $6 \times 6 \times 10 \mu\text{m}$ and $12 \times 12 \times 10 \mu\text{m}$ were simulated and a maximum error in the load-displacement curves was 6.2%. Based on the sensitivity analysis, it can be concluded that the simulation results

have converged with respect to the mesh spacing for the benchmark mesh size and the model size used.

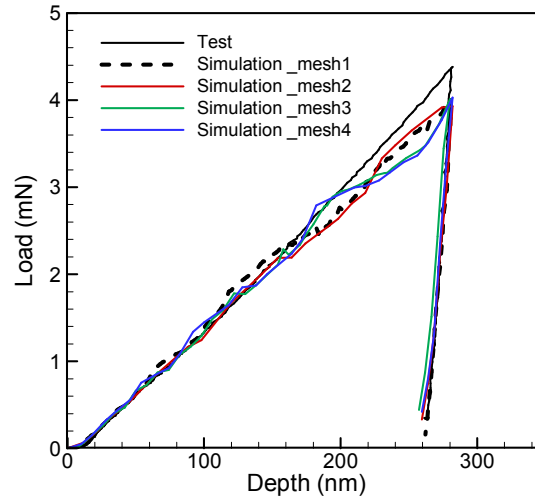


Fig. 3-12: Comparison on the load-displacement curves from nanoindentation test and simulations with various mesh size

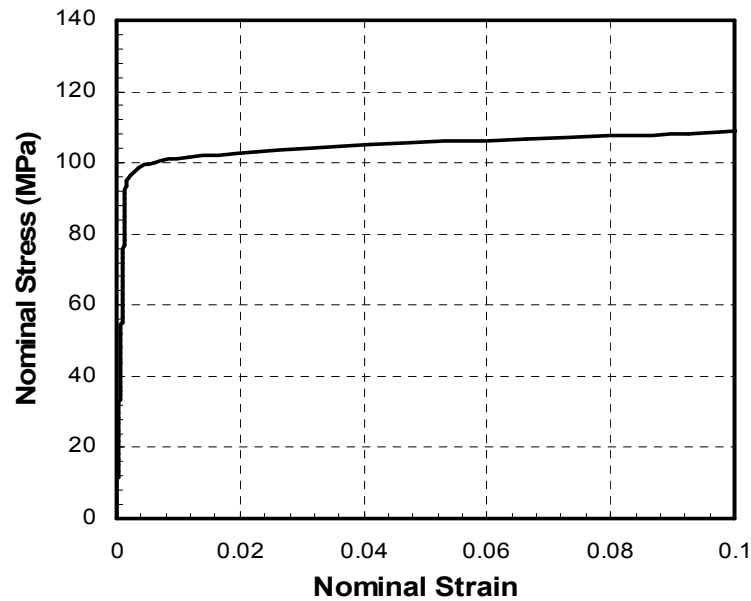


Fig. 3-13: Stress-strain curve for single-crystal copper at microscale

Various parameters obtained using the combined FEM/nanoindentation approach are then employed to determine the stress-strain relationship of single-crystal copper at

the microscale. Fig. 3-13 shows the stress-strain curve of single crystal copper at microscale.

3.5.3 Mechanical behavior of single crystal copper at mesoscale

The nanoindentation simulations were carried out along the $[\bar{1}00]$ direction using a spherical indenter. The parameters in Table 3-2 were used for the mesoplastic constitutive model. Fig. 3-14 (a) and (b) show the distribution of out-of-plane displacement profiles at various stages of indentation. They show the deformation on the (100) orientated surface with a four-fold symmetry. Flom and Komanduri (2002) observed the same deformation patterns in indentation experiments and Wang *et al.* (2004) also reported similar results using conical indenters from FEM simulations and experiments.

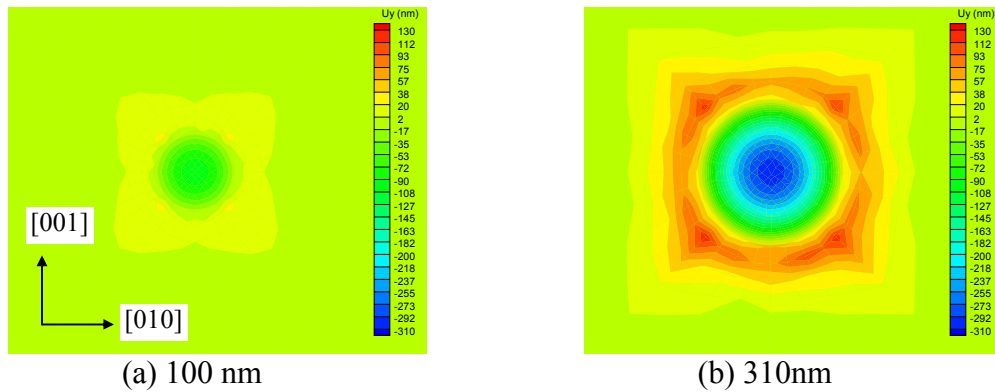


Fig. 3-14: Distributions of out-of-plane displacements at two stages of indentation

Both positive and negative values of displacement can be seen from Fig. 3-14 (a). The positive values occur symmetrically around the indent impression and represent the pile-up patterns of the material. With increase in indentation depth, the pile-ups become more and more pronounced [see Fig. 3-14 (b)]. Fig. 3-15 (a) and (b) show a comparison of the numerical out-of-plane displacement plot and the AFM image after unloading the

indenter. Even though, it is somewhat difficult to precisely capture in the simulations all phenomena observed in experiments both figures show some similar features, for example, a four-fold symmetry. Since self-hardening and latent-hardening for each slip system have already been taken into account in the hardening law, the effect of other active slip systems on the dislocation activities in a lattice have also been included in the simulations. It is also possible that the geometry of the styli may not be exactly spherical, especially with the smaller diameter ones.

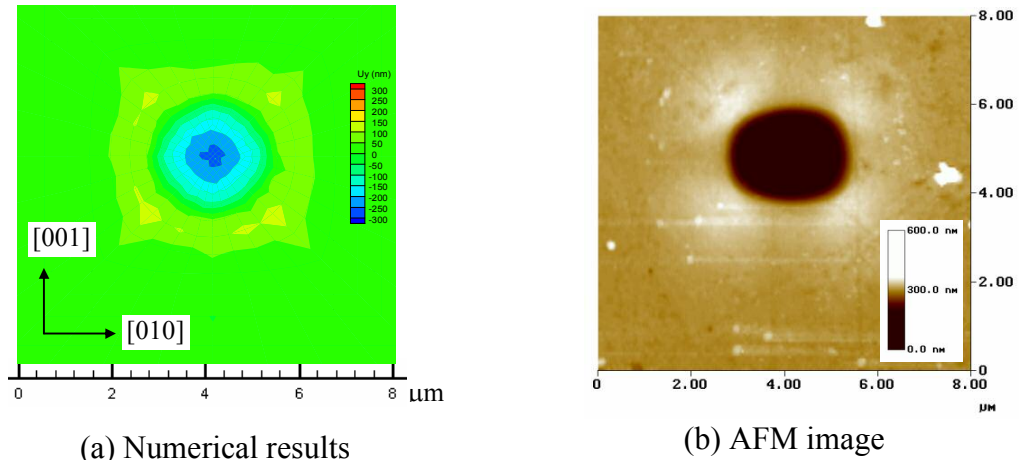


Fig. 3-15: Comparison of FEM and AFM images of the out-of-plane displacement at an indentation depth of 310 nm

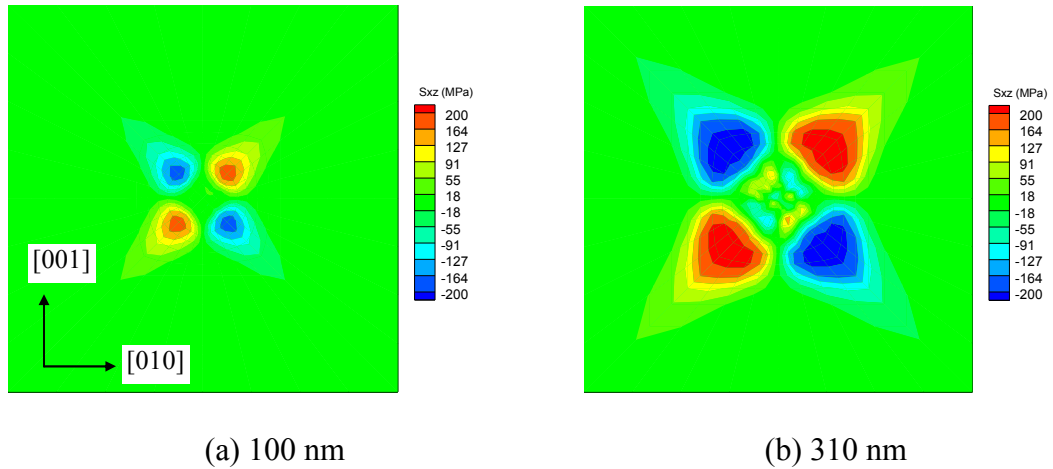


Fig. 3-16: Shear stress σ_{xz} distributions in the (100) plane at two stages of indentation

Fig. 3-16 (a) and (b) show the shear stress σ_{xz} distribution at various stages of indentation. Using a spherical indenter in nanoindentation, the stress waves propagate towards the four vertices in the (100) plane and the stress magnitudes increase with the indentation displacement. Fig. 3-17 (a) and (b) show the distribution of normal stress σ_{yy} (y-axis coincides with the [100] direction) in the mid-section (the normal direction is along [001]) of the single crystal at various stages of indentation. The stress distribution is symmetric with respect to the [100] direction. These figures also indicate that maximum compressive stress occurs right underneath the indenter with its magnitude increasing with indentation depth, and the domain of the compressive stress increases with the indentation displacement. Tensile stress zones become larger and larger with increasing indentation displacement, causing more significant pile-ups.

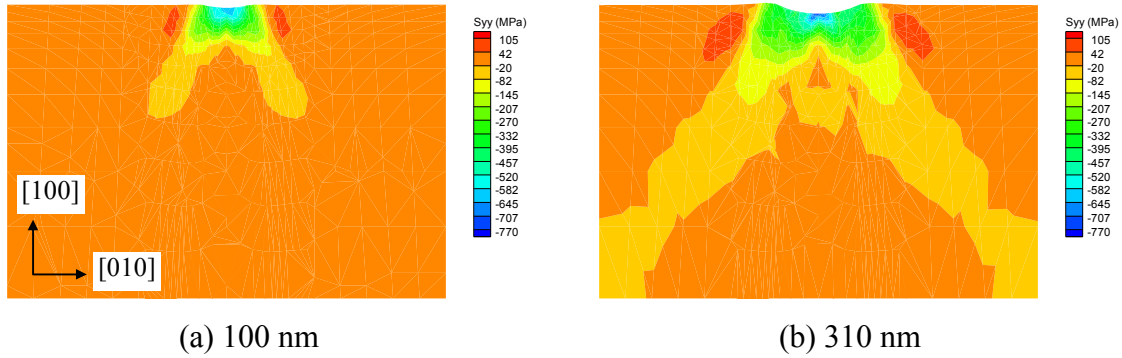


Fig. 3-17: σ_{yy} distributions in the (001) section at two stages of indentation

Fig. 3-18 shows a zoomed-in view of the pile-up on a displacement plot in the same section as that in Fig. 3-17, after unloading the indenter. Fig. 3-19 (a) and (b) show the distributions of the shear strain in the mid section. The total shear strain is calculated using the following equation:

$$\gamma = \sum_k |\Delta \gamma^{(k)}|. \quad (3-29)$$

It may be noted that γ is the shear strain based on the slip systems and it is an indication of the dislocation density. Hence, it should be differentiated from the general shear strain tensor in continuum mechanics. γ is related to the status of each slip system by the Schmid's law, and is associated with the dislocation density as well. As Fig. 3-19 (a) and (b) show, the shear strain distribution is symmetric with respect to the $[100]$ direction.

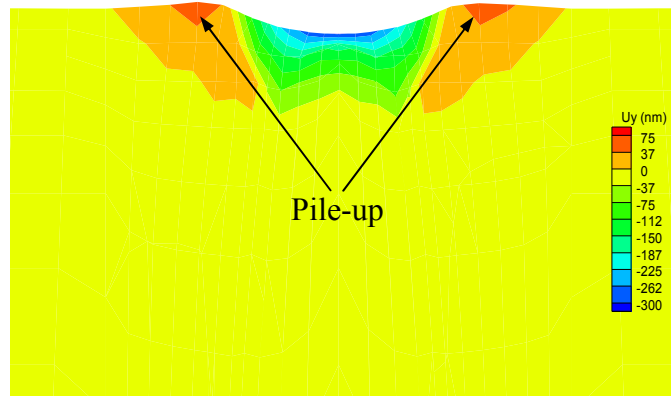


Fig. 3-18: Pile-up of the indentation region in the (001) section after unloading

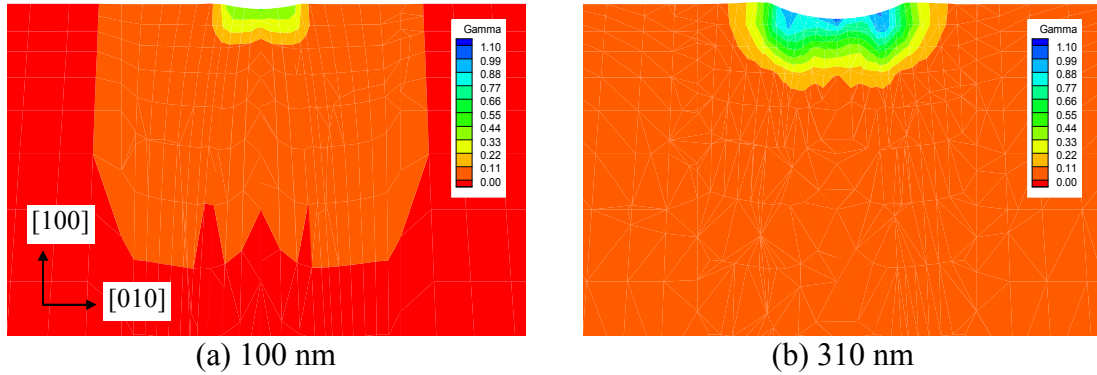


Fig. 3-19: Distributions of shear strain (total shear strain on all the slip systems) in the (001) section at two stages of indentation

3.5.4 Effect of friction on nanoindentation behavior

We now compare the pile-up profiles of the indent between the numerical and experimental data. The dashed line in Fig. 3-20 shows the surface profile scanned through the center of the indentation impression along a line in the $[110]$ direction [as

determined from the AFM image in Fig. 3-15 (b)]. Also shown is the surface profile determined from the numerical analysis for a frictionless contact condition (i.e., coefficient of friction, $\text{COF} = 0$) with the highest material pile-up. It can be seen that the depth of indentation is reasonably in a good agreement with the depth as determined from the AFM image. The material pile-up from the numerical analysis for a COF of zero is 125 nm while the value from the experiment is 60 nm. Even though, the material pile-up is within the same order of magnitudes for both cases, the values differ by a factor of about two. This difference can be attributed partially to friction.

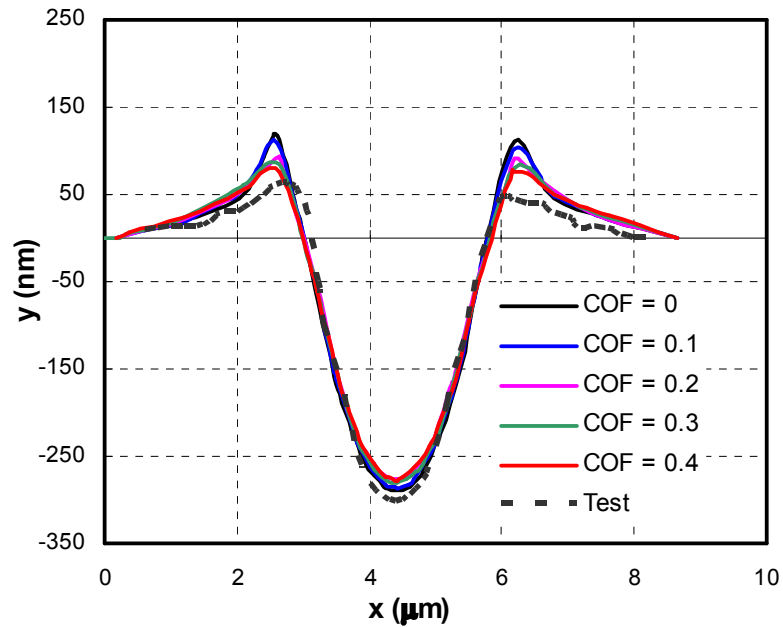


Fig. 3-20: Comparisons of the pile-up profiles for different COF at 285 nm indentation depth

The analysis conducted thus far has focused on a frictionless contact between the nanoindenter and the workpiece. It may, however, be noted that friction does play a role at the contact surface and can affect the surface profile. To investigate this, we introduced Coulomb frictional contact in the FEM simulation of nanoindentation. Because the COF is unknown, we used several values of COFs between $\mu = 0$ and $\mu = 0.8$ in the

simulations, attempting to find a COF that would give us the same surface profile as measured by the AFM. A constant COF is used in each simulation. Fig. 3-20 shows the simulated surface profile in the $[110]$ direction scanned through the center of the impression for COFs between 0 and 0.4. The results indicate that pile-up decreases as COF increases. We also find that as the COF reaches 0.4, further increase in the COF does not cause any additional reduction in the material pile-up. This is most likely because non-slip contact condition has been reached at a COF equals to or near 0.4, so that increasing COF simply maintains the same non-slip contact condition and does not contribute to further reduction in the material pile-up. At COF of 0.4, the simulated material pile-up is 75 nm, close to 60 nm which is the material pile-up measured from AFM. To the best of knowledge of the authors, this difference is small among the published literature at this scale lending further confirmation on the appropriateness of the mesoplastic parameters determined from the combined FEM/nanoindentation approach.

We next address the depth of indentation as shown in Fig. 3-20. It can be seen the indentation depth is constant (~ 285 nm) and independent of the COF. Because the indentation depth is not affected by COF, the load-displacement curve should not be affected by the COF as well. It is seen that the load-displacement curves are almost identical within the range of limited numerical noise (see Fig. 3-21 for COFs between 0 and 0.4). As a result, this combined FEM/nanoindentation approach directed towards finding the mesoscale parameters in single crystal copper through correlating numerical load-displacement curve with the nanoindentation counterpart is not influenced by the COF at the contact surface.

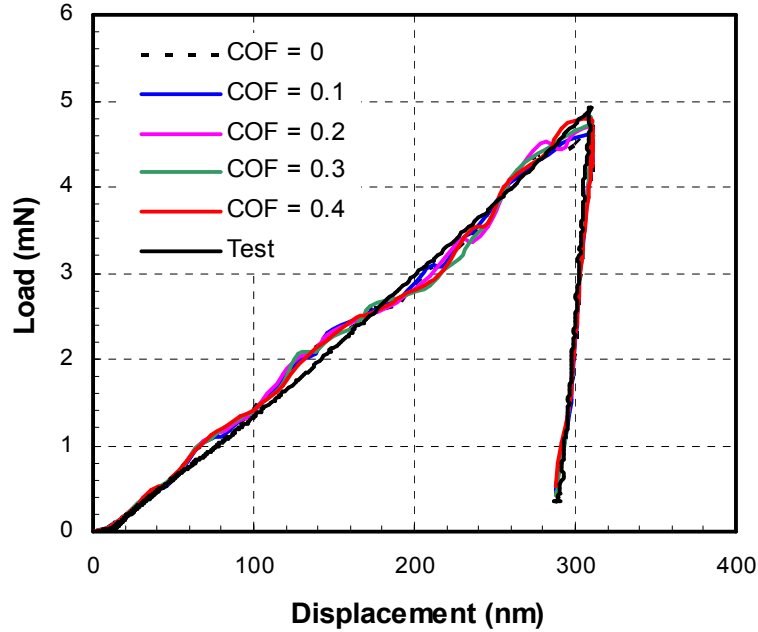


Fig. 3-21: Load-displacement curves for different COFs

3.5.5 Effect of spherical indenter radius on the mechanical properties of single crystal copper

Material parameters determined from nanoindentation tests can be size-dependent, namely, indentation depth and indenter radius. It may be noted that theoretical framework for mesoplasticity used in this investigation does not encompass the size effect. Ideally, it can be applied to any scale of indentation provided the material has the same crystalline characteristics. In reality, however, the nanoindentation size effect may result in changes in the yield stress and the hardening law.

Material hardness, as one of the important mechanical properties, can be measured using the nanoindentation technique with spherical indenters of different radii. To address this problem, numerical simulations were conducted using spherical indenters with different radii (3.4, 7, 10, 25, 50, 100, 200, 500, and 1000 μm) at corresponding indentation depths (310, 638, 912, 2280, 4560, 9120, 18240, 45600, and 91200 nm).

FEM results indicate that pile-up on the indent surface using a spherical indenter with a smaller radius is more evident than with a larger radius. This is because for a given depth of indentation, smaller radii indenters are less blunt than larger radii indenters.

Fig. 3-22 (a) shows the variation of mean pressure, P_m with indent radius, a for different indenter radii, R on a log-log scale. It shows that normal pressure increases with increase in the indent radius. It also shows that this increase is higher for spherical indenters of smaller radii than with larger radii, especially for lower values of the indent radii. Fig. 3-22 (b) shows the variation of mean pressure, P_m with the ratio of the indent radius to the indenter radius, (a/R) for different indenter radii, R . It is seen that a single curve can be fitted for P_m versus (a/R) for different indenter radii, when the indenter depth is normalized with respect to the indenter radius. The best fit equation is given by $P_m = 0.9583 (a/R)^{0.2984}$. The small differences in this case are attributed to the work-hardening behavior of the sample as well as minor numerical instabilities due to mesh distortions. Lim and Chaudhri (1999) found significant differences in the variation of mean normal pressure P_m with (a/R) between the work-hardened and annealed OFC samples. For the work-hardened sample, the P_m value for a given (a/R) is only slightly greater for the indenter of 7 μm radius than for the other two indenters (200 and 500 μm) for which it is the same. The simulation results in this chapter show a similar trend. To confirm the work-hardened behavior of the workmaterial, the indents were scanned under AFM. In general, scanning along a line in a typical AFM image of an indent impression shows pile-up in a work-hardened material and sink-in in the case of an annealed specimen (McElhaney *et al.*, 1998; Lim and Chaudhri, 1999). In the case of single crystal copper in our case, we scanned the surface along a line on an indent, and plotted the

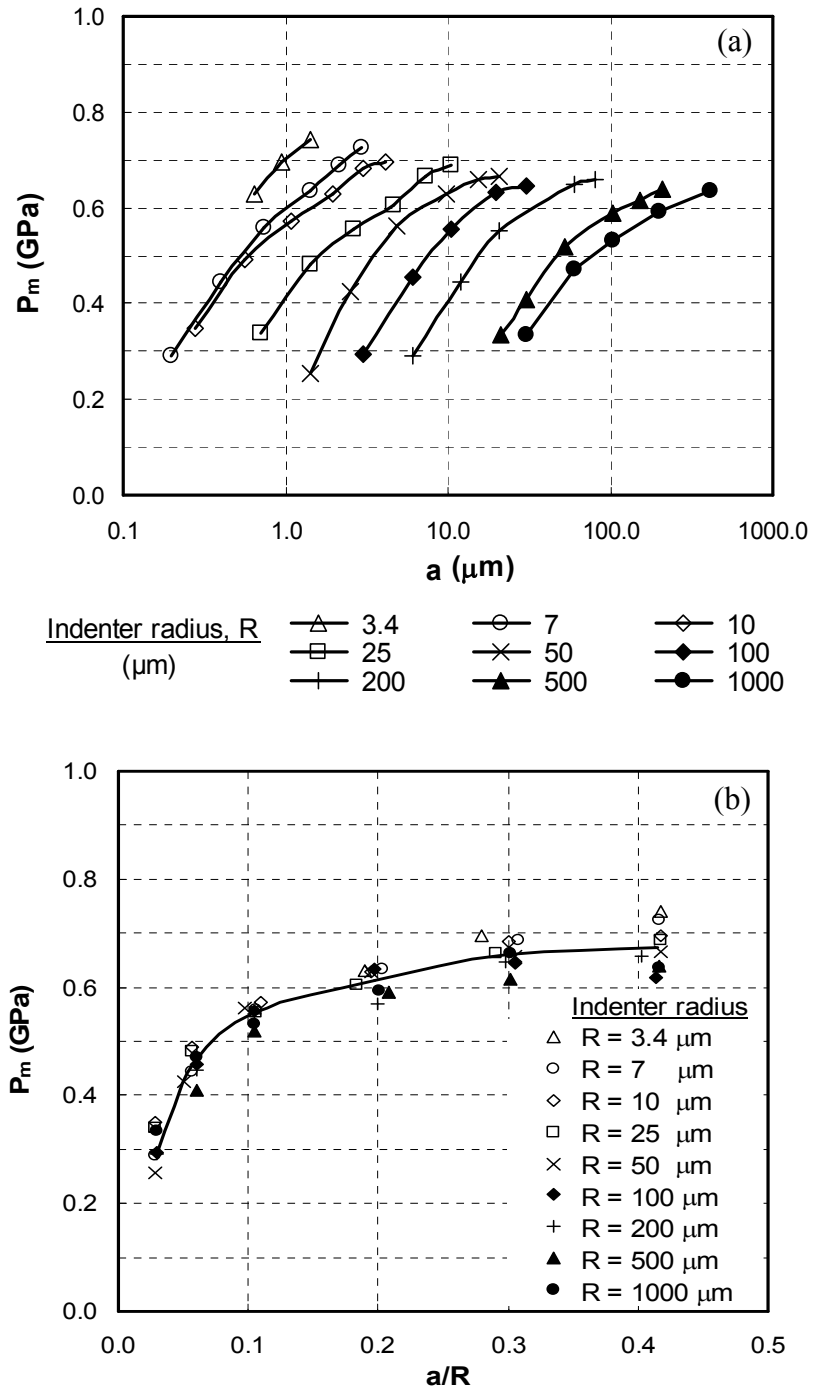


Fig. 3-22: (a) Results of simulation showing the variation of mean pressure, P_m with indenter radius, a for different indenter radii, R ; (b) Results of simulation showing the variation of the mean pressure, P_m with a/R for different indenter radii

height profile in Fig. 3-20. A pile-up is observed around 2.5 μm . Additionally, a pile-up is observed around 4 μm along a line on an indent formed by impression of a Berkovich indenter (Fig. 3-23). The pile-ups in indents formed by both spherical and Berkovich indenter impressions indicate that the single crystal copper used in this investigation is close to work-hardened conditions.

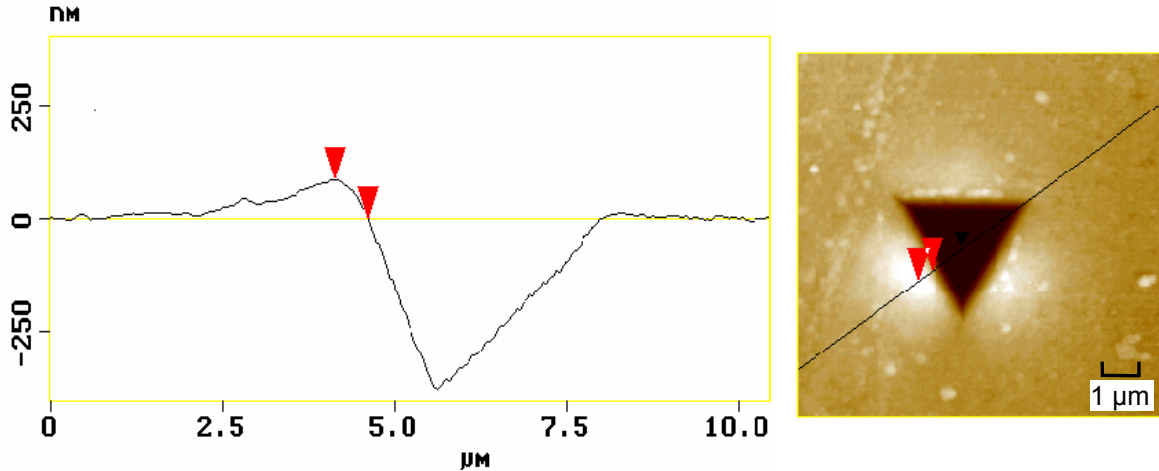


Fig. 3-23: AFM image of the indent impressions made with a Berkovich indenter

In Fig. 3-22 (a) and (b), the variable, indent radius, is involved in both axes. To eliminate this effect, the variation of normal force with indent diameter is plotted on a log-log scale [Fig. 3-24 (a)]. It shows that most of the data points fall on a single line and independent of the indenter radius used (in this case from 3.4 to 1000 μm). A straight line can be fitted between the indenter force and the indent radius. The equation for the best fit is given by $F = 0.4101 (2a)^{2.0359}$, where F is the indenter force and $2a$ is the indent diameter. It is interesting to note that this equation is very similar to the equation normally used at the macrolevel for spherical indenters, namely, $P = A (2a)^n$, where the exponent, n is called the Meyer index (1908). The value of n is reported to vary from 2 for fully strain-hardened metals to 2.5 for annealed metals (Shaw and DeSalvo, 1972).

The value of the exponent, n obtained in the present investigation is 2.0359, indicating the work-hardening behavior of the single crystal copper specimen. Fig. 3-24 (a) shows very little dependence of the indenter radius on the normal force at the microscale, similar to the ones observed at the macroscale. This equation was shown (Krupkowski, 1931) to hold for indenters of diameters in the range of 1-30 mm.

In order to compare the mean normal pressure values obtained from simulations, nanoindentation and microindentation experiments were conducted for several available spherical indenters (3.4, 10, and 500 μm). The nanoindentation tests of spherical diamond indenters (radii 3.4 and 10 μm) were performed on the MTS Nano Indenter XP system, whereas the microindentation tests of spherical tungsten carbide indenter (radius 500 μm) were conducted on a Clark Microhardness Testers (Model CM-700AT). The experimental data are presented in Fig. 3-24 (b). The best fit equation is $F = 0.3867 (2a)^{2.0352}$. The exponent as obtained from the experiment 2.0352 is very close to the simulation, which is 2.0359. From these results, it can be seen that the approach of using combined nanoindentation/FEM simulation for determining mesoplastic model parameters works reasonably well from the microlevel to the macrolevel.

The mesoplastic constitutive law used in this investigation is a mechanism based plasticity model derived from rate-dependent crystallographic theory. It is capable of capturing the effects of crystal orientations. The approach of combining numerical simulation with nanoindentation allowed the determination of the stress-strain relation at mesoscale. Numerical simulations of nanoindentation using appropriate parameters for material behavior at these scales have a reasonably good agreement with the nanoindentation results on indentation mean pressure and surface pileup. It may be noted,

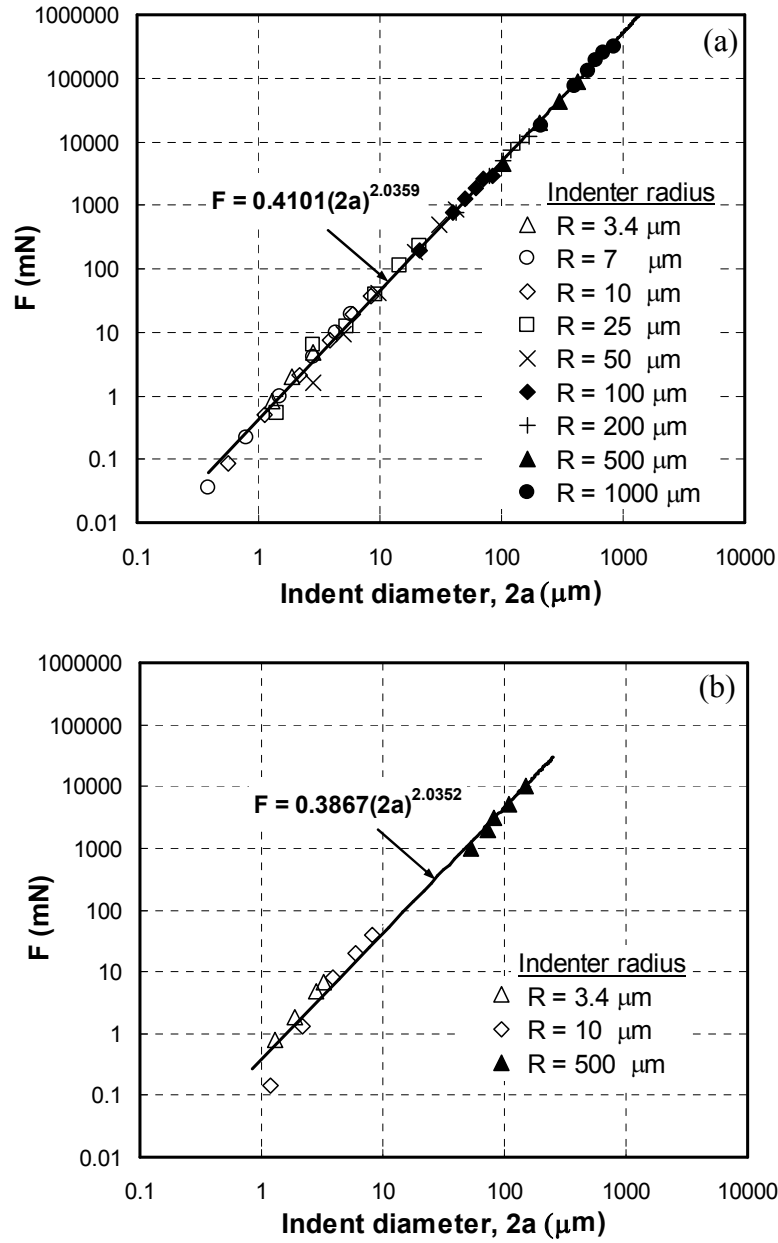


Fig. 3-24: (a) Results of FEM simulation showing the variation of the indentation force, F with indent diameter, $2a$ for different indenter radii, R ; (b) Results of indentation experiments showing the variation of the indentation force, F with indent diameter, $2a$ for different indenter radii, R

however, that the material length scale is not explicitly included in the current mesoplastic constitutive law. Therefore, it is applicable only to problems where size effects do not dominate the material behavior. It is currently, however, not capable of

modeling the size effects, such as the indenter size-dependent mean pressure as reported for annealed polycrystalline copper by Lim and Chaudhri (1999). Within the framework of numerical simulations, the length scale issues can be potentially incorporated. At the continuum level, there are usually three formulations to take into consideration of the size effects (Needleman, 2000): discrete dislocation plasticity, nonlocal plasticity, and coupling of matter diffusion and deformation. In discrete dislocation plasticity (Amodeo and Ghoniem, 1990; Gulluoglu and Hartley, 1993; van der Giessen and Needleman, 1995), the dislocations are modeled as line singularities in an elastic medium. The plastic flow is represented by the collective motion of a number of discrete dislocations. Dislocation based plasticity has a characteristic length, the Burgers vector, and is capable of capturing the size-dependent phenomena. In the nonlocal plasticity theory (Fleck *et al.*, 1994; Nix and Gao, 1998; Shu and Fleck, 1998, Saha and Nix, 2002), the stress tensor or higher order stress tensor depends on both strains and strain gradients. Different formulations for nonlocal plasticity have been presented (see Needleman, 2000 for a review). However, there is no unified formulation in nonlocal plasticity applicable to both single crystals and polycrystalline materials at all length scales. Whether a nonlocal plasticity theory is suitable or not depends ultimately on comparison with experimental data. Consideration of the size-dependence through the coupling of matter diffusion and deformation is usually important at high temperatures, such as the temperatures encountered in the manufacturing process of semiconductor devices. In this case, surface diffusion drives the formation of islands due to the deformation of thin films. Zhang and Bower (1999) found that islands will form if the initial roughness on the surface of the film exceeds certain critical wavelength.

The work presented herein indicates that there is no size-dependence in stress-strain relation, as well as hardness on work-hardened single crystal copper. In situations where size-effects are present, as in the case of annealed copper, size effects need to be introduced in the formulation of numerical simulation.

3.6 Conclusions

1. A multiscale finite element model involving meso-plasticity and elasticity was used for nanoindentation of single crystal copper. A combined FEM simulation and nanoindentation experimental approach was used to determine the parameters for the mesoplastic constitutive model. Nanoindentation tests were conducted to obtain the load-displacement characteristics. The parameters for mesoplastic constitutive model were determined by fitting the numerical load-displacement curves to the experimental data. Numerical results indicate that hardening parameters α and β and initial critical shear stress, τ_{in} have a strong effect on the nanoindentation load-displacement relationship. A reasonably good agreement between numerical and experimental results on the load-displacement relationship was obtained.

2. Meso-mechanical behavior of single-crystal copper was investigated. The distribution of displacements, stresses, shear strains, and shear stresses were analyzed at various stages of indentation. Numerical results show the deformation on the (100) orientated surface in nanoindentation has a four-fold symmetry similar to the AFM image of nanoindentation. This is consistent with the results reported by Flom and Komanduri (2002) and Wang *et al.* (2004).

3. With increase in indentation depth, material pile-up around the indenter also increases. The pile-up was more pronounced with smaller indenter radius. FEM

simulation results also indicate that pile-up decreases as the coefficient of friction (COF) increases from 0 to 0.4, while the nanoindentation load-displacement relationship is found to be independent of the coefficient of friction. Simulated material pile-up at COF of 0.4 compared reasonably well with the measured pile-up. The maximum shear strain associated with the dislocation density occurs underneath the top surface leading to macrocrack formation. Various parameters determined from the combined FEM/nanoindentation are then used to determine uniaxial stress-strain relationships at microscale.

4. The variation of hardness, P_m with a/R shows an increasing trend in hardness with increase in (a/R) and independent of indent diameter. The equation for the best fit is given by $P_m = 0.9583 (a/R)^{0.2984}$. It is interesting to note that this equation is very similar to the equation at the macrolevel for spherical indenters, namely, $P = A (2a)^n$, where the exponent, n is the Meyer index (1908). This equation was shown to hold for indenters of diameters in the range of 1-30 mm by Krupkowski (1931). It is shown in the present investigation that this effect can be attributed to the work-hardening behavior of the material in simulations using spherical indenters of radii varying from 3.4 μm to 1000 μm . Similar results were reported by Lim *et al.* (1998) and Lim and Chaudhri (1999) for polycrystalline work-hardened copper for indenters of radii from 7 to 500 μm .

5. The variation of normal force was found to increase linearly with indent diameter, on a log-log plot, and independent of the indenter radius. The equation for the best fit is given by $F = 0.4101 (2a)^{2.0359}$, where F is the normal force and $2a$ is the indent diameter. The value of n is 2.0359. The range of values of n reported to vary from 2 for fully strain-hardened metals to 2.5 for annealed metals (Shaw and DeSalvo, 1972). The

value of the exponent n obtained in the present investigation is 2.0359, indicating the work-hardening behavior of the single crystal copper specimen. The exponent as determined from experiments is 2.0352 which is also very close to the simulation results.

6. The results of the present investigation [Fig. 3-24 (a) and (b)] indicate that use of combined nanoindentation/FEM simulation approach for determining mesoplastic model parameters works reasonably well from microlevel to the macrolevel.

7. The method presented in this study has provided an approach to determine the microstructural parameters through nanoindentation tests and numerical simulations that can be used for quantitative analysis for a wide range of problems involving mesoplastic behavior.

Chapter 4

Orientation Effects in Nanoindentation of Single Crystal Copper

4.1 Introduction

Nanoindentation technique has become an extremely useful tool for determining the mechanical properties of very small volume (small size) of materials, such as the structural elements used in MEMS applications (e.g. microgears, microshafts, microconnectors) and thin films/coatings on various substrate materials (Oliver and Pharr, 1992). It can provide such valuable information as nanohardness, yield stress, and elastic modulus of materials comprising of extremely small volumes. Nanoscratching can provide additional information on friction, which is of importance in tribology. Nanoindentation can also provide load-displacement behavior as well as the onset of plastic flow, which plays a significant role in microscale deformation processes involved in adhesion, friction, and inelastic deformation.

A major deformation feature in nanoindentation is the material's strain hardening characteristics, which translates into pile-up or sink-in of the material around the indent (Gouldstone *et al.*, 2000; Wang *et al.*, 2004). As nanomechanics continues to be in the center of focus, the determination of the mechanical properties of materials at the nanometric level assumes significance. Nanoindentation technique is one method for addressing this issue.

4.2 Literature review

Nanoindentation has been extensively studied (analytical, numerical, and experimental) in view of its ability to determine mechanical properties of materials in small volumes. The experimental studies include, determination of plastic strain and strain gradients at very small indentation depths (Tymiak *et al.*, 2001), nonlinear deformation mechanisms during nanoindentation (Bahr *et al.*, 1998), discrete and continuous deformation during nanoindentation of thin films (Gouldstone *et al.*, 2000), nano- and micro-indentation studies on polycrystalline OFHC copper (both annealed and workhardened) using spherical indenters of different radii to investigate the scaling effect (Lim *et al.*, 1998; Lim and Chaudhri, 1999), dislocation structure involved in nanoindentation (Gaillard *et al.*, 2003), identification of slip systems around indentation (Nibur and Bahr, 2003). The simulation studies include, nanoindentation and incipient plasticity using large-scale atomic simulations using the quasi-continuum method (Shenoy *et al.*, 1999), computational mechanics at the mesoscale (Needleman, 2000), theoretical investigation of plasticity at the micrometer scale (Hutchinson, 2000), MD simulations of anisotropy in nanoindentation (Christopher *et al.*, 2003), size-dependent hardness or indentation size effect (ISE) due to the presence of geometrically necessary dislocations or strain gradient effects in polycrystalline aluminum using nanoindentation (Xu and Rowcliffe, 2002; Elmustafa and Stone, 2003a, b), strain bursts and creep in aluminum during nanoindentation (Feng and Ngan, 2001), and length scale effects on the mechanical behavior due to strain gradient plasticity (Duan *et al.*, 2001).

Conventional plasticity theories do not include material length scale in their formulation (Hutchinson, 2000). Hence, they cannot handle any size effect. A natural

way of including size effect in the constitutive equations is to postulate that yield stress depends not only on strain (as in conventional plasticity) but also on the strain gradient. Fleck and Hutchinson (1993) developed a phenomenological theory to take into account, the strain gradient effects in plasticity, using a single, constant, material length scale within the general framework of couple stress theory. To explain for the plausible size effect, especially in the submicrometer depth regime, Fleck *et al.* (1994) showed that large strain gradients inherent in small indentations can lead to geometrically necessary dislocations that can cause enhanced hardening. Begley and Hutchinson (1998) applied the deformation version of the strain gradient plasticity theory to model materials undergoing nano/micro-indentation to assess its applicability by comparing the analytical results with the experimental.

Poole *et al.* (1996) explained the size dependence of hardness in micro/nano indentation using a dislocation model that incorporates geometrically necessary dislocations due to the presence of strain gradients in the deformation zone around the indent. Nix and Gao (1998) modeled the indentation size effect for crystalline materials through the consideration of geometrically necessary dislocations. They used this model to derive a mathematical relationship for strain gradient plasticity and compared it with the nanoindentation results published in the literature showing reasonably good agreement.

Some studies have recently been reported on the anisotropy associated with nanoindentation of single crystal materials of different crystallographic orientations (Groenou *et al.*, 1989; Khan *et al.*, 1992; Stelmashenko *et al.*, 1993; Lim and Chaudhri, 2002; Flom and Kmanduri, 2002; Komanduri *et al.*, 2000; Christopher *et al.*, 2003; Nibur

and Bahr, 2003; Wang *et al.*, 2004; Peralta *et al.*, 2004). In view of their relevance to the present investigation, they will be reviewed briefly.

Groenou *et al.* (1989) investigated slip patterns on a single crystal MnZn ferrite workpiece by spherical indentation on three crystallographic planes [(100), (011), and (111)]. They reported that on all planes investigated, the deformation consists of slip lines, when the shear stress is higher than a threshold value. At higher loads, they report formation of new lines that appeared to couple with the initially generated slip lines. At even higher loads, the formation of cracks was reported. They discussed the slip patterns for {100}, {111}, and {110} slip systems in terms of the Burgers vector along $\langle 110 \rangle$. The experimental results were compared with the analytical results on the basis of elasticity equations for a half-space loaded by a sphere. Analysis in the plastic regime was not provided in their work.

Khan *et al.* (1992) investigated the formation behavior and hardness in indentation of a single crystal MgO on (100), (011), and (111) using a Vickers diamond pyramidal indenter and a spherical cemented tungsten carbide indenter (0.4 mm diameter). They investigated the plastically deformed zone around the indents using cathodoluminescence (CL) and showed that crystal orientation has a marked influence on the indentation crack patterns. They also found that hardness depends on the geometry of the indenter and the crystallographic plane in which the indentation was made. They made an attempt to explain for the difference in terms of material flow and dislocation interactions of various slip systems.

Stelmashenko *et al.* (1993) conducted microindentations on (100), (011), (111) surfaces of single crystals of W and Mo using a scanning tunneling microscope (STM).

They found that formation of pile-up in W and Mo single crystals is determined by the geometry of the BCC crystal slip systems. They also found that the spatial distribution of the deformation depends on the crystallographic orientation of the surface. Their results indicate that STM enables the amount of plastic deformation to be quantified accurately even for small indents.

Lim and Chaudhri (2002) investigated microindentation hardness of individual grains of [(110) and (111) orientations] on a polycrystalline copper using a cemented tungsten carbide spherical indenter of radius 200 μm . They determined that the indentation hardness values of (individual grains in polycrystalline) of copper of different orientations are very similar and any differences in the orientation of contiguous grains would not affect the hardness values of polycrystals significantly.

Recently, Flom and Komanduri (2002) reported results of indentation and sliding experiments on a wide range of single crystal and polycrystalline materials (FCC, BCC, and HCP) at microscale using a modified microhardness tester. Optical microscopy was used to characterize the specimens after indentations. On a copper specimen, an FCC metal, plastic deformation takes place predominantly along $\{111\}$ slip planes and along the $\langle 110 \rangle$ slip directions. Thus, a 4-fold symmetry is expected when an FCC crystal was indented on a (100) plane. Similarly, when the copper crystal was indented in (011) and (111) planes, 2-fold and 3-fold symmetries are expected. Experimental results of indentation on these faces have confirmed these features. Both the size and shape of the indentations gave rise to slip lines surrounding the indentations, revealing marked anisotropies on different crystallographic orientations. These results were also found to

be in agreement with the molecular dynamics simulation results of Komanduri *et al.* (2000). The present investigation is an extension of that work at the meso scales.

Christopher *et al.* (2003) investigated the anisotropy of nanoindentation in a single crystal copper {110}. They showed that pile-up patterns in nanoindentation are indicative of the sample symmetry. They conducted both experimental and MD simulations to determine the atomistic mechanisms underlying the anisotropy. Their simulations showed that dislocation loops start from the nanoindenter tip and end on the crystal surface, propagating outwards along the four in-plane $\langle 111 \rangle$ directions. These loops carry material away from the indenter and form lumps on the surface along these directions separated by the pile-up of material around the indent. Atoms also move in the two out-of-plane $\langle 111 \rangle$ directions, causing propagation of subsurface defects and pile-up around the indent.

Nibur and Bahr (2003) conducted indentation testing, followed by AFM and orientation imaging microscopy (OIM) observations to identify slip planes on which dislocations emerge at the free surface around indentations. They found that the patterns of slip steps around the indentations are predictable and repeatable. They reported that for the FCC materials tested these patterns depend mostly on the crystal orientation, and that the stacking fault energy and slip mode affect the planarity of any given step.

Wang *et al.* (2004) reported results of a study similar to the work presented in the current investigation. They conducted nanoindentation studies using a conical indenter on single crystal copper specimens of three different orientations, namely, on (011), (100), and (111) faces. They investigated the orientation dependence of nanoindentation pile-up patterns and reported a two-fold, four-fold, and six-fold symmetry on (011), (100), and

(111) faces, respectively. They also conducted simulations using a 3D elastic-viscoplastic crystal plasticity FEM, which takes into account the crystallographic slip and orientation changes during indentation. They reported an order of magnitude difference between the experimental and simulation results of the load-displacement relationships. They offered several plausible reasons for this discrepancy, including: 1. simulations were conducted with much larger indenters than experiments, 2. differences in the real tip radius, 3. geometry difference between actual and simulated indenters, 4. nanoindentation experiments were conducted using the force control mode while simulations were conducted in the displacement control mode, 5. mesh effects in FEM and associated problems, 6. influence of the constitutive law used, and finally, 7. unknown frictional conditions.

Wang *et al.* (2004) also found that most of the patterns around the indents are pile-up rather than sink-in. They attributed this to the highly crystallographic and localized flow of material only along small volumes. They concluded that in these confined zones only little microscopic strain hardening occurs due to parallel slip promoting pile-up instead of sink-in behavior. The present investigation (both numerical and experimental) confirms the findings of Wang *et al.* (2004) on the pile-up (instead of sink-in) and some other issues, such as pile-up patterns.

Peralta *et al.* (2004) investigated the deformation surrounding Vickers indents in copper for two orientations of the indenter diagonals using optical, electron-beam, and scanning probe microscopes. They reported that both sink-in and pile-up behavior depend on in-plane crystallographic orientations rather than the orientation of the indenter.

Regions with multiple slips show larger lattice rotations and sink-in whereas regions with lower slip density have smaller lattice rotations and show pile-ups.

Considerable attention has been devoted recently to simulations of nanoindentation on single crystals (Kalidindi *et al.*, 1992; Fivel *et al.*, 1998; Smith *et al.*, 2001; Zimmerman *et al.*, 2001; Zhu *et al.*, 2004; Saraev and Miller, 2006). However, investigations on the effects of crystallographic orientations on the nano-mechanical behavior, including load-displacement relationship and deformation topography, are limited. Molecular dynamics (MD) simulations have been used to investigate the anisotropic features in nanomechanical properties on the surfaces of nickel single crystals as a function of indenter size and velocity for three crystallographic orientations: $\langle 100 \rangle$, $\langle 110 \rangle$ and $\langle 111 \rangle$ (Kum, 2005). The results showed the dependency of anisotropic elastic-plastic deformation on the indenter size, velocity, and crystal orientation. MD simulations (Liang *et al.*, 2004; Tsuru and Shibutani, 2007) were used to study the crystal plasticity in nanoindentation by comparing the elastic-plastic response of three copper substrates with (001), (011) and (111) crystallographic surfaces. However, direct comparison between the MD simulations and experimental data is not feasible because the indentation depth in MD simulations is small (on the order of angstroms) and the indentation velocity is extremely high (nine orders of magnitude higher), preventing nanoindentation experiment to be conducted under the same conditions. To date, there is no good comparison between experimental and numerical results on all crystallographic orientations of single crystals materials, necessary to interpret nanoindentation data to extract the mechanical behavior through nanoindentation.

Several researchers have investigated mesoplastic constitutive relationships, including the pioneering work of Hill and Rice (1972), and Asaro and Needleman (1985). Peirce *et al.* (1982) analyzed the non-uniform and localized deformation in ductile single crystals in tension using mesoplasticity theory. Huang (1991) developed a material user subroutine incorporating mesoplasticity in the ABAQUS implicit program. The theoretical framework of Hill and Rice (1972) has been implemented in the 2D subroutine. Kalidindi *et al.* (1992) developed an implicit time-integration procedure based on Asaro and Needleman's constitutive model (1985).

Gambin and Barlat (1997) predicted the texture development in plastically deformed FCC metals using crystal plasticity based on the concept of yield surfaces with rounded corners. They suggested a relation between stacking fault energy (SFE) of crystalline materials and the parameters describing the roundness of yield surface vertices. Therefore, the model allows predictions of reorientation paths and texture development for FCC metals of low, medium, and high SFE.

Nakamachi *et al.* (2002) studied the influence of crystallographic texture on the formability of FCC aluminum sheet metal using elastic/crystalline viscoplastic finite element (FE) analysis. Numerical simulations of the forming processes showed evidence of texture effects on strain localization and failure. They concluded that texture of annealed sheets leads to postponement of strain localization and improvement of the formability of aluminum alloy sheet.

Yoshino *et al.* (2002) developed a two-dimensional finite element model and calculated the dislocation density distributions of single crystal copper under nanoindentation using a cylindrical indenter. Wang *et al.* (2004) simulated 3D

nanoindentation but the load-displacement curves are not in good agreement with the experimental data. Thus, a lack of good comparison between experimental and numerical results leads to the difficulty of investigating the mechanical behavior of nanoindentation on single crystal materials.

In Chapter 3, a mesoplastic constitutive model was implemented in a commercial finite element code (ABAQUS/Explicit) and investigated the material behavior of nanoindentation on single crystal copper along the [100] direction (Liu *et al.*, 2005). Experimental and numerical results are in good agreement, validating the approach. In this chapter, the deformation behavior of single crystal copper of three different orientations [(100), (011) and (111)] by nanoindentation is explored at the microscale. Large deformation theory is incorporated into the mesoplastic constitutive model to take into account large element rotation. Nanoindentation on single crystal copper along different orientations is simulated using the finite element method. Numerical results including load-displacement curves, deformation patterns around the indenter and the pile-up profiles are compared with the experimental results from indentation tests.

4.3 Numerical simulations

The mesoplastic constitutive model has been implemented using a user-defined subroutine VUMAT (ABAQUS Manual, 2003) in a commercial finite element code (ABAQUS/Explicit) in Section 3.2.3. The underlining assumption of the stress update scheme is that the element rotation is small. Under large deformations, where the element rotation is relatively large, the incrementally objective integration for stress update should be used. It is given by (Belytschko *et al.*, 2000)

$$\boldsymbol{\sigma}_{n+1} = \mathbf{Q}_{n+1} \cdot \boldsymbol{\sigma}_n \cdot \mathbf{Q}_{n+1}^T + \Delta t \overset{\nabla}{\boldsymbol{\sigma}} \quad (4-1)$$

where $\mathbf{Q}_{n+1} = \mathbf{e}^{\omega \Delta t}$ is the incremental rotation tensor associated with effective spin ω and it can be linearized as $\mathbf{Q}_{n+1} = \mathbf{I} + \omega \Delta t$ for small incremental spin. Comparing the stress update in the large deformation with the small deformation, the $\mathbf{Q} \boldsymbol{\sigma}_n \mathbf{Q}^T$ term is added to account for the proper rotation of the stress. The effective deformation rate \mathbf{D} in Eq. (3-6) can be computed from the deformation gradient \mathbf{F} and the push-forward of the incremental Green strain $\Delta \mathbf{E}$, which is defined as

$$\Delta \mathbf{E} = \frac{1}{2} (\mathbf{F}_{n+1}^T \cdot \mathbf{F}_{n+1} - \mathbf{F}_n^T \cdot \mathbf{F}_n) \quad (4-2)$$

$$\Delta t \mathbf{D} = \mathbf{F}_{n+1}^{-T} \cdot \Delta \mathbf{E} \cdot \mathbf{F}_{n+1}^{-1} = \frac{1}{2} [\mathbf{I} - (\Delta \mathbf{F}_n)^{-T} \cdot \Delta \mathbf{F}_n^{-1}] \quad (4-3)$$

$\Delta \mathbf{F}_n$ is the incremental deformation gradient given by $\Delta \mathbf{F}_n = \mathbf{I} + \nabla_n \Delta \mathbf{u}$, where $\Delta \mathbf{u}$ is the displacement increment. A strain measure should vanish for any rigid body rotation. If a strain measure fails to meet this requirement, it will predict nonzero strains, and in turn nonzero stresses, in rigid body rotation. It can be seen that the effective deformation rate \mathbf{D} is zero in a rigid rotation because $(\Delta \mathbf{F}_n)^{-T} \cdot \Delta \mathbf{F}_n^{-1} = \mathbf{I}$ in a rigid rotation. Therefore, incremental objectivity is achieved.

The effective spin is defined through

$$\boldsymbol{\Omega} \Delta t = \frac{1}{2} [(\nabla(\Delta \mathbf{u}))^T \cdot \mathbf{F}_{n+1}^{-1} - \mathbf{F}_{n+1}^{-T} \cdot (\nabla(\Delta \mathbf{u}))] \quad (4-4)$$

In this investigation, we propose and implement the large deformation formulation of mesoplasticity. To account for arbitrary crystal orientations, two coordinate systems are introduced in the calculation — specimen (global) coordinate and crystalline (local) coordinate systems. The global coordinate system is fixed and defined

on the specimen. The local coordinate system is aligned with the crystal lattice and all the material calculations are conducted in it. At each time step, transformation is performed to bring the stress formulation from one system to the other. The crystal orientation is represented in terms of the three Euler angles. The mesoplastic constitutive model is used in the finite element analysis to simulate nanoindentation on single crystal copper and obtain numerical load-displacement relationships. In the constitutive model, m is chosen as a small value such that the constitutive formulation is nearly rate independent. Thus, $\tau_0^{(k)}$, α , β are the material parameters to be determined. Appropriate parameters were determined by fitting the simulated load-displacement curves to the experimental data. If the load-displacement relations, as determined from the numerical analysis agree with the experimental data on all three orientations, the parameters in the mesoplastic model would be suitable for the single crystal copper. The material parameters used in the simulation on different orientations of single crystal copper are shown in Table 3-2.

The FEM simulations on single crystal copper were conducted to investigate the microscale behavior of the material under nanoindentation. It may be noted that ABAQUS already takes into account the large deformation theory in strain increment and stress update. The dimensions of the workpiece in FEM model are $15 \times 15 \times 10 \mu\text{m}$, which are smaller than the actual dimensions of the specimen [(100): $10 \times 10 \times 1 \text{ mm}$, (011): $10 \times 10.4 \times 2.3 \text{ mm}$, and (111): $12.5 \times 8.3 \times 2.1 \text{ mm}$] used in nanoindentation, yet much larger than the maximum indentation displacement ($\sim 310 \text{ nm}$) so that the condition of indentation into a half-space is justified. The workpiece consists of 2,688 eight-node brick elements and 3,208 nodes. Size of the mesh in the FEM is generally a compromise

between computational cost and solution accuracy. Since stress gradient reaches its highest value in the region directly underneath the indenter, very fine mesh is used near the indenter tip and coarser mesh for other regions. The mesh sensitivity analysis has been presented in Section 3.5.2. In order to ensure convergence of the simulation results with respect to the mesh size, different mesh sizes were employed. The mesh size used in this study is chosen based on the convergence and the computational efficiency.

It is well-known that the deformation and defect propagation in single crystal materials depend on the crystallographic orientation. The anisotropy of the deformation on single crystal copper is investigated by the surface topography of the indents on (100), (011), and (111) oriented surfaces using different indenters as well as by comparing the load-displacement relations. Two indenters used in this study are diamond spherical and Berkovich indenters. The spherical indenter has a radius, $R = 3.4 \mu\text{m}$. In the simulation, the indenter is modeled as a rigid body. This is justified as the diamond indenter has a modulus of 1000 GPa, which is more than an order of magnitude higher than that of Cu, which has a modulus on the order of 120 GPa. In simulations, the indenter moves towards the workpiece at a constant velocity. A frictionless contact pair, implemented by two contact surfaces with associated nodes between the indenter and the workpiece is defined. The effect of friction coefficient on the nanoindentation behavior of a single crystal copper have been investigated in Section 3.5.4 and it was found that the introduction of friction does not change the nanoindentation load-displacement relation but changes the indent surface profile. The top surface of the workpiece is traction free and nodes on the bottom are constrained along the indentation direction. To compromise the stability of the dynamic simulation and the overall computational time, the time step

increment is fixed at 60 ps ($1 \text{ ps} = 10^{-12} \text{ s}$) in the simulations. This leads to a total time step increments of 67,000 in the simulation, including loading, intermediate transition, and unloading. The intermediate transition step entails ramping down the velocity to remove the numerical discontinuities in the resistant force caused by the abrupt change in the velocity direction of the indenter.

4.4 Experimental setup and test conditions

To obtain experimental results for comparison with numerical simulation results, nanoindentation tests were conducted on the (100), (011) and (111) oriented single-crystal copper surfaces. An MTS NanoIndenter (XP) system was used on single crystal copper samples to obtain nanoindentation load-displacement relationships. The system can reach a maximum indentation displacement of 500 μm and a maximum load of 500 mN. The displacement resolution is 0.2 nm and the load resolution is 50 nN. All nanoindentation tests were conducted in air at room temperature (23°C). The tests did not start until a thermal equilibrium state had been reached and the drift of the indenter tip dropped below a set value, typically 0.05 nm/s. After the indenter tip had made contact with the specimen surface, the indenter penetrated gradually to the surface of the specimen, and the indentation load and displacement were recorded simultaneously at a sampling rate of five data points per second.

Three single crystal copper samples with (100), (011) and (111) oriented surface planes were prepared for nanoindentation tests with dimensions of $10 \times 10 \times 1 \text{ mm}$, $10 \times 10.4 \times 2.3 \text{ mm}$ and $12.5 \times 8.3 \times 2.1 \text{ mm}$, respectively. All samples were cut from an ingot using electrical discharge machining (EDM) and the surface was chemo-mechanically polished. The surface roughness was measured by AFM, and the R_a value is 9.08 nm for

(100) surface. Each sample was mounted separately on a flat end aluminum cylinder before the test. Indentations were made using two different indenters on the specimens. One was a Berkovich diamond indenter; the other was a spherical diamond indenter with a radius of 3.4 μm . In selected tests, a nanoindenter with a tip radius of 10 μm was also used to determine the hardness, and a microindenter with a tip radius of 500 μm was used on a Clark Micro Hardness Tester (Model CM-700AT) to determine the microhardness and its dependence on the indenter tip radius. For each indentation displacement, nanoindentation tests were conducted at four different locations to ensure repeatability of data. It was ensured that all the indents were away from the edge of the sample and the distance between any two neighboring indents was at least 10 times the impression diameter to avoid interference in nanoindentations at different locations. After the nanoindentation tests, the copper samples were immediately scanned under an AFM to obtain the surface topographies and the pile-up profiles. The experimental data are then compared with the numerical results.

4.5 Results and discussion

Finite element simulations of nanoindentation were conducted at various indentation depths on single crystal copper specimen in three crystallographic orientations [(100), (011), and (111)] with indenters of two different geometries, namely, a spherical indenter (3.4 μm radius), and a Berkovich indenter. In nanoindentation, at the microscale, plastic deformation occurs primarily by slip on certain preferred slip systems, causing either pile-up or sink-in in the vicinity of the indent. In this section, the nanoindentation simulation results on single crystal copper on different crystallographic planes will be presented.

4.5.1 Nanoindentation using a Spherical Indenter

Using a commercial software (ABAQUS) with a user-defined material subroutine, the simulation setup of nanoindentation on (100) single crystal copper were fully described in Section 3.4. Through multiple trial runs, using the parameters given in Table 3-2, a reasonably good agreement between the numerical and experimental load-displacement curves has been achieved for indentations on surfaces with various crystallographic orientations using a spherical indenter (radius $3.4\text{ }\mu\text{m}$), as shown in Fig. 4-1. The load increases monotonically as the indentation proceeds, and the load follows the displacement when the indenter retracts from the surface of the copper. Fig. 4-1 (a) and (b) show a comparison of experimental and simulation results in reasonably good agreement. In Fig. 4-1 (c), there are two simulation curves, simulation_1 and simulation_2, corresponding to the results obtained using the 8-node brick element and 10-node tetrahedron element, respectively. The purpose of using two types of elements is to investigate the dependency of the load-displacement curve on the element type. It can be seen that the two simulation curves reach the same load at the maximum displacement although the curve with the 10-node tetrahedron element is smoother than its counterpart. In order to maintain comparability of the simulation results among three orientations, the same mesh with 8-node brick element is used for all the simulations hereafter.

In Fig. 4-1 (a)-(c), the nanoindentation experimental data using a spherical indenter with $3.4\text{ }\mu\text{m}$ radius shows that at the same displacement, the reaction force on the (111) surface is the lowest while that on the (100) surface is the highest. For example, at 250 nm displacement, the test force on the (111) surface is 3.00 mN , in comparison to 3.55 mN on the (011) surface and 3.82 mN on the (100) surface. This phenomenon will

be further investigated by employing spherical indenters of other sizes to investigate the size effect. It can be seen from Fig. 4-1 (a) to (c) that the slope of the three unloading curves is very close to each other because the unloading behavior is solely determined by the elastic properties of the material. The steep unloading curves indicate that the amount of elastic recovery is small under unloading for single crystal copper.

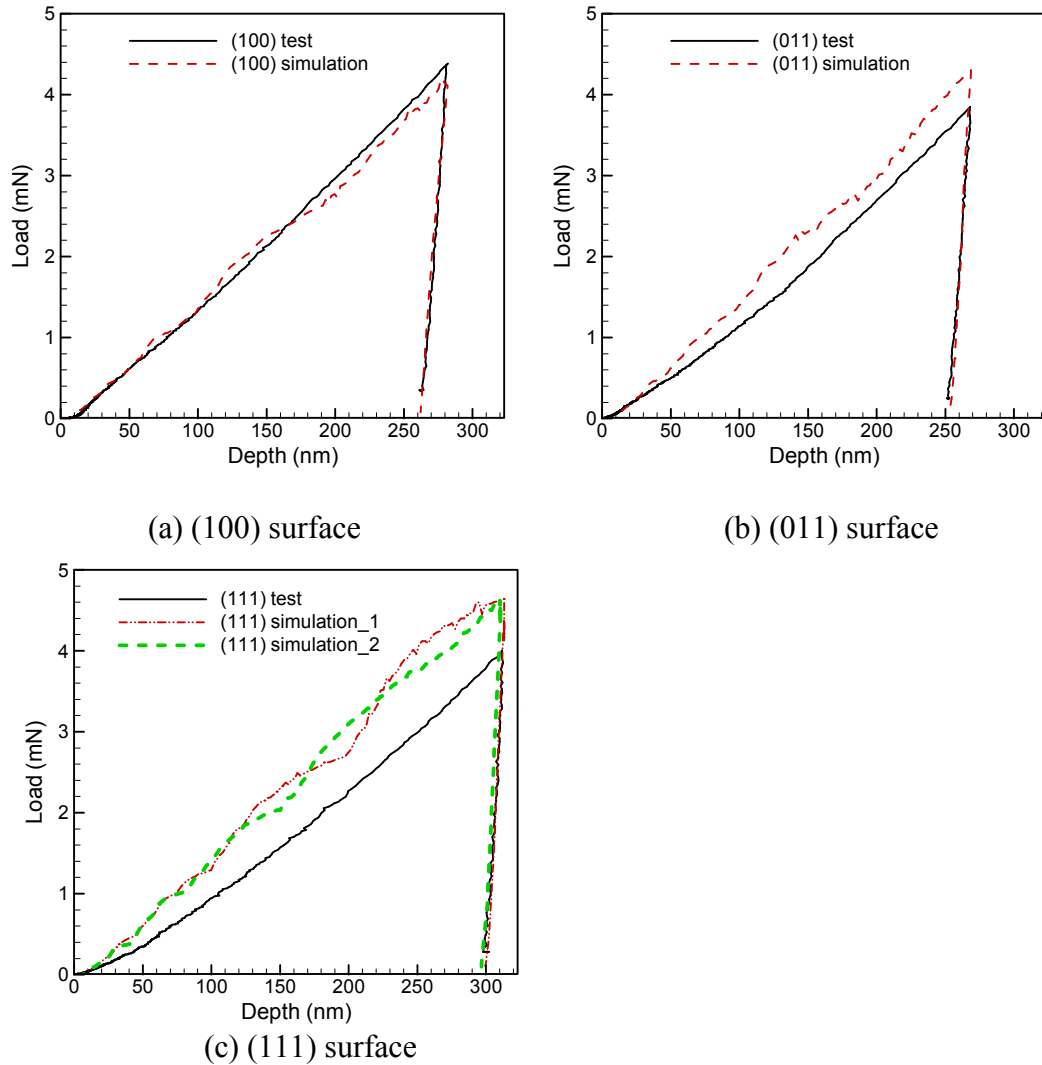


Fig. 4-1: Comparisons between numerical and experimental load-displacement curves on copper samples of different crystallographic orientations made with a spherical indenter (tip radius $3.4 \mu\text{m}$)

To the best of knowledge of the author, no satisfactory agreement between numerical and experimental load-displacement curves on single crystal copper on all the three orientations have been reported previously. Fivel *et al.* (1998) compared the experimental results with the simulation load-displacement curve at a displacement of 50 nm on a [001] oriented single crystal copper using a combination of 3D discrete dislocation simulation and FEM. The unloading part of the load-displacement curve was not included and the orientation effects were not studied. Wang *et al.* (2004) presented a study of the dependence of nanoindentation pile-up patterns and microtextures on the crystallographic orientation using copper single crystals. The comparison of the load-displacement curves between experiments and simulations indicated deviation that was about an order of magnitude although the correspondence on pile-up patterns was satisfactory. Liang *et al.* (2004) used MD simulations to study crystal plasticity during nanoindentation by comparing the elastic-plastic response of three copper substrates with (001), (011) and (111) crystallographic planes. However, comparison of the load-displacement relationships between MD simulations and experimental data were not available.

Fig. 4-2 shows distributions of out-of-plane displacements at three crystallographic orientations, (100), (011), and (111). There are both positive and negative values in the displacement [see Fig. 4-2 (a)-(c)]. The positive values occur symmetrically around the indent impression in all three figures and they represent the pile-up patterns of the material. The pile-up regions correspond to high dislocation densities. Copper is an FCC metal with the predominant slip planes and slip directions being {111} and $\langle 110 \rangle$, respectively. As the crystal is indented in the (100) surface,

plastic deformation takes place along the $\{111\}$ planes and in the $\langle 110 \rangle$ directions. In Fig. 4-2 (a), the surface is elevated in the four $\langle 110 \rangle$ directions (pile-up) as expected when viewed along the direction of application of the load. Therefore, slip extends away from the indents along the $\langle 110 \rangle$ directions, leading to slip and material flow along these directions. This is so because the $\{111\}$ family of slip planes intersect with the (100) surface at the $\langle 110 \rangle$ directions. For example, the (111) slip plane intersects with the (100) surface along the $[01\bar{1}]$ direction. Thus, a 4-fold symmetry is expected, as can be seen in Fig. 4-2 (a). Even though the indenter is spherical, metal pile-up does not occur all round the indent but occurs at four corners forming a four-fold, square symmetry.

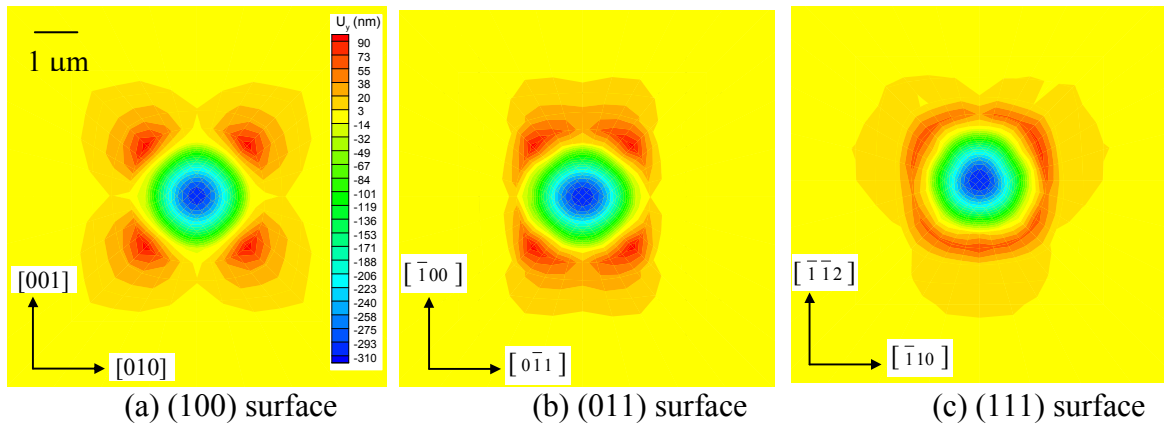
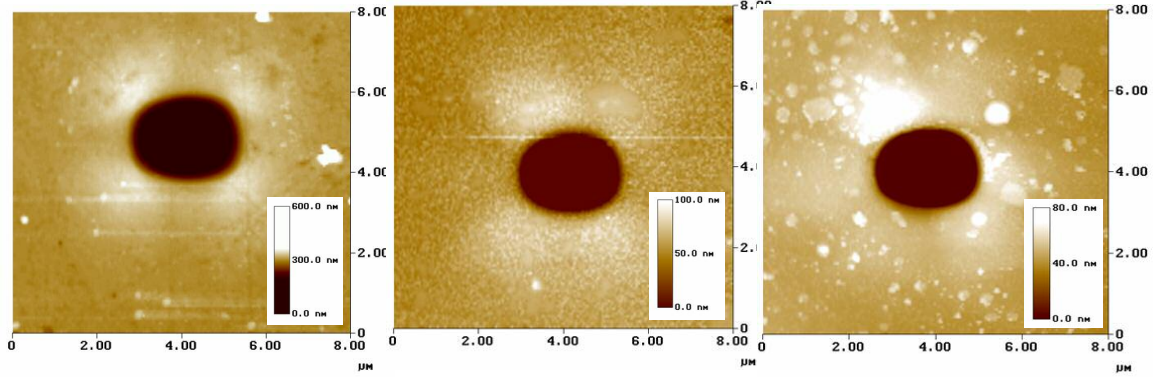


Fig. 4-2: Distributions of out-of-plane displacements at different orientations on a copper sample using a spherical indenter (tip radius $3.4 \mu\text{m}$).

In the (011) plane, one can see only two-fold, rectangular symmetry [Fig. 4-2 (b)]. The predominant slip planes and the (011) surface have intersection vectors as $\langle 211 \rangle$. The angle between the directions $[\bar{1}00]$ and $[21\bar{1}]$ is $35^\circ 16'$, which is approximately the case in Fig. 4-2 (b). In contrast, in the (111) plane, a three-fold symmetry can be seen with the build-up occupying a third of the indent circumference [Fig. 4-2 (c)]. The intersection vectors are $\langle 110 \rangle$. The $[\bar{1}\bar{1}2]$ direction meets the $\langle 110 \rangle$ vectors at an angle of

30°, as observed in Fig. 4-2 (c). In summary, for all the surfaces studied, the symmetry of the pile-up distributions correlates with the orientation of slip systems $\{111\}\langle 110\rangle$. These observations are consistent with the experimental results shown in Fig. 4-3 (a)-(c).



(a) (100) surface (b) (011) surface (c) (111) surface
Fig. 4-3: AFM images of the indent impressions made on copper workpiece with a spherical indenter (tip radius 3.4 μm) at different crystallographic orientations

Fig. 4-3 (a)-(c) show AFM images of the indents with a spherical indenter (3.4 μm radius) on various crystallographic surfaces. After the nanoindentation tests, the copper samples were imaged using an AFM to acquire the surface topography. On the images, the bright color corresponds to the pile-ups. It can be shown from Fig. 4-3 that pile-up patterns from experiments agree well with the simulation results, i.e., the patterns on the (100) surface presents four-fold symmetry, (011) surface two-fold, and (111) surface a three-fold symmetry. Moreover, the exhibited symmetry characteristics of the surfaces coincide with the experimental observations reported in the literature for single crystal copper (Lee *et al.*, 2000; Flom and Komanduri, 2002; Peralta *et al.*, 2004; Wang *et al.*, 2004). The size of the plastic deformation zone around the indents is observed to be from 1 to 7 μm on the horizontal axis for the (100) surface indent [Fig. 4-3 (a)], from 2 to 6 μm for (011) surface indent [Fig. 4-3 (b)], and from 0 to 7 μm for the (111) surface

indent [Fig. 4-3 (c)]. The experimental data suggests that the deformation zone is the largest on the (111) surface. The size of the plastic zone is an important parameter in determining the yield stresses of single crystal and polycrystalline material (Bahr *et al.*, 1998). It can be seen from the experimental and simulation results [Fig. 4-2 (a)-(c) and Fig. 4-3 (a)-(c)] that the symmetry characteristics and the size of the plastic zone depend strongly on the crystal orientation.

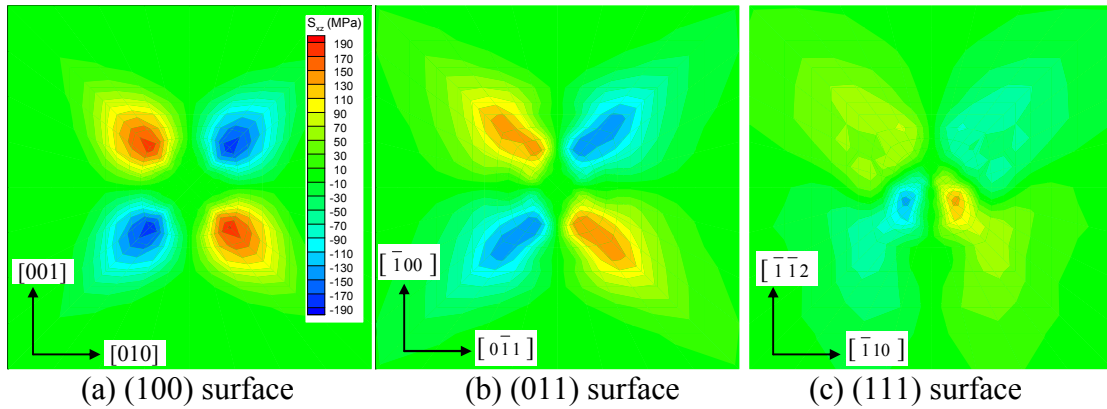


Fig. 4-4: Shear stress σ_{xz} distributions on the indented planes of different orientations in the indentation of copper

We turn next to the study of the shear stress σ_{xz} distribution with the y -axis as the indentation direction in the global coordinate system. Even though the spherical indenter is symmetric, the distribution and magnitude of the shear stresses is not the same [Fig. 4-4 (a)-(c)]. The shear stresses on two opposite sides of the indent have the same sign while the shear stresses in the direction orthogonal to them have the opposite sign. The distribution of shear stresses on both (100) and (011) appears to be similar although (100) has a larger magnitude. The shear stress reaches a maximum on (100), followed by shear stress on (011), and on (111) with the spherical indenter (3.4 μm radius). However, for the (111) orientation, the distribution of shear stresses is asymmetric indicating a strong crystal anisotropy [Fig. 4-4 (c)].

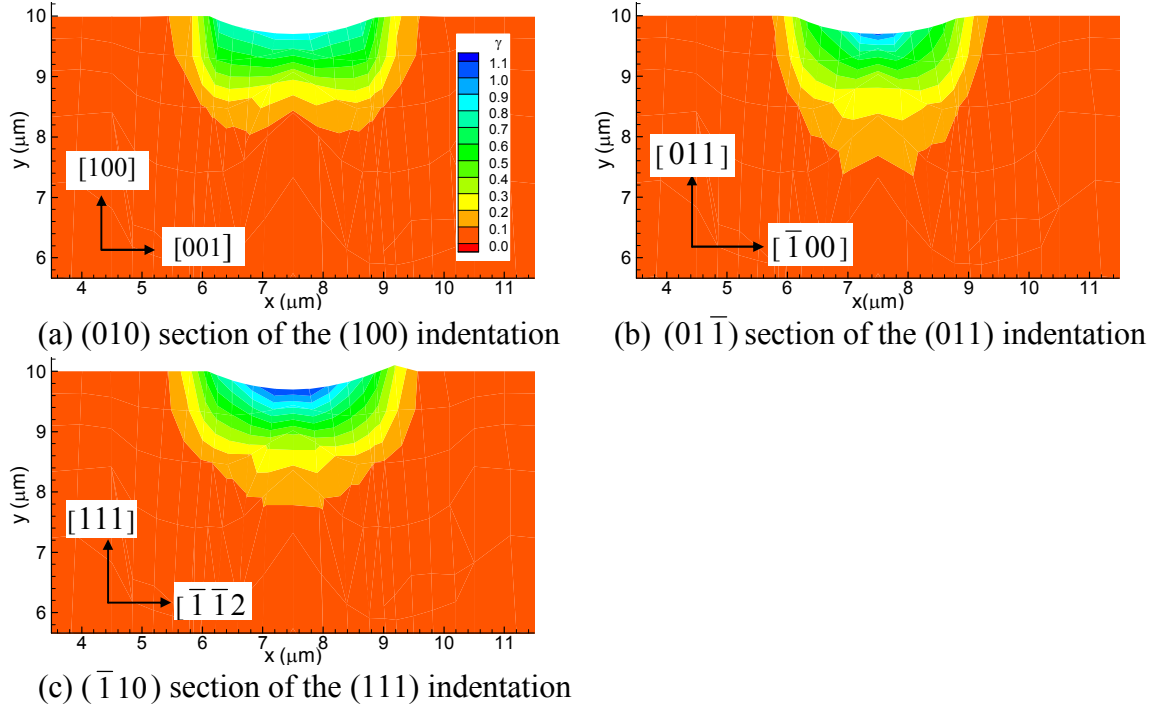


Fig. 4-5: Distributions of shear strain (total shear strain on all the slip systems) on the mid-section of the copper workpiece

Fig. 4-5 shows the distributions of the total shear stain in the adjacent region of the indenter tip, as observed from a section cut through the middle of the workpiece with the orientations marked. The total shear strain is defined as the summation of the absolute value of the individual shear strain over the 12 slip systems. As for the magnitude of total shear strain, it is the largest for the (111) indentation case, namely, 1.1 and smallest for the (100) indentation case, namely, 0.86. This is attributed to the easiest slip on the (111) plane, i.e., most packed plane for single crystal copper.

As presented in Section 3.5.4, friction plays a significant role in affecting the magnitude of pile-ups in the nanoindentation modeling. In nanoindentation, the frictional condition on the contact pair, namely, the indenter tip and workpiece surface is so complex that the exact friction mechanism is unknown. In this investigation, Coulomb frictional contact was introduced in the FEM simulation on nanoindentation and it was

determined a coefficient of friction (COF) of 0.4 is appropriate for nanoindentation simulation based on the comparison between experimental and simulation results. Using a COF of 0.4, the pile-up profiles on the three indented surfaces are shown in Fig. 4-6. The lines on the images on the lower right corner of Fig. 4-6 (a)-(c) show the scan direction of which the pile-up profile was obtained. It can be seen that the scans approximately cut through the maximum pile-up locations. It may be noted that all the profiles show the pile-up behavior, instead of sink-in due to the work-hardened condition of the samples. As shown in Fig. 4-6 (a) and (b), the simulation profiles agree with the experimental profiles on the indented well of the profiles although the simulation profiles show a slightly larger pile-up magnitude than the experiment.

The previous discussion was for indentation results with a spherical indenter of radius 3.4 μm . To determine the mechanical behavior of single crystal copper with three orientations under spherical indentations with different indenter tip radii, two other spherical indenters with tip radii of 10 μm and 500 μm were also used. Nanoindentations were conducted using the MTS NanoIndenter (XP) system with the diamond spherical indenter of 10 μm and microindentations were conducted on a Clark Micro Hardness Tester (Model CM-700AT) using the spherical cemented tungsten carbide indenter with a radius of 500 μm .

Fig. 4-7 (a)-(c) show the variation of mean pressure (i.e., hardness), P_m versus the ratio of the indent radius to the indenter radius, (a/R) for different indenter radii, R . In Fig. 4-7 (a), P_m is different for the three orientations investigated; it is largest on (100) plane and smallest on (111) plane. However, this tendency is not seen in Fig. 4-7 (b) and

(c). In Fig. 4-7 (b) and (c), P_m of (011) and (111) plane is very similar, while of (100) plane varies.

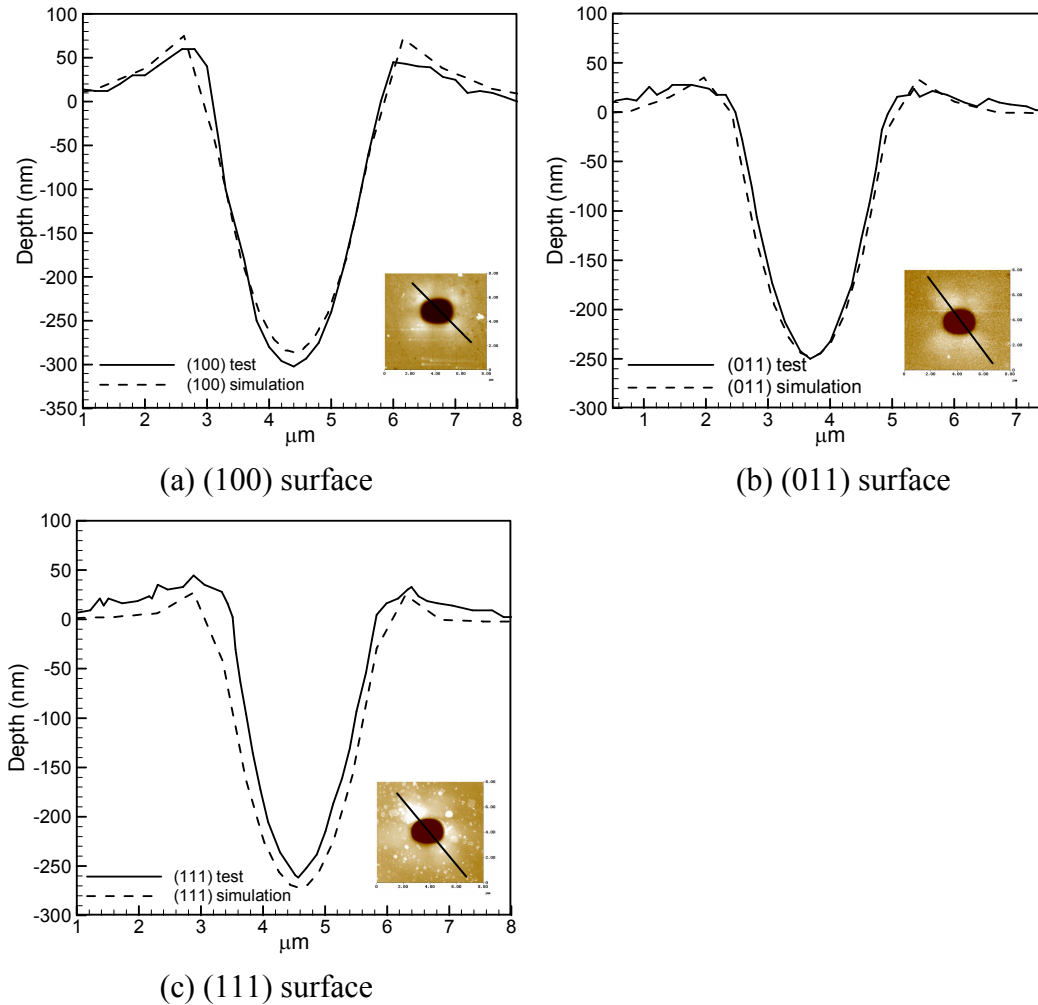


Fig. 4-6: Comparisons of the pile-up profiles of indents made on copper samples with a spherical indenter (tip radius $3.4 \mu\text{m}$)

Lim and Chaudhri (2002) studied the microindentation hardness on single grains of a polycrystal of copper [(110) and (111) orientations] using a cemented tungsten carbide spherical indenter of radius $200 \mu\text{m}$. They found the indentation hardness values of single crystal copper of different orientations to be very similar. They attributed that prior dislocation density of the specimens to be the most likely parameter to causes this. Tsuru and Shibutani (2007) conducted atomistic simulations of nanoindentation (using

spherical indenters of radius 5 nm, 15 nm and 30 nm) of Al and Cu [(001), (110), and (111) planes] to investigate anisotropic effects in elastic and incipient plastic behavior under nanoindentation. They found that (001) and (111) planes exhibit inherent critical mean pressure for dislocation nucleation, while (110) shows values that vary according to the indenter radius caused by variations in the location of the dislocation emission. The experimental results in Fig. 4-7 show that variation of P_m on the three orientations depends strongly on the indenter radius used.

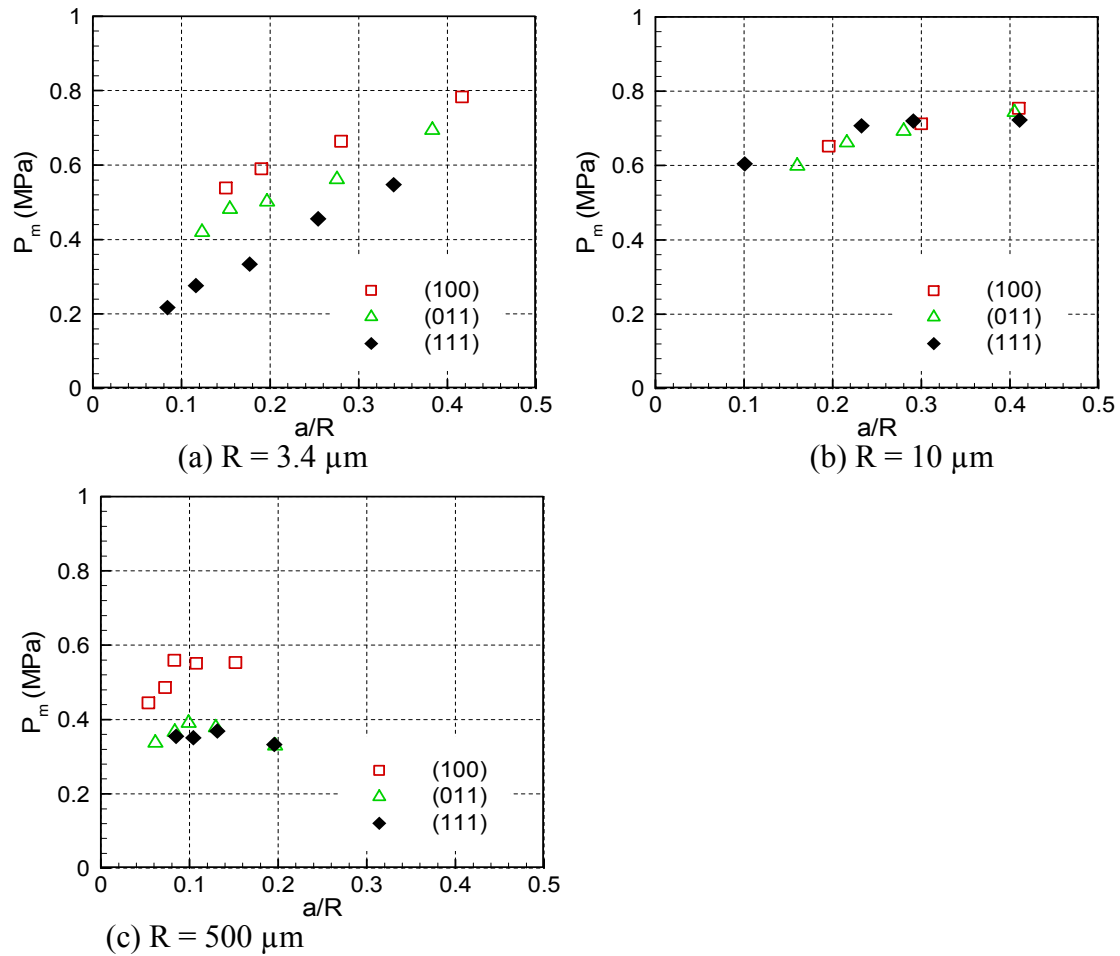


Fig. 4-7: Experimental results on the variation of mean pressure, P_m with a/R on copper samples of different orientations for three spherical indenters of different radii

From all comparisons between the numerical results and experimental measurements for nanoindentations on the three surfaces of single crystal copper using a spherical indenter, it is conclusive that the material parameters and the nanoindentation model are appropriate in predicting the mechanical behavior of single-crystal copper under various crystalline orientations. Therefore, the numerical model can be used to estimate the crystal orientation for a given single crystal copper sample or the orientation of a particular grain of a polycrystalline copper sample. Through nanoindentation experiments and AFM imaging, the load-displacement curve and the pile-up patterns of a sample can be obtained. In the simulation, the three Euler angles, which represent the crystal orientation, can be adjusted such that both load-displacement curve and the pile-up patterns match the corresponding experimental results. Thus, the orientation of the crystal can be obtained provide the Euler angles are determined.

4.5.2 Nanoindentation using a Berkovich Indenter

The measurement of mechanical properties by nanoindentation methods is most often conducted using indenters with a triangular pyramid or with a sphere because they provide a wealth of information (Pharr *et al.*, 1996). In order to explore the behavior of single crystal copper under geometrically different indenters, the pyramidal, three-sided Berkovich indenter is also used in the simulations. The main geometrical distinction between a spherical indenter and a Berkovich indenter is that the former is axisymmetric while the later is three-fold symmetric. In the FE model, the Berkovich indenter was constructed exactly following the specifications of the indenter given by the manufacturer. The angles between the normal and the three faces of the indenter are

65.2°. In the simulations, all the numerical parameters are the same as in the spherical indenter simulations except the indenter was changed to Berkovich shape. As for the in-plane orientation of the indenter, it makes no difference for the spherical indenter since it is axisymmetric. For the Berkovich indenter, it appears that the mechanical behavior of single crystal materials depend on the in-plane crystallographic orientations of the material rather than the in-plane orientation of the three fold symmetric Berkovich

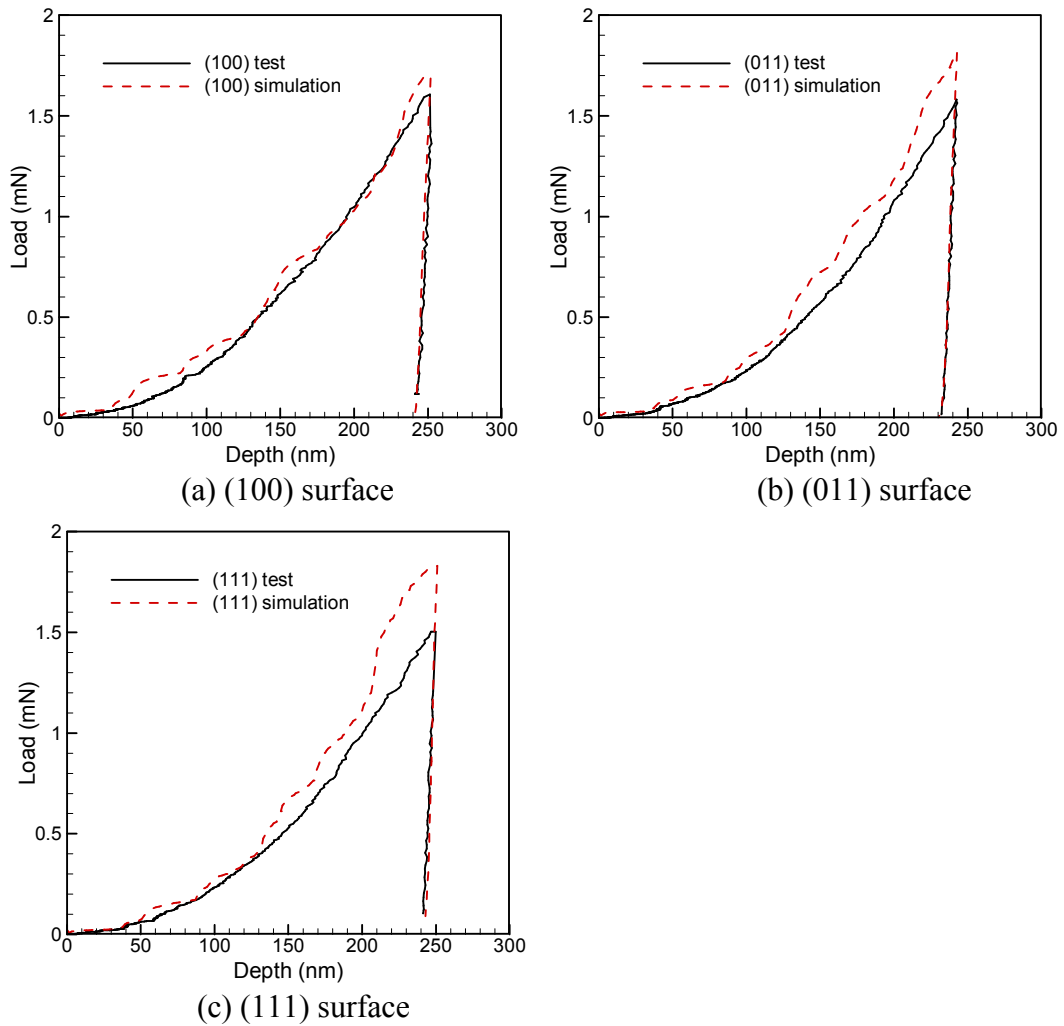


Fig. 4-8: Comparisons between numerical and experimental load-displacement curves for different orientations of copper with a Berkovich diamond indenter

indenter (Vlassak and Nix, 1994; Grillo *et al.*, 2003; Peralta *et al.*, 2004). In all simulations, the orientation of the Berkovich indenter is kept the same in the global coordinate system as can be seen in Fig. 4-10 [(a)-(c)].

Fig. 4-8 (a)-(c) show the load-displacement comparisons between experiments and simulations for different orientation. The comparisons are, in general, reasonably good as shown in Fig. 4-8 (a) and (b), while the comparison on (111) surface indentation is not as good as the other two, especially after the displacement is larger than 200 nm. Although efforts have been focused on calibrating the material parameters, the satisfactory comparisons between the experimental and numerical load-displacement curves on all the three surfaces were not obtained in the meanwhile.

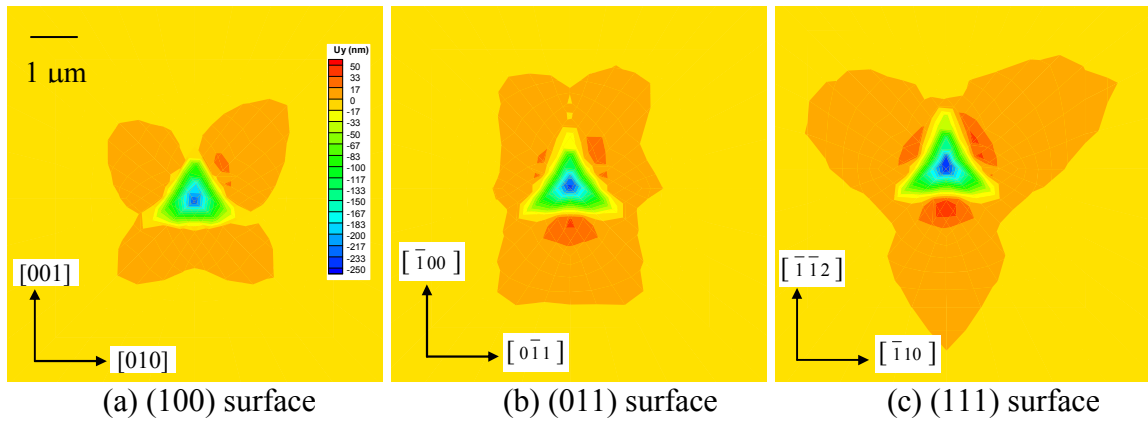


Fig. 4-9: Distributions of out-of-plane displacements at different orientations on copper using a Berkovich diamond indenter

Fig. 4-9 shows the out-of-plane displacement distributions from nanoindentation using a Berkovich indenter. In comparison to the four-fold and two-fold symmetries [Fig. 4-2 (a) and (b)], Fig. 4-9 (a) and (b) do not appear to have the same symmetry characteristics with the same surface in nanoindentation under spherical indenter. In both Fig. 4-9 (a) and (b), it is observed that the pile-up extends away from the two upper sides of the triangular indent impression. Pile-up is also present below the horizontal side of

the triangle. The topography on the (111) surface reveals the three-fold symmetries, as in Fig. 4-2 (c), because the Berkovich indenter has the same symmetric characteristic. Fig. 4-10 (a) to (c) shows the AFM images of the indent impressions made with the Berkovich indenter.

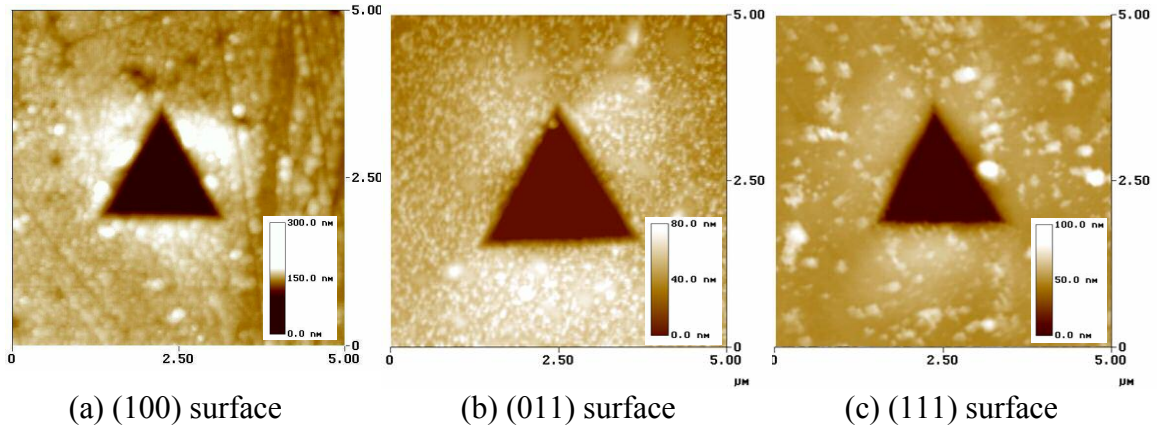


Fig. 4-10: AFM images of the indent impressions made on copper at different crystallographic orientations with a Berkovich diamond indenter

Fig. 4-11 (a) to (c) shows the indentation profiles scanned through the same direction in the global coordinate system on all three indented surfaces. The scan direction is shown by the line on the lower right image in Fig. 4-11 (b). This scanning line passes the top vertex of the triangle, perpendicular to the base of the triangle. It can be seen that comparisons on the pile-up profiles between the nanoindentation testing and the simulation results on all three crystallographic orientations are in reasonably good agreement. However, the simulations tend to under predict the amount of pile-ups, resulting in smaller pile-up values than the measurement data.

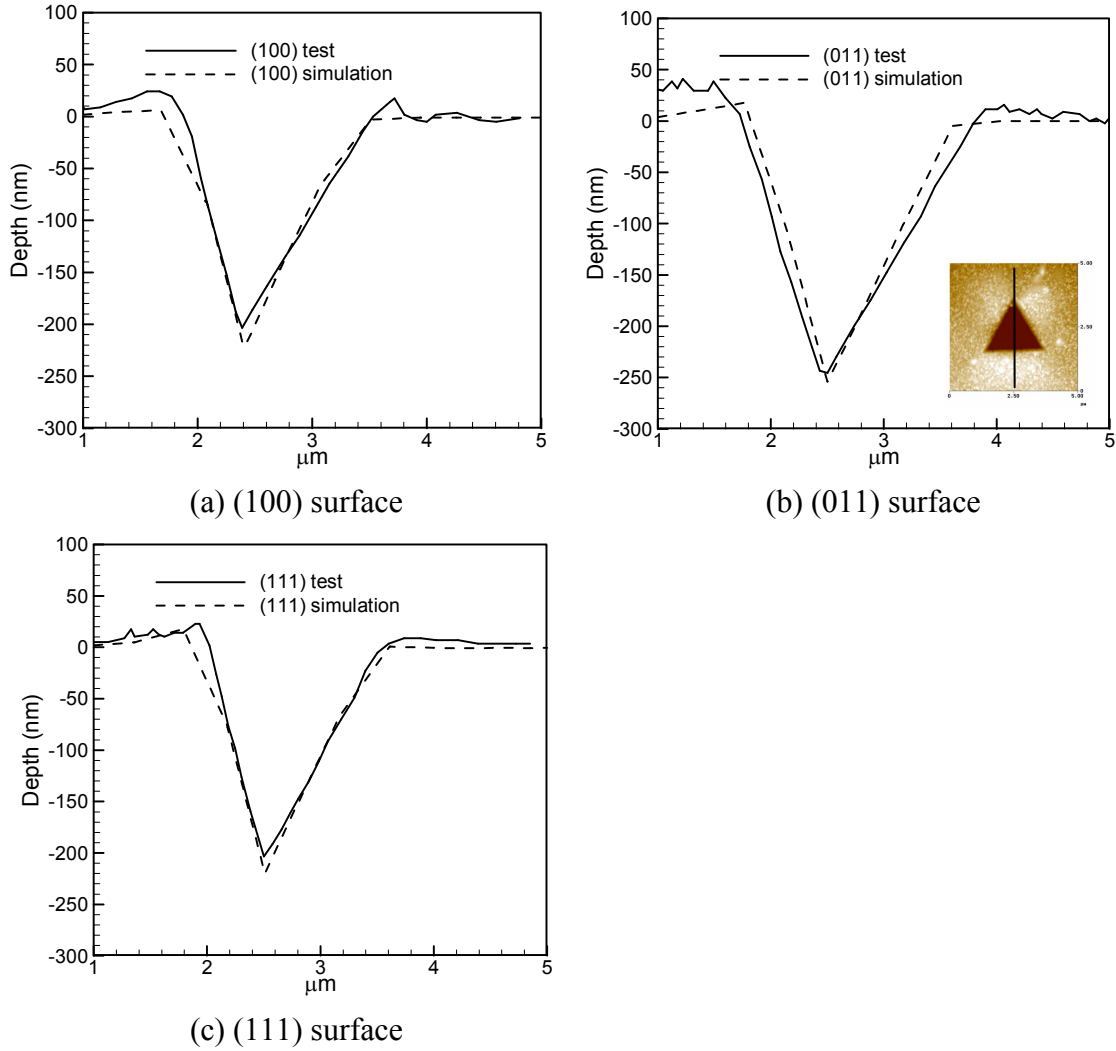


Fig. 4-11: Comparisons of the pile-up profiles of indents made on copper at different crystallographic orientations with a Berkovich diamond indenter

4.6 Conclusions

Nanoindentations using both spherical and Berkovich indenters on single crystal copper of three crystallographic orientations, i.e. (100), (011) and (111) were simulated using a commercial software (ABAQUS) incorporating mesoplasticity constitutive law in the user subroutine VUMAT. Large deformation theory is incorporated into the model so that large element rotation can be considered appropriately. Nanoindentation measurements were made to determine the load-displacement relations and the AFM was

used to obtain the surface topographies and pile-up profiles for comparison purpose. On a spherical nanoindentation, distribution of the out-of-plane displacements at three crystallographic orientations, (100), (011), and (111) show pile-ups with a topographical pattern of four-fold, two-fold and three-fold symmetry, respectively in both experiments and simulations. No sink-in was observed due to the work-hardened condition of the specimens. The magnitude of the pile-ups, the in-plane shear stresses and the total shear strains were compared on the three surfaces and correlated with the orientation effects.

Under nanoindentation with a spherical indenter, the material behavior of single crystal copper strongly depends on the crystal orientation. Using a Berkovich indenter, the deformation patterns on the (111) surfaces showed a three-fold symmetry which is in good agreement with the finite element results. Further, the comparison between the nanoindentation and simulation on load-displacement relations and pile-up profiles were also in reasonably good agreement, lending further demonstration on the capability of the current model. To the best of the knowledge of the author, no satisfactory agreements between numerical and experimental load-displacement curves on single crystal copper on all the three orientations have been reported previously. Thus, material properties of single crystal copper can be determined based on their deformation behavior under indentation. It is concluded that the numerical model can be used to estimate the crystal orientation for a given single crystal copper sample or the orientation of a particular grain of a polycrystalline copper sample.

Chapter 5

Discrete Dislocation Method at the Mesoscale

5.1 Introduction

There exist various techniques to model material behavior at the mesoscale. This chapter presents one such method, namely, discrete dislocation method. Mesoplasticity was used to model nanoindentation problems in Chapters 3 and 4. Mesoplasticity models material constitutive behavior based on slip systems of crystal lattice. Slip in crystalline metals is a consequence of the motion of large number of dislocations. In order to model the motion of relatively small number of dislocations, various discrete dislocation models have been presented in the past two decades. In general, dislocations are described as line singularities in an elastic medium (Amodeo and Ghoniem, 1990; Gulluoglu and Hartley, 1993; Kubin and Canova, 1992; Fang and Dahl, 1993; Groma and Pawley, 1993; van der Giessen and Needleman, 1995; Zbib *et al.*, 1998; Shilkrot *et al.*, 2004). When it comes to the interactions of the dislocations, the long-range forces are well-represented by the linear elastic fields outside a dislocation core radius of about five Burgers vectors from a dislocation. Within a distance of several Burgers vectors from the core, the displacement field around the dislocation is nonlinear and can not be accurately described by linear elasticity (Amodeo and Ghoniem, 1990). The short-range interactions of dislocations include the nucleation, immobilization and annihilation. The effects involved are represented by a set of constitutive rules.

At the present state-of-art, the discrete dislocation method can be divided into two categories: dislocation dynamics (Amodeo and Ghoniem, 1990; Gulluoglu and Hartley, 1993) and static (quasi-static) equilibrium method (van der Giessen and Needleman, 1995; Shilkrot *et al.*, 2004). In dislocation dynamics, the Peach-Koehler force drives the evolution of dislocations with time. In static equilibrium methods, dislocations are located by minimizing the total energy or, equivalently, finding the zero-force positions where the force on a dislocation is the derivative of the total energy with respect to the position of the dislocation (Cutin and Miller, 2003). Static equilibrium method does not take temperature into account. Therefore dislocation climb, which occurs at high temperature, is not considered.

In the context of multiscale simulation, mesoscale dislocation modeling is used in bridging the continuum and atomistic simulations (Raffi-Tabar *et al.*, 1998). A multiscale framework merging two scales, the mesoscale/microscale and the continuum scale, was developed to create a hybrid elasto-viscoplastic simulation model coupling discrete dislocation dynamics with finite element analysis based on the principle of superposition (Zbib and Diaz de la Rubia, 2002). The involvement of dislocation dynamics in connecting the atomistic and continuum scales enables the model to handle plastic deformation through the explicit motion of dislocation defects in the continuum region. With this feature, the multiscale model is completely structured for applications, such as nanoindentation (Shiari *et al.*, 2005). Recently, nonlinear deformation has been considered in coupling to represent the physical phenomenon. The coupled atomistic/continuum discrete dislocation (CADD) method has demonstrated its capability in detecting dislocations in the atomistic region and converting the atomistic dislocations

into discrete dislocations in the continuum region (Shilkrot *et al.*, 2004). A dynamic version of the CADD method has been used to study the nanoindentation process as a function of temperature and velocity of indentation (Shiari *et al.*, 2005).

While FEM has been developed as an appealing simulation technique at the continuum scale, it is subjected to some deficiencies, including the complexity in mesh generation for computational bodies with complex geometries and severe mesh distortion under large nonlinear deformations. To overcome some of the limitations of FEM, the material point method (MPM) (Sulsky *et al.*, 1995; Sulsky and Schreyer, 1996) was introduced for dynamic simulations and the generalized interpolation material point (GIMP) method (Bardenhagen and Kober, 2004) was presented with improved simulation stability. MPM is a particle method for simulations in computational fluid and solid mechanics. The method uses a regular structured grid as a computational scratchpad for computing spatial gradients of field variables. The grid is convected with the particles during deformations that occur over a time step, eliminating the diffusion problems associated with advection on an Eulerian grid. MPM has also been successful in solving problems involving contact, having an advantage over traditional finite element (FE) methods in that the use of the regular grid eliminates the need for doing costly searches for contact surfaces. In MPM and GIMP, material points that can conform to the geometric complexity with ease are used to discretize the computational body. A multiscale simulation bridging the continuum scale using the GIMP method and the atomistic scale using MD was proposed and verified in 2D using the multilevel refinement technique in a parallel computing environment (Ma *et al.*, 2005; Ma *et al.*, 2006). Coupling between GIMP and MD is achieved using compatible deformation,

force, and energy fields in the transition region between GIMP and MD. This coupling framework can overcome some inherent limitations of FEM while maintaining the advantages of the multiscale modeling.

In this chapter, a multiscale simulation scheme, encompassing GIMP at the continuum scale and dislocation dynamics (DD) at the mesoscale is presented. The technique has expanded the previous GIMP and MD coupling method (Ma *et al.*, 2006) by introducing discrete dislocations in the framework of coupling. Dislocation accommodation and propagation mechanisms are introduced by detecting dislocations from the MD simulation in real time and then passing them through the handshaking region of the continuum and atomistic zones. Discrete dislocations are the common description of plastic deformation for the continuum region and the atomistic region. Therefore, this method allows plastic deformation to occur at the handshaking region. Furthermore, the new method can handle larger numerical model without drastically increasing the computational costs, as the introduction of DD allows the regions modeled by MD to be smaller. DD can also substitute MD in the simulations of some of the critical areas without significant loss of accuracy and the computation is more economical for the same model.

5.2 Coupling between the GIMP and DD

5.2.1 Numerical formulation

The current state of a deformable body in terms of the displacement, strain, and stress fields is computed as the superposition of two fields (van der Giessen and Needleman, 1995),

$$\mathbf{u} = \tilde{\mathbf{u}} + \hat{\mathbf{u}} \quad , \quad \boldsymbol{\varepsilon} = \tilde{\boldsymbol{\varepsilon}} + \hat{\boldsymbol{\varepsilon}} \quad , \quad \boldsymbol{\sigma} = \tilde{\boldsymbol{\sigma}} + \hat{\boldsymbol{\sigma}} \quad (5-1)$$

where the (\sim) fields are the fields associated with N dislocations in their current configuration but in an infinite homogeneous medium. The complimentary (\wedge) fields are used to enforce the correct boundary conditions. The solution for $\tilde{\boldsymbol{\sigma}}$, $\tilde{\boldsymbol{\varepsilon}}$, and $\tilde{\mathbf{u}}$ is the superposition of the fields of individual dislocations. Therefore, the computational region is discretized into Problems I and II as follows (van der Giessen and Needleman, 1995):

Problem I: Discrete dislocations residing in an infinite homogeneous elastic material.

The solution for the total stress $\tilde{\boldsymbol{\sigma}}$, strain $\tilde{\boldsymbol{\varepsilon}}$ and displacement $\tilde{\mathbf{u}}$ is obtained by superposition on all the dislocations at position \mathbf{d}^i in an infinitely large elastic continuum:

$$\tilde{\boldsymbol{\sigma}} = \sum_i^N \tilde{\boldsymbol{\sigma}}^i \quad , \quad \tilde{\boldsymbol{\varepsilon}} = \sum_i^N \tilde{\boldsymbol{\varepsilon}}^i \quad , \quad \tilde{\mathbf{u}} = \sum_i^N \tilde{\mathbf{u}}^i \quad (5-2)$$

Each dislocation i is characterized by its Burgers vector \mathbf{b}^i and the unit normal vector \mathbf{m}^i of its slip plane. For plane-strain problems involving edge dislocations, each pair of dislocations in a limiting sense represent a cross-section of a dislocation loop (van der Giessen and Needleman, 1995). If the material is elastically isotropic with shear modulus μ and Poisson's ratio ν , the components $u_\alpha^i (\alpha = 1, 2)$ of the infinite-body displacement field $u^i(x_\alpha)$ due to dislocation i positioned at (X_1^i, X_2^i) are given by the following equations for dislocations with positive Burgers vector (Hirth and Lothe, 1982). For dislocations with negative Burgers vector, the sign for the equations are reversed.

$$u_1^i(x_\alpha) = \frac{\|\mathbf{b}^i\|}{2\pi(1-\nu)} \left\{ \frac{1}{2} \frac{\Delta x_1 \Delta x_2}{(\Delta x_1)^2 + (\Delta x_2)^2} - (1-\nu) \tan^{-1} \left(\frac{\Delta x_1}{\Delta x_2} \right) \right\} \quad (5-3)$$

$$u_2^i(x_\alpha) = \frac{\|\mathbf{b}^i\|}{2\pi(1-\nu)} \left\{ \frac{1}{2} \frac{(\Delta x_2)^2}{(\Delta x_1)^2 + (\Delta x_2)^2} - \frac{1}{4} (1-2\nu) \ln \frac{(\Delta x_1)^2 + (\Delta x_2)^2}{(b^i)^2} \right\} \quad (5-4)$$

where

$$\Delta x_\alpha = x_\alpha - X_\alpha^i \quad (\alpha = 1, 2)$$

The corresponding in-plane stress field components $\sigma_{\alpha\beta}^i$ are

$$\sigma_{11}^i(x_\alpha) = -\frac{\mu\|\mathbf{b}^i\|}{2\pi(1-\nu)} \frac{\Delta x_2 [3(\Delta x_1)^2 + (\Delta x_2)^2]}{[(\Delta x_1)^2 + (\Delta x_2)^2]^2} \quad (5-5)$$

$$\sigma_{22}^i(x_\alpha) = \frac{\mu\|\mathbf{b}^i\|}{2\pi(1-\nu)} \frac{\Delta x_2 [(\Delta x_1)^2 - (\Delta x_2)^2]}{[(\Delta x_1)^2 + (\Delta x_2)^2]^2} \quad (5-6)$$

$$\sigma_{12}^i(x_\alpha) = \frac{\mu\|\mathbf{b}^i\|}{2\pi(1-\nu)} \frac{\Delta x_1 [(\Delta x_1)^2 - (\Delta x_2)^2]}{[(\Delta x_1)^2 + (\Delta x_2)^2]^2} \quad (5-7)$$

On the update of the dislocations, the Peach-Koehler (P-K) force p^i is the driving force for changes in the dislocation structure. Considering the motion of the dislocations on the slip planes,

$$p^i = (\mathbf{m}^i)^T \cdot (\hat{\boldsymbol{\sigma}} + \sum_{j \neq i}^N \tilde{\boldsymbol{\sigma}}) \cdot \mathbf{b}^i \quad (5-8)$$

If \mathbf{b}^i is the unit Burgers vector, this equation also denotes the resolved shear stress, τ^i , on the slip plane containing dislocation i . Using a linear drag relation, the magnitude of the velocity of dislocation v^i is taken to be linearly related to the Peach-Koehler force

$$p^i = Bv^i \quad (5-9)$$

where B is the drag coefficient. In a given time step Δt , the dislocations are moved by $v^i \Delta t$. In order to avoid big numerical oscillations, a velocity cap is used so that the dislocation motion within one time step can not be too large. Opposite signed dislocations should move along the opposite direction. The positions of the dislocations are then updated.

Problem II: The image continuum field enforces the boundary conditions that resulted from the dislocation motions in an infinite homogeneous elastic material.

The continuum field is a well posed boundary value problem and is solved by GIMP. The boundary conditions are:

$$\text{Surface traction: } \hat{\mathbf{T}} = \mathbf{T}_0 - \tilde{\mathbf{T}} \quad (5-10)$$

$$\text{Displacement: } \hat{\mathbf{u}} = \mathbf{u}_0 - \tilde{\mathbf{u}}, \quad (5-11)$$

The constitutive equation for this field is linear elasticity, given by,

$$\hat{\boldsymbol{\sigma}} = \mathbf{C} : \hat{\boldsymbol{\varepsilon}} \quad (5-12)$$

As for the dislocation interactions, the long range interactions between dislocations are accounted through the continuum elasticity fields as described in “Problem I”. The short range interactions are represented by a set of constitutive rules (van der Giessen and Needleman, 1995), including the following:

Dislocation nucleation: The material is initially free of dislocations, but contains dislocation sources. Assume dislocation sources are point sources on the slip plane, which generate a dislocation dipole when the magnitude of the shear stress at the source $|\tau^i|$, computed by Eq. (5-8), has exceeded the critical stress τ_{nuc} during a period of time, t_{nuc} . As shown in Fig. 5-1, if the resolved shear stress $\tau^i > 0$, then a positive dislocation

$b^i > 0$ is generated in the direction of \mathbf{n}^i ; the dislocation signs change when $\tau^i < 0$. The distance L_{nuc} between the two dislocations is determined such that the total resolved shear stress τ_{nuc} balances the shear stress that the two dislocations exert on each other, i. e., by setting $\sigma_{12}^i(x_\alpha) = \tau_{nuc}$, $\Delta x_1 = L_{nuc}$, $\Delta x_2 = 0$, we get

$$L_{nuc} = \frac{\mu}{2\pi(1-\nu)} \frac{b}{\tau_{nuc}} \quad (5-13)$$

If the shear strength of the dislocation source, τ_{nuc} , is the same for all the sources, a sudden burst of dislocations will occur, which is not very realistic. Therefore, the strength of the dislocation sources is randomly chosen from a Gaussian distribution with a mean strength of $\bar{\tau}_{nuc} = 50$ MPa and a standard deviation of $0.2 \bar{\tau}_{nuc}$ (van der Giessen and Needleman, 1995). Corresponding to a mean nucleation distance of $L_{nuc} = 125 b$ and b is specified to have the value 0.25nm for the Burgers vector for copper (Cleveringa *et al.*, 1999).

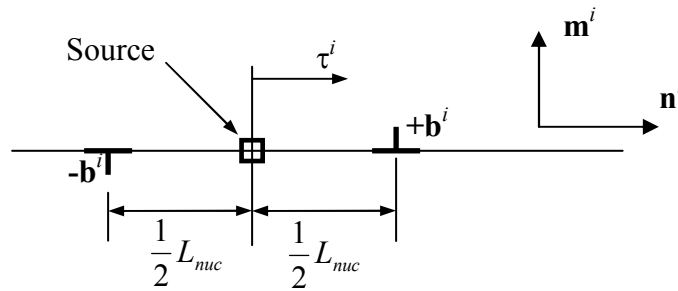


Fig. 5-1: Illustration of a dislocation source and a pair of dislocation dipole

Dislocation annihilation: Two edge dislocations with opposite Burgers vector will annihilate each other when they have approached within a material-dependent, critical annihilation distance L_e . L_e is specified as $6 b$ (Cleveringa *et al.*, 1999).

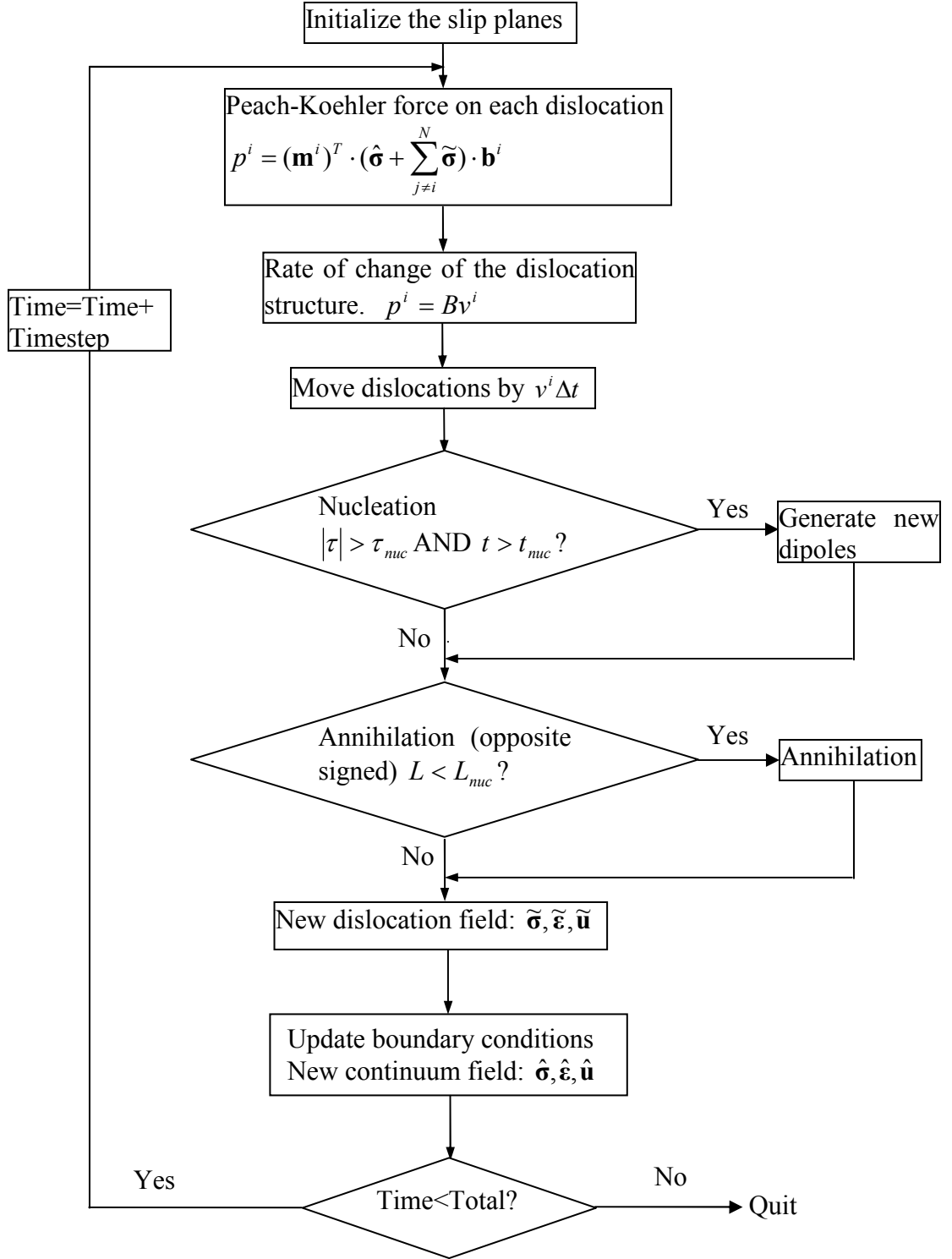


Fig. 5-2: Flow chart of dislocation dynamics calculation

Each time step involves three main computational stages: (i) calculation of the forces on the dislocations, i.e. the Peach-Koehler force; (ii) determination of the change

of the dislocation structure, which involves the nucleation of new dislocations, the motion of dislocations and their mutual annihilation; and (iii) updating of the stress and strain state for the new dislocation arrangement. The flow chart for the code is given in Fig. 5-2.

5.2.2 Model verification

In order to validate the coupling algorithm between GIMP and DD, uniaxial tension and bending problems are modeled.

5.2.2.1 Uniaxial tension simulation

The dimensions of the copper workpiece for the uniaxial tension model are given in Fig. 5-3. A uniform pressure of 500 MPa is applied to both sides of the bar. The workpiece is initially seeded with dislocation sources at random locations, one source on each slip plane. The slip plane distance is $100 b$, where b is the magnitude of the Burgers vector. To simplify calculations, only one direction (45°) of slip plane is used in this example although there are three slip plane directions in a 2D representation for FCC crystals in realistic situation. The simulation parameters (Cleveringa *et al.*, 1999) are shown in Table 5-1.

Table 5-1. Material parameters for the discrete dislocation calculations
(Cleveringa *et al.*, 1999)

Drag coefficient, B	Crit. Nucleation. shear stress, τ_{nuc}	Crit. Nucleation. Time, t_{nuc}	Crit. Annihilation. Distance, L_{nuc}	Elastic properties
1.5×10^{-4} $Pa \cdot s$	$N(\bar{\tau}_{nuc}, 0.2 \bar{\tau}_{nuc})$ $\bar{\tau}_{nuc} = 50 \text{ MPa}$	0.1 ns ($\Delta t = 0.5 \text{ ps}$)	6b (b = 0.25nm)	E = 70 GPa $\nu = 0.33$

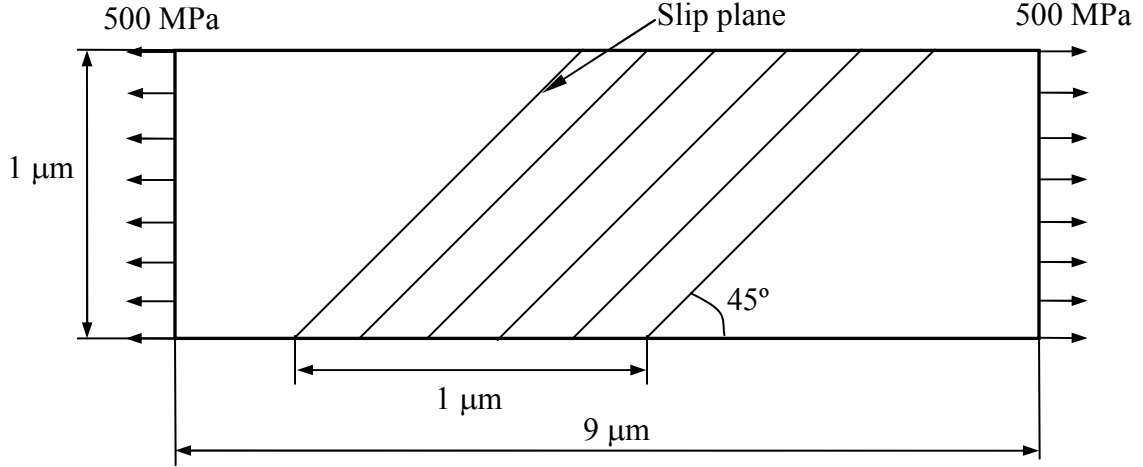


Fig. 5-3: Schematic of initial model setup for uniaxial tension

Fig. 5-4 shows the distribution of the seeded dislocation sources at time $t = 0$. There are totally 29 sources and their locations do not change throughout the simulation. Fig. 5-5 shows the stress distributions at 50,000 steps (one time step is 0.5 ps). The total stress field σ_{xx} [Fig. 5-5 (a)] is the sum of the continuum stress field [Fig. 5-5 (b)] and dislocation stress field [Fig. 5-5 (c)]. It can be seen from Fig. 5-5 (a) that at the left and right boundaries of the workpiece, the magnitude of the stress is approximately 500 MPa, which is the applied pressure. The continuum stress field is the stress at each material point from regular continuum mechanics calculation. The dislocation stress field is computed at each material point using Eq. (5-2).

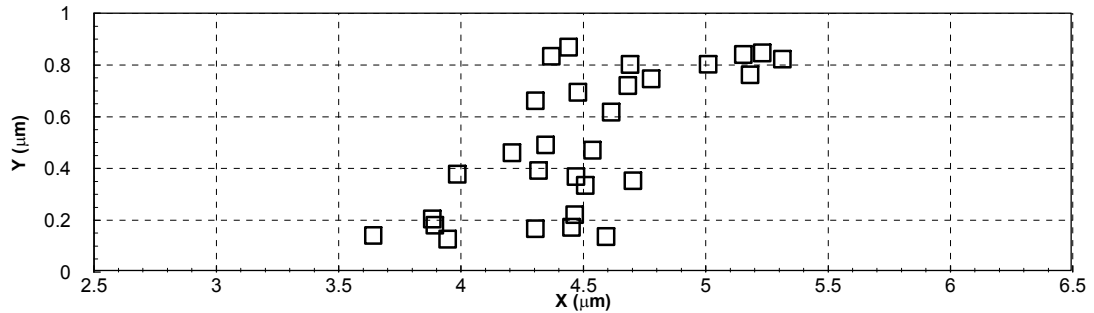


Fig. 5-4: Distribution of the dislocation sources

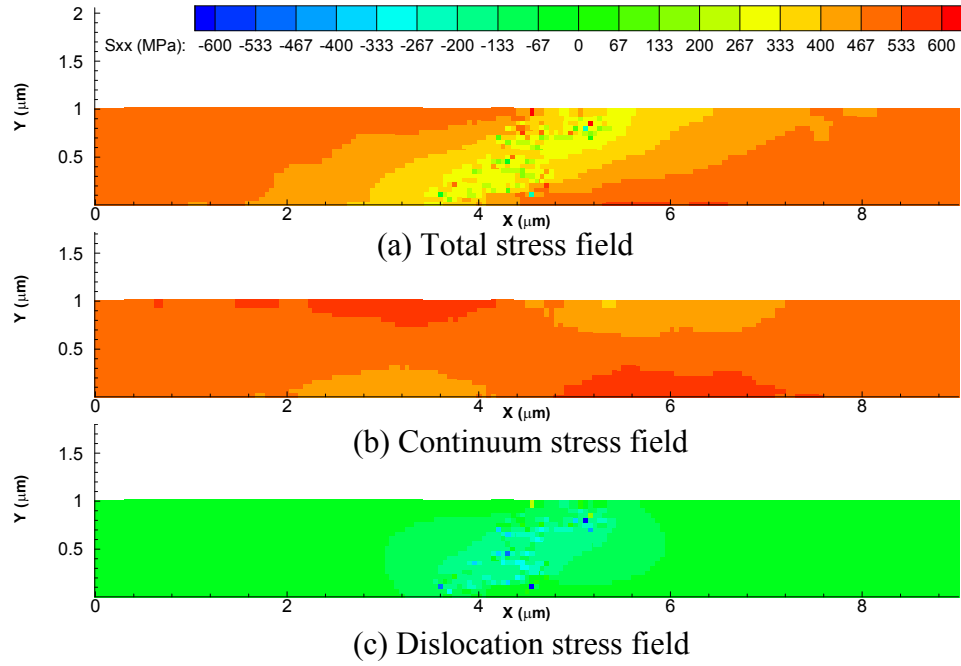


Fig. 5-5: Distribution of the normal stress σ_{xx} at step 50, 000

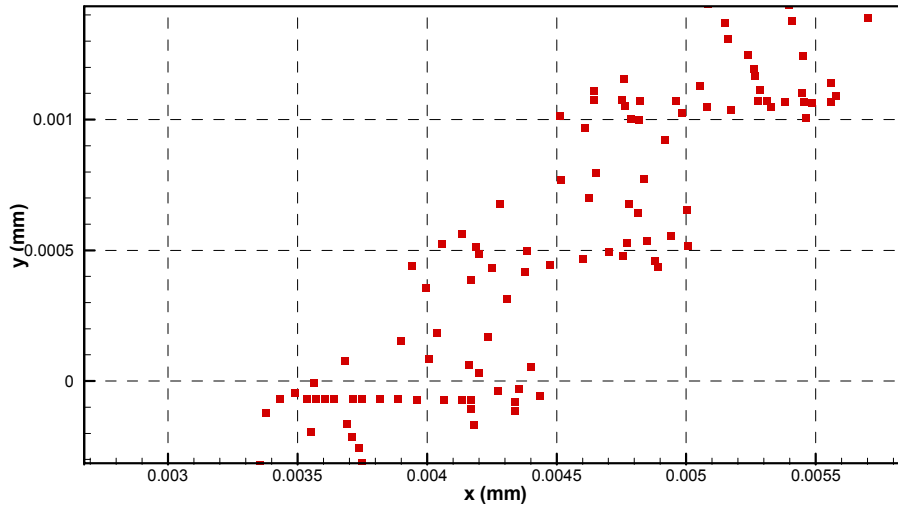


Fig. 5-6: Distribution of dislocations at step 50,000

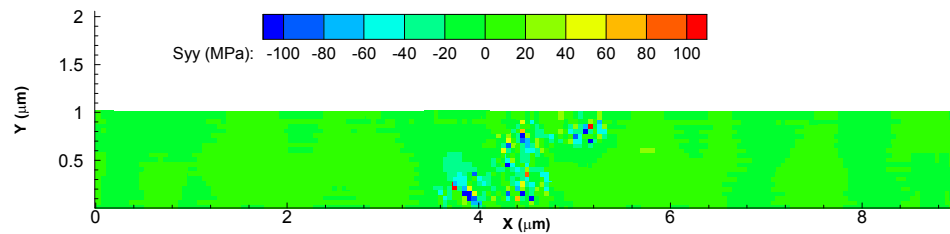


Fig. 5-7: Total σ_{yy} field in the tension specimen at step 50,000

Fig. 5-6 shows the distribution of the discrete dislocations at 50,000 time steps. Some of the dislocations have moved out of the physical boundary of the workpiece. This is permitted because the dislocation space is infinite. Fig. 5-7 shows the total stress field of σ_{yy} . It can be seen that σ_{yy} is zero on the top and bottom surfaces. This indicates that the traction free boundary condition is satisfied.

5.2.2.2 Bending simulation

The dimensions of the workpiece for bending model are given in Fig. 5-8. A bending moment $M = 0.125$ mN per unit thickness is applied to the bar. To validate multiple slip systems, three slip plane directions in a 2D representation for FCC crystals are employed. The workpiece is initially seeded with dislocation sources one on each slip plane at random locations. The slip plane distance is $100b$. The simulation parameters are given in Table 5-1. There are totally 280,000 steps. Fig. 5-9 shows the distribution of the dislocation sources at random locations on the slip planes.

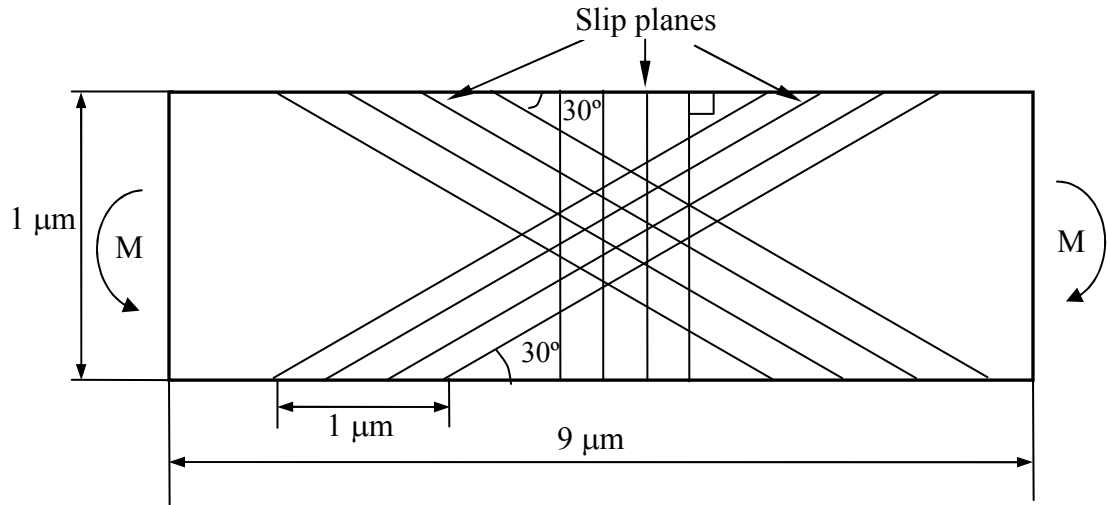


Fig. 5-8: Schematic of initial model setup for bending

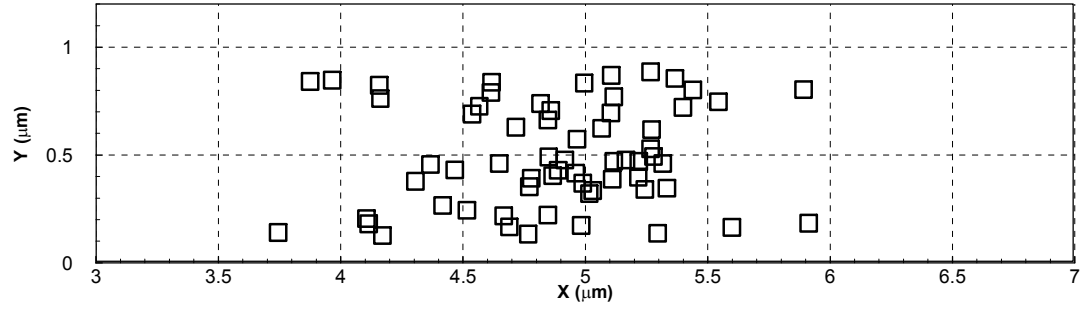


Fig. 5-9: Distribution of the dislocation sources

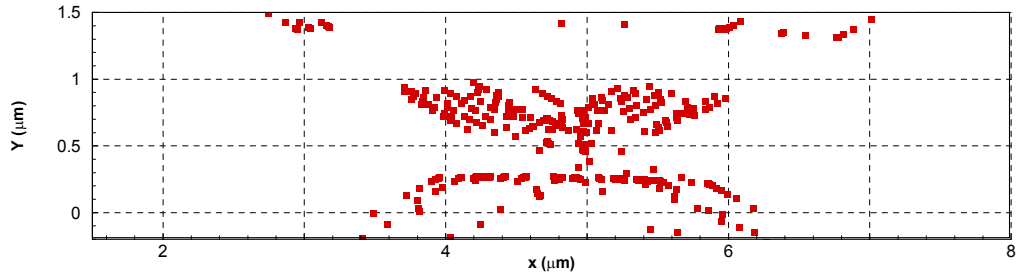


Fig. 5-10: Distribution of dislocations at step 280, 000

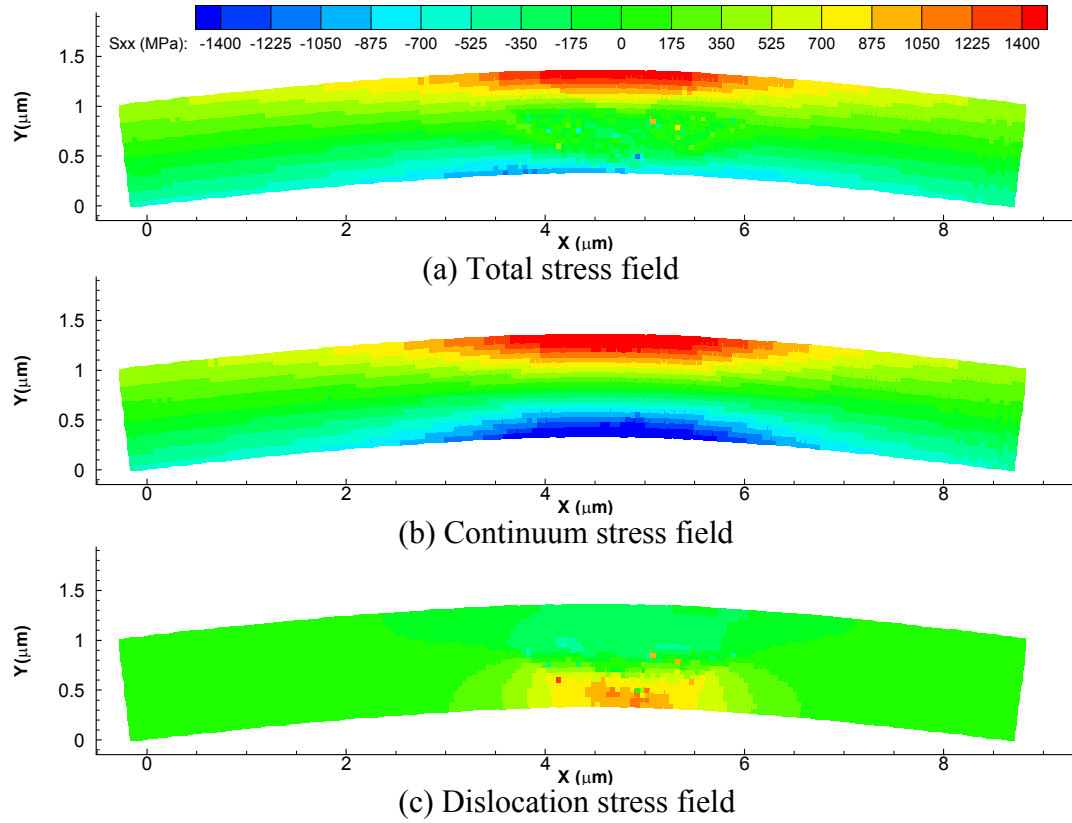


Fig. 5-11: Distribution of the normal stress, σ_{xx} at step 280, 000

Fig. 5-10 shows the distributions of the dislocations at the end of the simulation. Fig. 5-11 (a) shows the distribution of the total stress field σ_{xx} , which is the superposition of the continuum and discrete dislocation field. It may be noted that the continuum stress field [Fig. 5-11 (b)] is continuous while the dislocation stress field [Fig. 5-11 (c)] is somewhat singular. It can be seen that the top of the specimen is subjected to tension while the bottom is subjected to compression. In the center region of the specimen, stress distribution is not continuous due to the presentation of dislocations.

5.3 Coupling of GIMP, DD and MD

Based on the validated coupling scheme between GIMP and DD, DD is coupled with the GIMP and MD coupling to formulate a full multiscale simulation framework. Ma *et al.* (2005, 2006) conducted a multiscale simulation bridging the continuum scale using GIMP method and the atomistic scale using MD in 2D using the multilevel refinement technique in a parallel computing environment. When it comes to dislocation modeling, dislocations are generated from dislocation sources in GIMP and DD coupling. In the realistic situation, they are nucleated in the MD region once the atom deformation is sufficiently large. Hence, one of the key issues in the coupling of GIMP, MD and DD is to detect dislocations in the MD region in real time and pass them onto the continuum region.

5.3.1 Dislocation detection and passing from atomistic region to continuum region

a) Dislocation detection

In order to detect dislocations when they are nucleated in the MD region and then pass them onto the continuum region, the method proposed by Shilkrot *et al.* (2004) was used in this investigation of coupling GIMP and MD. Several layers of atoms at the

border of MD and continuum region form the detection band elements which are triangular in shape. During deformation, the Lagrangian strain tensor, \mathbf{E} of an element in the detection band is given by (Shilkrot *et al.*, 2004)

$$\mathbf{E} = \frac{1}{2}[\mathbf{F}^T \mathbf{F} - \mathbf{I}], \quad (5-14)$$

where \mathbf{I} is the second order identity tensor, \mathbf{F} is the deformation gradient tensor can be decomposed into

$$\mathbf{F} = \mathbf{F}^e \mathbf{F}^p. \quad (5-15)$$

In Eq. (5-15), \mathbf{F}^e is related to the lattice stretching while \mathbf{F}^p corresponds to the plastic shearing of the slip systems of the crystal. For the case of ideal slip deformation, $\mathbf{F}^e = \mathbf{I}$. \mathbf{F}^p can be represented by

$$\mathbf{F}^p = \mathbf{R} \left(\mathbf{I} + \frac{\mathbf{b} \otimes \mathbf{m}}{d} \right), \quad (5-16)$$

where \mathbf{R} is the lattice rotation and d is the interplanar distance. Substituting Eq. (5-16) into Eq. (5-14), we get the plastic slip strain tensor as

$$\mathbf{E}^p = \frac{1}{2}[(\mathbf{F}^p)^T \mathbf{F}^p - \mathbf{I}] = \frac{(\mathbf{b} \otimes \mathbf{m})_{sym}}{d} + \frac{(\mathbf{m} \otimes \mathbf{b})(\mathbf{b} \otimes \mathbf{m})}{2d^2} \quad (5-17)$$

For each of the detection band elements, both the actual strain \mathbf{E} and the plastic slip strain \mathbf{E}^p are computed after the positions of the atoms are updated at each computational step. The norm L_2 represents the difference between the actual strain and the plastic slip strain.

$$L_2 = \sqrt{(\mathbf{E} - \mathbf{E}_i^p) : (\mathbf{E} - \mathbf{E}_i^p)} \quad (5-18)$$

If the zero Burgers vector ($\mathbf{b}=\mathbf{0}$) minimizes L_2 , no dislocations are detected. Otherwise, the core of the detected dislocation is assigned to the centroid of the detection band element. For 2D triangular lattices, \mathbf{E} can be computed from constant strain triangles as in FEM.

b) Dislocation passing

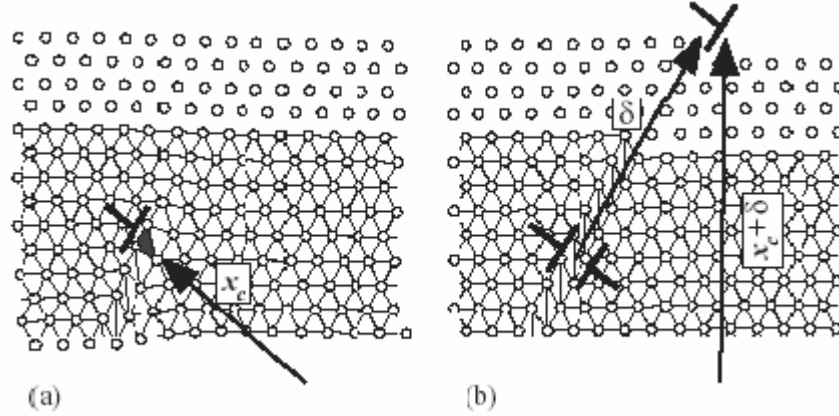


Fig. 5-12: Passing of atomic dislocations to the continuum region (Shilkrot *et al.*, 2004).

If a dislocation is generated in the detection band element at \mathbf{x}_c , as shown in Fig. 5-12, the location \mathbf{d}^i , slip plane \mathbf{m}^i and Burgers vector \mathbf{b}^i are recorded. By passing the dislocations into the continuum region, the displacements on the atoms and particles are modified. As a result, the dislocation core at the atomistic region is annihilated and a continuum dislocation is generated at position $\mathbf{x}_c + \delta$ [see Fig. 5-12 (b)]. Generally, δ is a vector on the order of several lattice spacings to ensure the effect of the dislocation dipole is only short-ranged.

5.3.2 Coupling algorithm

At the continuum scale, the generalized interpolation material point (GIMP) method is used. Fig. 5-13 illustrates the coupling scheme in which the atomistic region is

embedded in the continuum region, as shown in Fig. 5-13 (a). A transition region, where the communication between the two regions takes place, is constructed by overlapping the material points and the atoms by certain width and is divided into three zones, namely, the inner zone, the “incommunicado” zone, and the outer zone, as shown in Fig. 5-13 (b). A common background grid is used to carry out the communication by interpolating the physical quantities, such as the velocity and forces, back and forth between the continuum region and the atomistic region. The material points in the inner zone, shown in Fig. 5-13 (b), are updated from atomistic simulation, and then join the rest of the material points in the GIMP simulation. The velocities of the atoms in the outer zone are updated by the continuum region, and then boundary conditions are provided for the MD simulation.

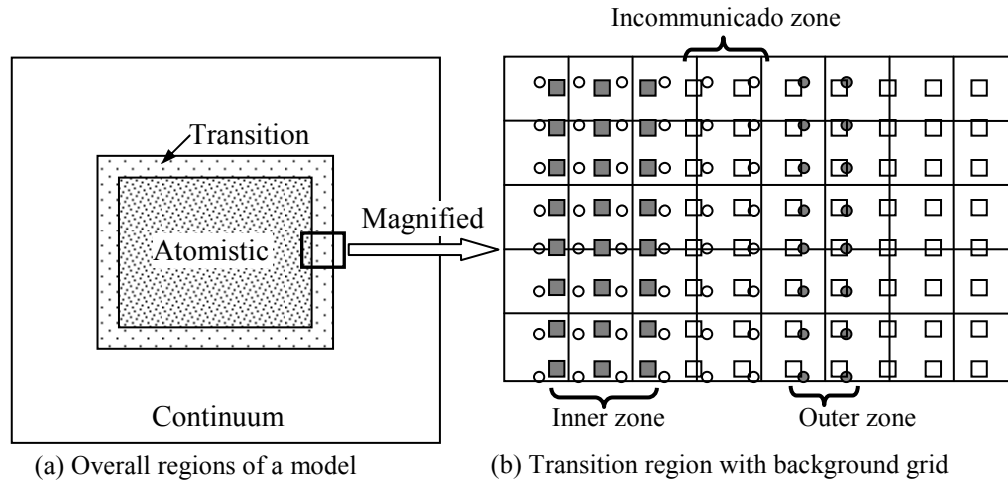


Fig. 5-13: Illustration of coupled GIMP and MD simulations. The circles represent atoms and the squares (smaller than physical size) represent material points. The material points connect to each other without a gap to represent the continuum (Ma *et al.*, 2006)

Refinement algorithms in GIMP have been developed to split the material points to the size of atoms at the transition region to achieve seamless coupling. However, if dislocations cannot be modeled explicitly in the continuum region, the atomistic region

has to be large enough so that the dislocations do not propagate to the transition region to allow the continuum region to remain elastic.

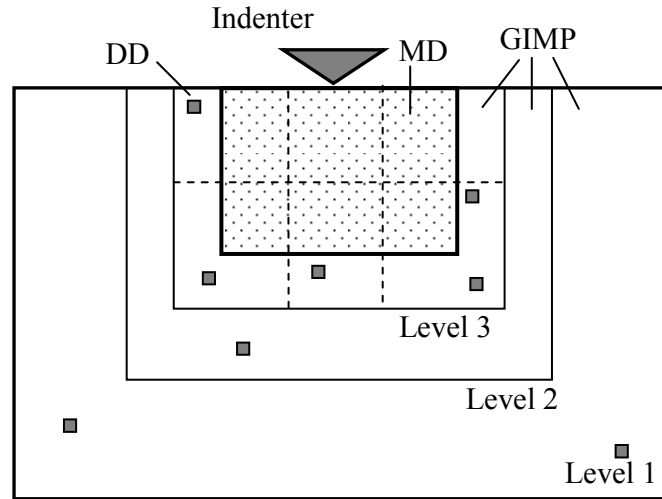


Fig. 5-14: Illustration of the domain decomposition and refinement for the coupling simulation of 2D indentation using GIMP, DD and MD

Fig. 5-14 is a schematic of an indentation problem used in the coupling simulation. The area immediately beneath the indenter is modeled by MD. Three levels of successive refinements in GIMP are shown with the finest level decomposed into six rectangular patches. Other levels are also divided into six patches, however, these patches are not shown. To reduce data transfer among the processors in coupling, the MD region is decomposed into six rectangular regions. Each MD region in coupling is assigned to a patch residing in the same processor as used for the simulation of a GIMP region. Thus, each processor handles both MD and GIMP regions in coupling. Although using the same domain decomposition for MD and GIMP in the finest level does not produce the best load balance among the processors, this approach is simple to implement and effective in the communication between GIMP and MD in the transition region. This is because

material points and atoms in exchange of information are stored and processed by the same processor. Hence, no inter-processor communication is necessary.

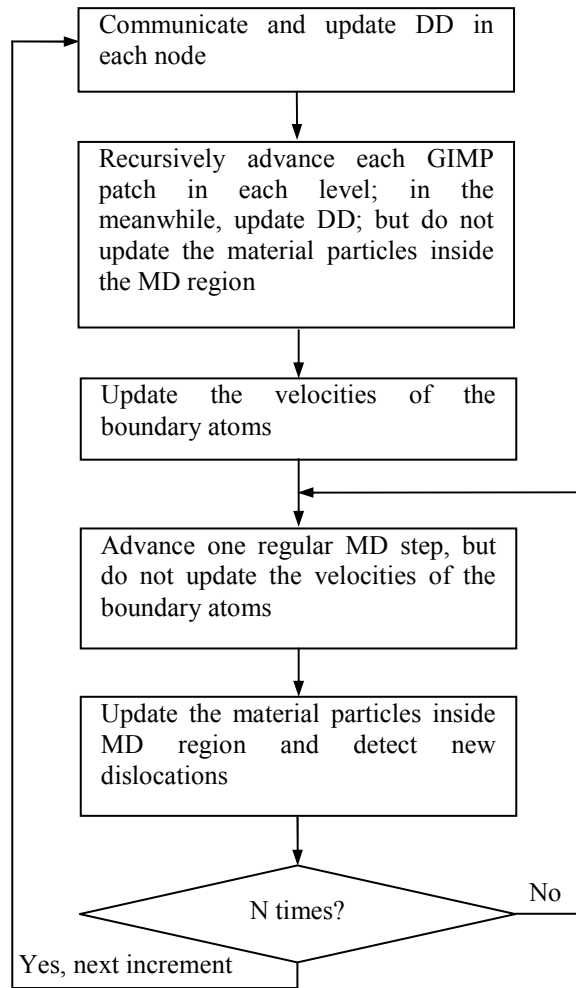


Fig. 5-15: Flowchart of the coupling algorithm for each increment

When discrete dislocations, shown as small squares in Fig. 5-14, are introduced into the model, we keep the domain decomposition intact. Fig. 5-15 shows the overall flowchart of the coupling algorithm incorporating GIMP, DD and MD. Each DD is updated within each patch where it resides because the local continuum stress is needed to compute the Peach-Koehler force applied on it. A parallel processing algorithm, based on SAMRAI (Structured Adaptive Mesh Refinement Application Infrastructure), which is the code developing at the Lawrence Livermore National Laboratory for exploring

parallel computing, and software issues associated with structured adaptive mesh refinement, was implemented for discrete dislocation.

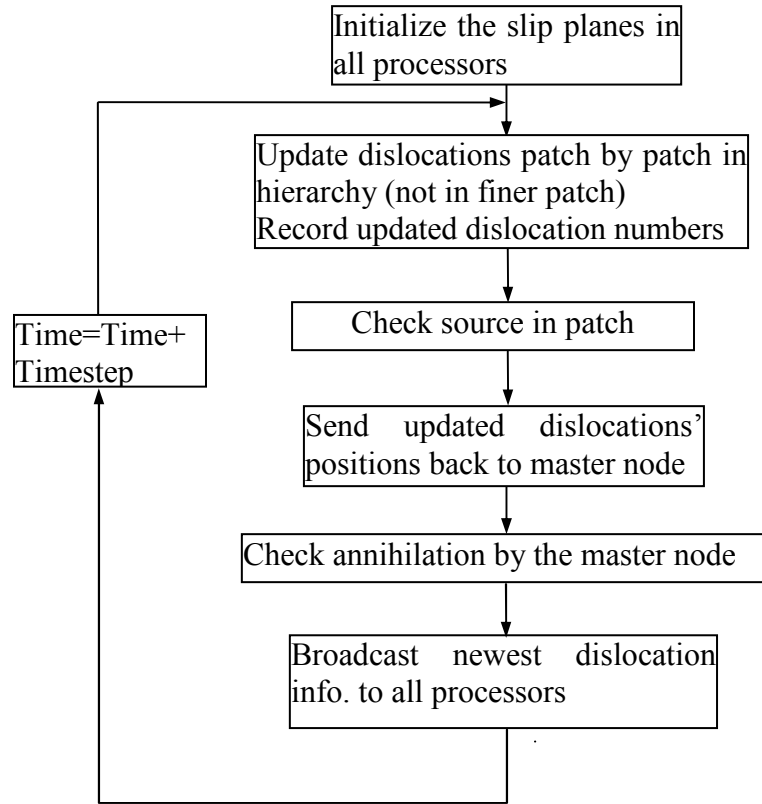


Fig. 5-16: Flowchart for the parallel process of dislocation dynamics

The flow chart for the coupling algorithm for each increment is shown in Fig. 5-16. Because the long-range forces from all other DDs have to be computed, i.e., loop all the DDs, we store the updated information of all the DDs in each processor. Hence, inter-processor communication can be avoided. The cost is that after each step, i.e., after all patches in each level and the DDs are updated, the updated DD information has to be transmitted to other processors. To achieve this, initially, each processor sends the local updated DD information, including newly created DDs, to one master node and the master node assembles all the updated dislocations. Next, the master node broadcasts all the dislocation information to all other processors. It may be noted that each dislocation

carries a position and a Burgers vector and the communication overhead is usually negligible compared to GIMP and MD computations.

5.4 Multiscale simulation of nanoindentation

5.4.1 Simulations at 0° K temperature

When a long rigid wedge indenter is indented into a workpiece, the middle section can be assumed to be in the plane-strain condition. In this investigation, as shown in Fig. 5-17, the indentations were performed along the $[\bar{1}\bar{1}2]$ direction on the FCC copper uses the embedded atom method (EAM) potential (Daw and Baskes, 1984). This problem was modeled as a 2D indentation on the (111) plane. The drag coefficient B in Eq. (5-9) for copper is taken at 1.5×10^{-4} Pa·s (Fusenig and Nembach, 1975). The simulations were conducted at 0° K.

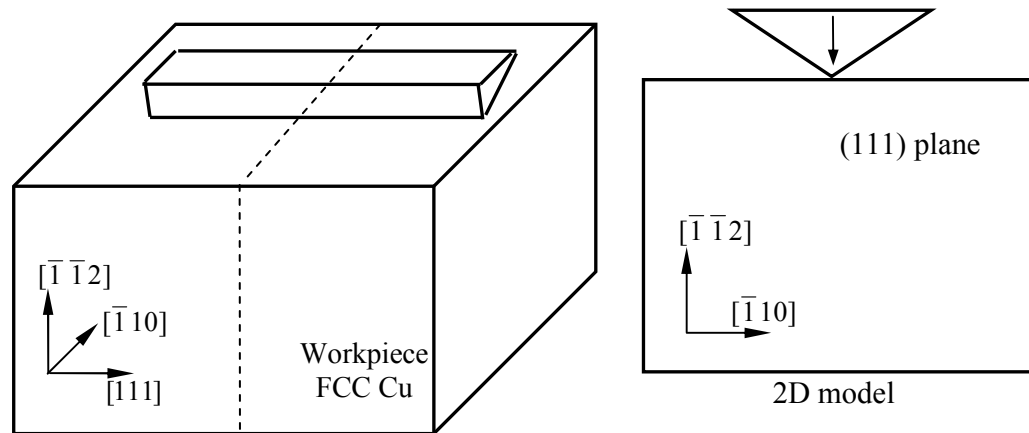


Fig. 5-17: 2D modeling of an indentation problem with a wedge indenter

A wedge indenter with an included tip angle of 120 degrees was used in the simulation. The first slippage was initiated at a depth of ~ 4 Å. More slippage was developed subsequently along the three possible slip directions. Significant amount of slip was developed on the contact surface, resulting in the pile-ups of the material.

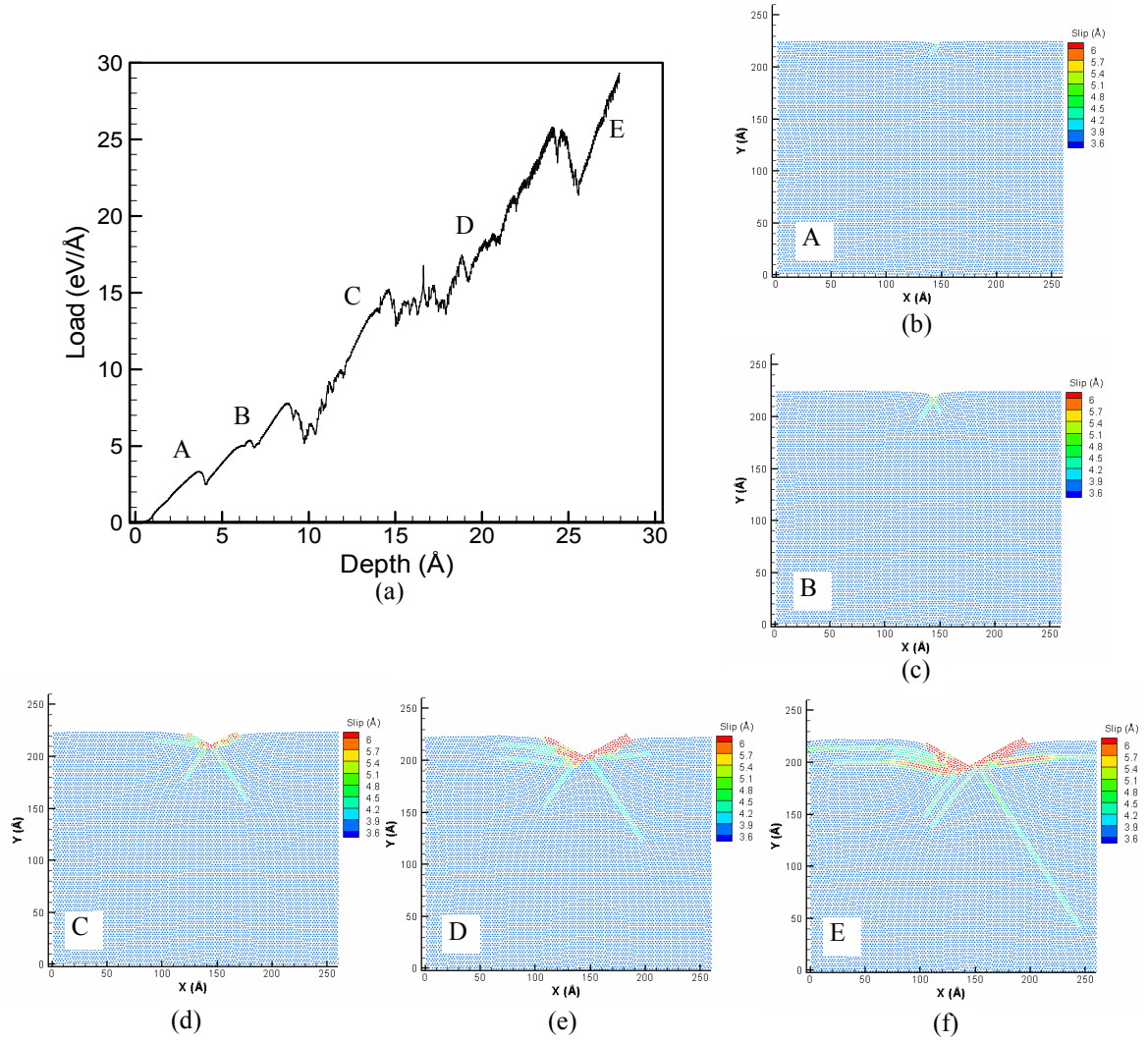


Fig. 5-18: (a) Load-displacement curve using a wedge indenter; (b)-(f) Workpiece showing the indent and generation of dislocations at different stage of indentation

Fig. 5-18 (a) shows a typical load-displacement curve from simulation. The initial loading curve is relatively smooth and no dislocations were observed in the atomistic region up to an indentation depth of ~ 4 Å. The atom distribution corresponding to point A is plotted in Fig. 5-18 (b). At the first drop, point B in the load-displacement curve, dislocation twinning below the indenter was observed, shown as in Fig. 5-18 (c). The first dislocation moves along the $[10\bar{1}]$ direction. The other dislocations are nucleated

immediately after the first one and they move along $[01\bar{1}]$ direction. These two dislocations have advanced in a straight path as the indenter continues to indent into the workpiece. The workpiece stiffens until the next set are generated at points C and D with these states shown in Fig. 5-18 (d) and (e) in the $[\bar{1}\bar{1}0]$ and $[\bar{1}10]$ directions. All subsequent dislocations are in these four possible directions and the workpiece softens when each dislocation was generated below the indenter.

5.4.2 Finite temperature

In conducting multiscale simulations at finite temperatures, thermal vibrations of atoms can cause adverse effects in coupling because vibrations can generate instantaneous oscillations in the magnitude of strain and stress. Thermostat algorithms have been proposed in the literature (Bernstein *et al.*, 2000; Plimpton, 2005) to control thermal vibrations by removing some kinetic energy in the MD system. For example, the atom velocities can be rescaled to keep the instantaneous temperature at a constant (Bernstein *et al.*, 2000; Plimpton, 2005), or a damping factor can be used to dissipate extra kinetic energy (Jang and Voth, 1997; Shiari *et al.*, 2005). Since the instantaneous temperature is proportional to the kinetic energy, and the MD region is relatively small in coupling, the temperature can increase quickly in the simulation of indentation when the indentation velocity is high. Fig. 5-19 shows the temperature change during simulation of 2337 Cu atoms using a wedge indenter at three indentation velocities, namely, 36, 180, and 360 m/s. At the indentation velocity of 360 m/s, large portion of atoms has started to translate at the same simulation time, resulting in higher instantaneous temperatures.

Shiari *et al.* (2005) reported a similar phenomenon with a cylindrical indenter at an indentation speed of 3000 m/s.

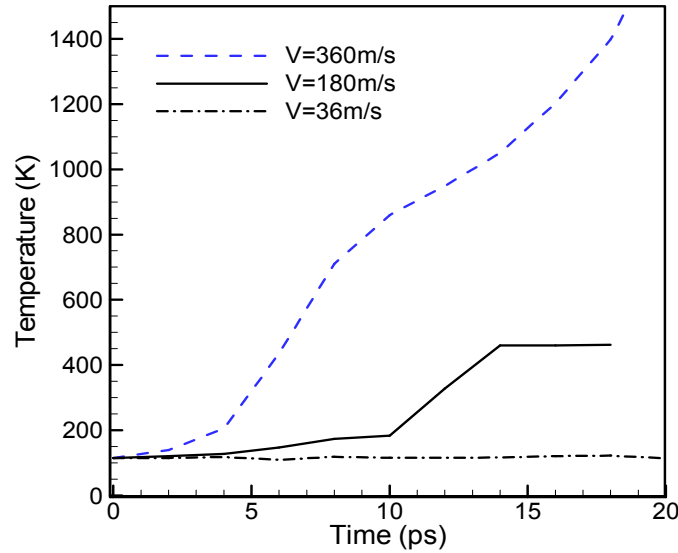


Fig. 5-19: Instantaneous temperatures as a function of time at different indentation velocities

The atom velocities are composed of two parts, one representing the thermal vibration and the other representing deformation and translation. Thermostat algorithms do not distinguish between these two. Ideally, the deformation part of the velocity should not be altered in the coupling simulation in order to maintain displacement compatibility with the continuum region. Filtering algorithms, such as moving time average and Fourier transform, can be used to separate the thermal vibration from deformation/translational motion in the frequency domain. However, these algorithms require storage of history data for each atom and they are very intensive computational for coupling simulations.

In this investigation, in order to maintain displacement compatibility between the continuum and atomistic regions, thermostat algorithms are not used. To minimize the effect due to atomic vibrations in the transition region, a spatial average velocity of each

atom in the inner zone is used. The average velocity is computed with the first nearest neighboring atoms. For the 2D triangular lattice, each atom has six first nearest neighboring atoms. In addition, the process of interpolating atom velocities to the background grid can reduce the atom vibrations because each background node receives interpolation from multiple atoms. This technique does not allow heat exchange between MD and GIMP and it is only suitable for problems that do not involve much temperature change in nature, such as the indentation problem.

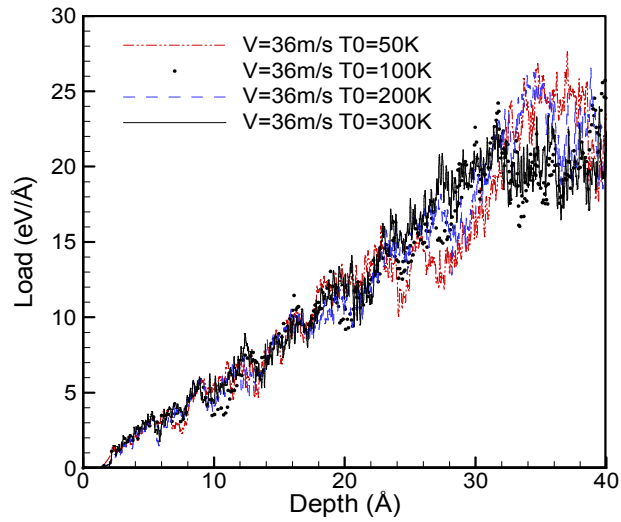


Fig. 5-20: Load-displacement curves at different temperatures using a wedge indenter

Fig. 5-20 shows the load-displacement curves at different temperatures. The indentation velocity was chosen as 36 m/s because the instantaneous temperature does not vary much at this speed, as can be seen in Fig. 5-19. The load-displacement curves at the four initial temperatures overlap each other. The onset of dislocations appears to be independent of temperature when a wedge indenter is used. Shiari *et al.* (2005) reported strong dependence of the onset of dislocations on the temperature when a cylindrical indenter was used. The coupled simulations in this work show similar temperature

dependence in slip patterns. Fig. 5-21 shows the slip patterns at a simulation time of 50 ps and an indentation depth of 18 Å at four temperatures, namely, 50, 100, 200 and 300 K. It can be seen that the slip patterns are different at different temperatures even when the applied indentation load is nearly identical.

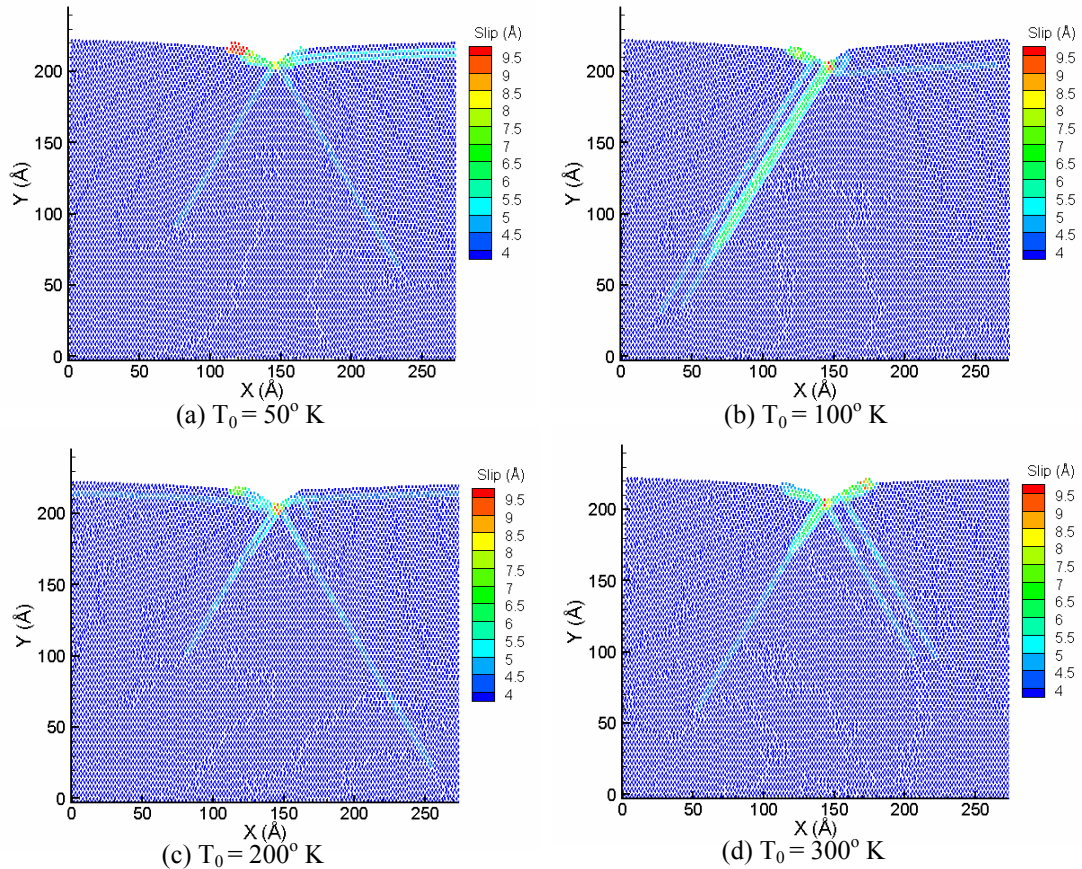


Fig. 5-21: Slip patterns at different temperatures when the indentation depth is 18 Å

5.5 Conclusions

In this chapter, the dislocation dynamics (DD) method is adopted for multiscale simulation. Dislocation dynamics can effectively model the dislocations and their interactions at the mesoscale. In coupling with continuum mechanics, discrete dislocations are assumed to be in the infinite elastic medium. Dislocation motions are governed by the continuum stress field and the interactions of all dislocations. Principle

of superposition is used to solve the problem in the domain of interest. In fact, the continuum mechanics computation is performed with the actual applied boundary conditions subtract the traction and displacement on the boundary generated by the dislocations.

Dislocations from MD simulation can be detected and passed onto the continuum using the method proposed by Shilkrot *et al.*, 2004. Hence, dislocation dynamics links the MD simulation and continuum simulation seamlessly. A multiscale simulation algorithm that couples MD, DD and GIMP was developed for material simulations with parallel processing based on domain decomposition. In parallel processing, each processor updates all the material points, discrete dislocations, and atoms in its sub-domain (Ma *et al.*, 2006). The coupling algorithm is used to simulate the indentation on Cu (111) plane with a wedge indenter. Dislocation nucleation and subsequent propagation of dislocations are observed for the indentation simulation. Spatial averaging technique is used to maintain displacement compatibility at finite temperatures. In the transition region, the atom velocity is averaged with six nearest neighboring atoms in 2D for coupling to reduce the adverse effect of thermal vibrations on the continuum region. This technique is appropriate for simulation of problems under isothermal conditions, such as nanoindentation.

Chapter 6

MD Simulations of Atomic Friction

6.1 Introduction

In previous chapters, material behaviour is modeled at the mesoscale. In this chapter, simulation approach is scaled down to the atomic level and molecular dynamics (MD) simulations are used to study the atomic-scale friction between two plates that are in contact and sliding against each other.

Atomic-scale friction is of considerable importance to understand the frictional aspects in nanotribology. Many industrial processes require a detailed understanding of tribology at the nanometer scale. The development of lubricants in the automobile industry depends on the adhesion of nanometer layers to a material surface. Assembly of components can depend critically on the adhesion of materials at the nanometer length scale. In the information technology (IT) industries of semiconductor and data storage, nanotribological studies help optimize the design of the magnetic head and media surface.

MD simulations were initiated in the late 1950's by Alder and Wainwright (1959) using hard-core potentials in the field of statistical mechanics. Since then, the approach has been applied to a wide range of applications, including the study of phase transitions and dynamics of microscopic defects in solids. In MD simulations, the behavior of atoms is traced during a short timescale with short-range interaction, which is generally described by an atomic potential function. The motion of the atoms is computed by

integrating the equations of motion given by Newton's second law. With the growing availability of computing power, MD simulation is becoming a powerful tool in simulation of material behavior.

Perry and Harrison (1995) used an empirical hydrocarbon potential, developed by Brenner *et al.* (1991), to examine friction that occurs when the (100)-(2 × 1) reconstructed surfaces of two diamond lattices that are placed in sliding contact. They performed a series of MD simulations to study the effects of applied load, crystallographic sliding direction, and sliding velocity. At high applied loads, the atomistic sliding mechanisms began to vary depending mainly on whether or not the stick-slip phenomena occurred. It was concluded that decreasing the sliding velocity by an order of magnitude did not significantly affect the coefficient of friction; however, the atomic-scale friction mechanism was altered for sliding.

Holian *et al.* (1998) conducted non-equilibrium MD simulations on high-speed friction between dry metal interfaces. The results showed surprising similarities between shockwave loading and high-speed friction. Shimizu *et al.* (1998) modeled the atomic-scale stick-slip phenomenon between the specimen and slider using Morse potential and concluded that MD simulation has an advantage in deciding the spring constant of cantilevers in AFM. Ohzono and Fujihira (2000) simulated the molecular stick-slip motion and the frictional anisotropy observed experimentally between an AFM tip and an ordered monolayer of n-alkane chains. Djuidje Kenmoe and Kofane (2007) studied the frictional stick-slip dynamics theoretically and numerically in a model of one oscillator interacting with a nonsinusoidal subtracted potential. Their study suggested the motion of the particle involves periodic stick-slip, erratic and intermittent motions, characterized by

force fluctuations, and sliding, depending on the model shape parameter. Ma *et al.* (2006) briefly presented atomic friction of two sliding plates using MD simulations and a multiscale simulation formulation bridging the continuum scale using the generalized interpolation material point (GIMP) method and the atomistic scale using MD. This work is a comprehensive study based on Ma *et al.* (2006) using MD simulations.

Frictional sliding along an interface between two identical isotropic elastic plates under impact shear loading (Coker *et al.*, 2005) was investigated experimentally and numerically at the continuum scale. The experiments exhibited both crack-like and pulse-like modes of sliding. Plane stress finite element modeling of the experimental configuration was carried out and a variety of sliding modes are obtained depending on the impact velocity, initial compressive stress, and values of interface variables.

6.2 MD simulation of friction

MD code used in this investigation is the LAMMPS code developed by the Sandia National Laboratories (Plimpton, 2005). It can be used to model atomistic behavior or, more generically, as a parallel particle simulator at the meso and continuum levels. LAMMPS runs on both single-processor machines and in parallel using message-passing techniques and a spatial-decomposition of the simulation domain. The atomic potential chosen is the Lennard-Jones potential given by

$$u(r) = 4\varepsilon_0 \left[\left(\frac{\sigma}{r} \right)^{12} - \left(\frac{\sigma}{r} \right)^6 \right], \quad (6-1)$$

where ε_0 is the depth of the potential well, σ is the finite distance at which the interparticle force is zero, and r is distance between two atoms. In Eq. (6-1), the

$\left(\frac{1}{r}\right)^{12}$ term describes repulsion and the $\left(\frac{1}{r}\right)^6$ term describes attraction. In the simulations, $\varepsilon_0 = 1.0$, $\sigma = 1$ and the mass of each atom m_a is assumed to be 1. The cut off radius is 2.5. Dimensionless MD units are used in this study [see, Allen and Tildesley (1989)] and therefore, the units for time, velocity, and stress/pressure are $\sigma\sqrt{\frac{m_a}{\varepsilon_0}}$, $\sqrt{\frac{\varepsilon_0}{m_a}}$ and $\sqrt{\frac{\varepsilon_0}{\sigma^3}}$, respectively. The potential in Eq. (6-1) gives the longitudinal wave speed $c_l = 8.99$, the shear wave speed $c_s = 5.19$, and the Rayleigh wave speed $c_R = 4.8$.

The atomic friction between two plates of the same material (artificial material) at a temperature of 0° K was simulated by applying shearing velocities of opposite directions on top and bottom halves on the left side of the model as shown in Fig. 6-1. A 2D triangular lattice is used in the simulations. The model has 600 lattices in the X-direction and 400 lattices in the Y-direction. The size of the model is $\sim 670 \times 770$ and there are totally 480,001 atoms in the model. The simulations are carried out on a Linux Boewulf cluster with six nodes. The interface was assumed to be atomically smooth and the friction/interaction was governed by the pairwise L-J interaction with a break radius that is significantly less than the cut-off radius. The break radius defines a distance within which the atoms have interaction. It only affects the atoms above and below the interface in a pair in this study. In other words, if both atoms are beyond the interface zone, normal cut-off radius applies. Therefore, the interface is a weak zone compared to the interior of each block. The setup models a shear crack growth along the weak plane and it is analogous to dynamic friction problem. To avoid contact and penetration of the free

interfaces, a small velocity V_y was applied on the left boundary, the magnitude of which is 0.3% of the V_{x0} (see Fig. 6-1). At the right, both the top and bottom surfaces were constrained in the Y-direction to avoid possible rotation of the model in the simulation. The right side is constrained in the X-direction to eliminate the stress wave generated by the free surface in MD simulations. The time step is 0.002 and the total steps vary from 50,000 to 100,000, depending on the applied shearing velocity.

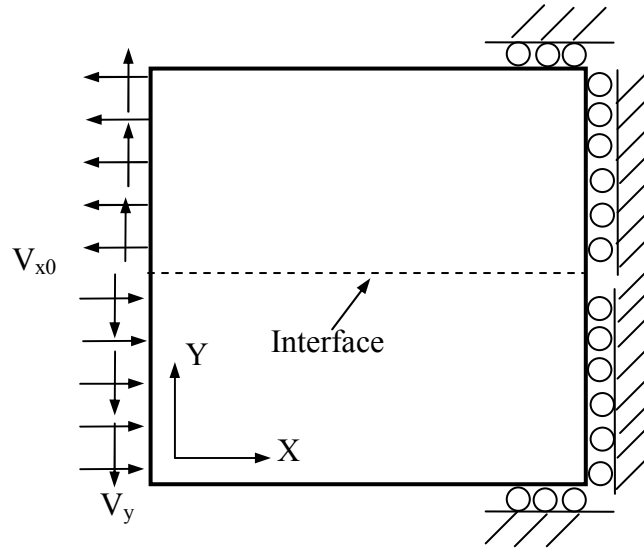


Fig. 6-1: Applied boundary conditions for the MD simulations of the atomic friction problem

Parametric studies on the simulation parameters, including the shearing velocity (V_{x0}) and break radius (r) are conducted through numerical experiments to investigate the frictional behavior at the interface of the two plates. Five different shearing velocities, varying from 0.0005 and 0.01, and three break radii varying from 1.2 to 1.6 are used. The results and findings are reported in the next section.

6.3 Numerical results

Fig. 6-2 shows the contours of V_x in the computational domain at various times for $V_{x0} = 0.006$ and $r = 1.6$. The evolvement of the stick-slip phenomenon is observed. At

$t = 100$ in Fig. 6-2 (a), the first slipping spot was seen and subsequent spots were seen in Fig. 6-2 (b)-(e). At $t = 500$ in Fig. 6-2 (e), five slipping spots were seen along the

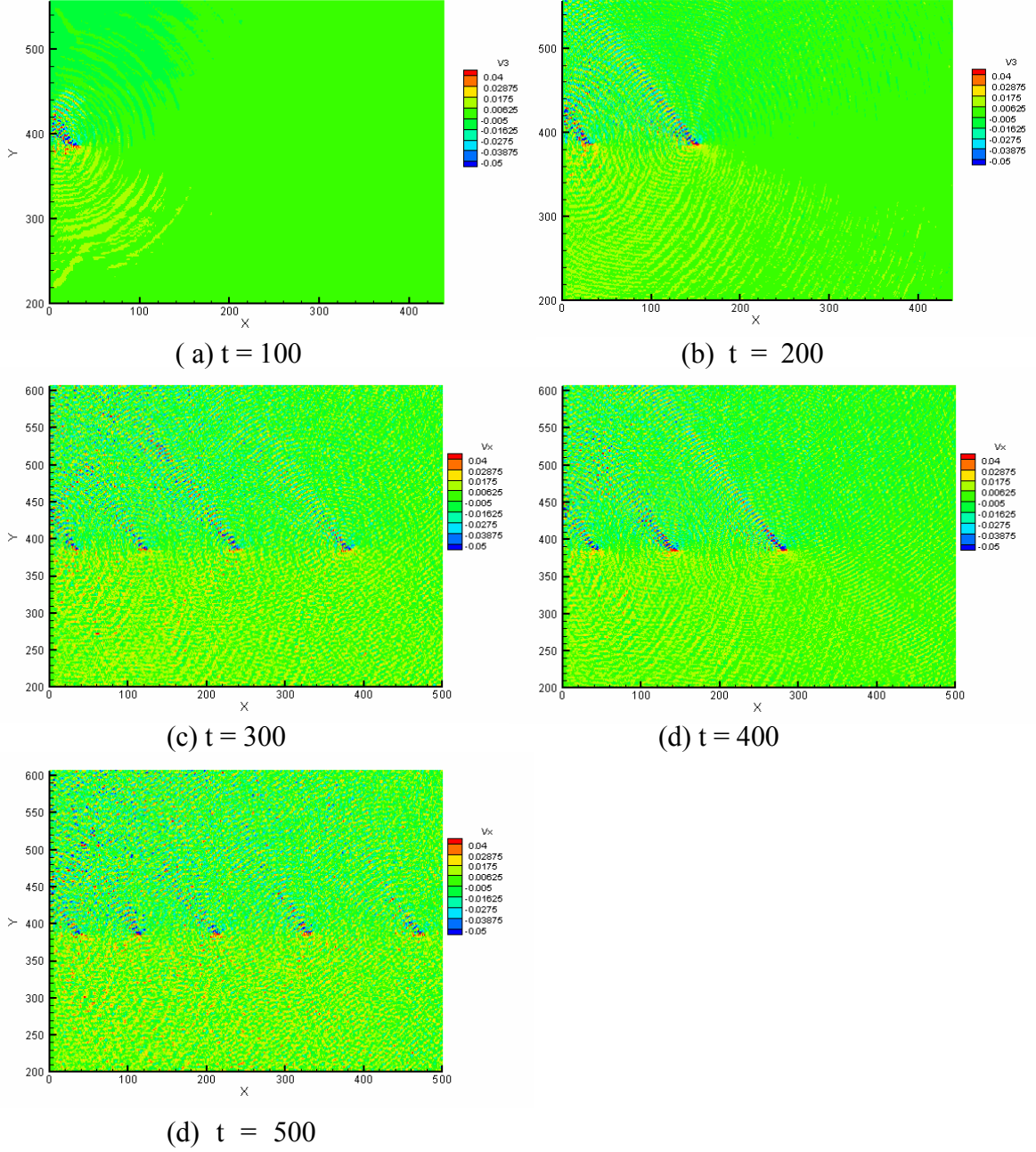


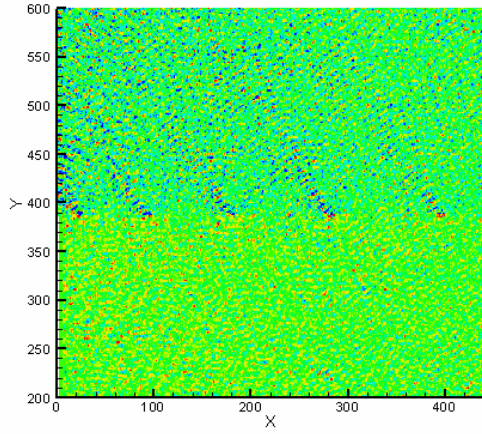
Fig. 6-2: Evolution of the slip pulses over time for $V_{x0} = 0.006$ and $r = 1.6$

interface. It may be noted that the distance between the two neighboring spots decreases as more and more spots occur. For example, the distance between the two spots in Fig.

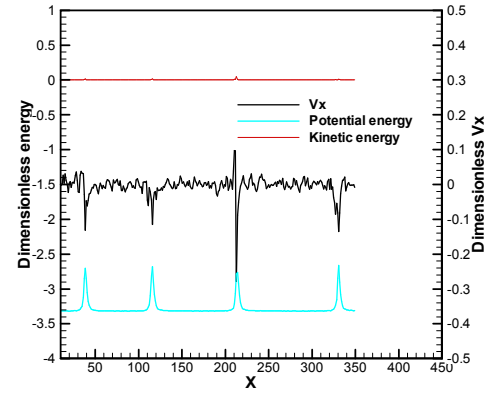
6-2 (b) is ~ 120 , in comparison of ~ 80 between the first two spots on the left in Fig. 6-2 (e). The atoms on different sides of the interface slip against each other at isolated spots along the interface. The atoms below the interface move to the right and the atoms above the interface move to the left. The slipping spots are generated on the left and travel to the right successively, as seen in Fig. 6-2. Between the slipping spots, the interfacial atoms appear to be healed.

Fig. 6-3(a), (c) and (e) show the distributions of the V_x in the two blocks at three different break radii at a fixed shearing velocity, $V_{x0} = 0.01$. Fig. 6-3 (b), (d) and (f) show V_x and kinetic and potential energy distributions along the weak zone for the simulation cases in Fig. 6-3(a), (c) and (e), respectively. Stick-slip phenomenon is seen in Fig. 6-3(a), (c) and (e). As r decreases, the slipping spots tend to connect each other to form a sliding interface, indicating a transition from the stick-slip mode towards the full sliding mode, as observed by Perry and Harrison (1995). As for the energy, at each slipping spot, a spike in potential energy is observed, as seen in Fig. 6-3(b) and (d). The energy eventually transfers to the rest of the lattice and dissipates as heat. In contrast, for $r = 1.2$ [Fig. 6-3(f)], gradual changes in the potential energy are seen as small hills and the width of the hills is about the same as the width of the stick-slip pattern. The smaller the break radius is, the weaker is the interaction between the neighboring atoms on the two sides of the weak zone. And hence, less energy will be generated in sliding contact of the two blocks.

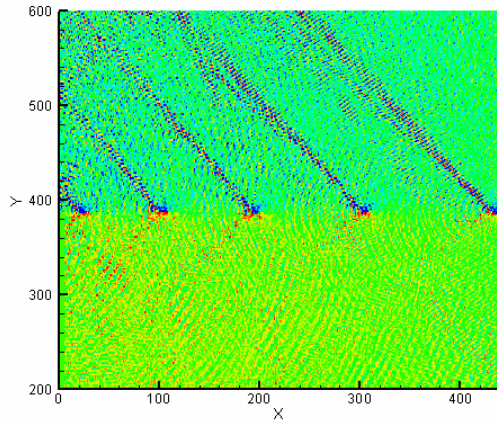
Figs 6-4 to 6-7 show similar results as Fig. 6-3 with decreasing V_{x0} , at 0.006, 0.002 and 0.0005 respectively. At different shearing velocities, the stick-slip patterns show qualitative similarities as those in Fig. 6-3 for the same break radius. For example,



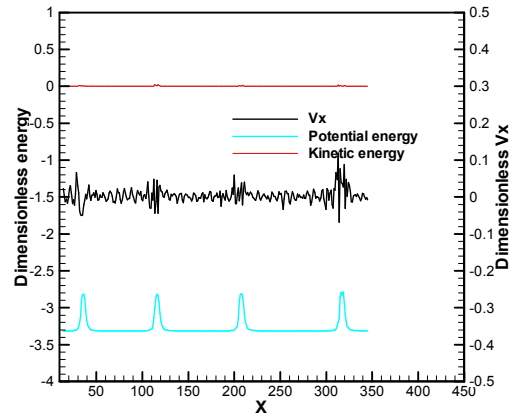
(a) $r = 1.6$



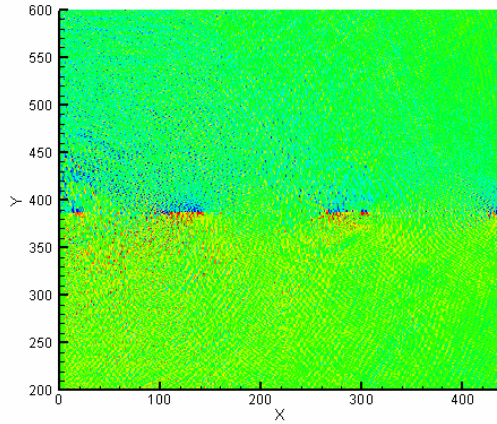
(b)



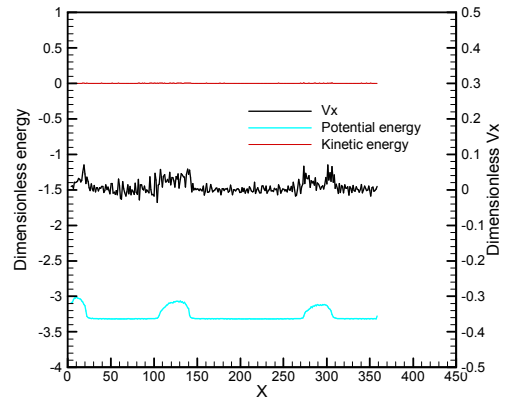
(c) $r = 1.4$



(d)

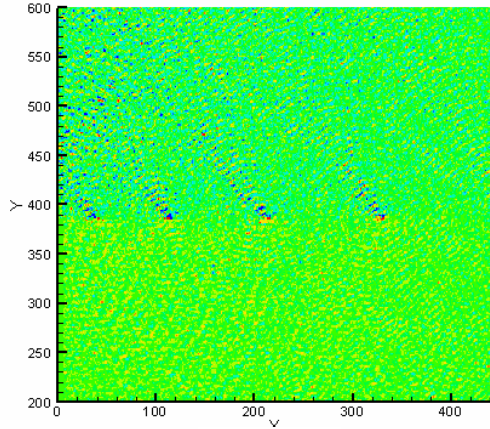


(e) $r = 1.2$

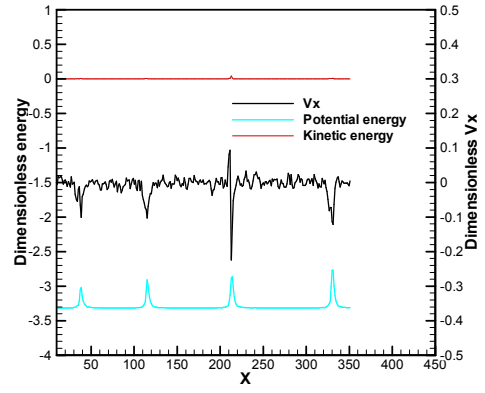


(f)

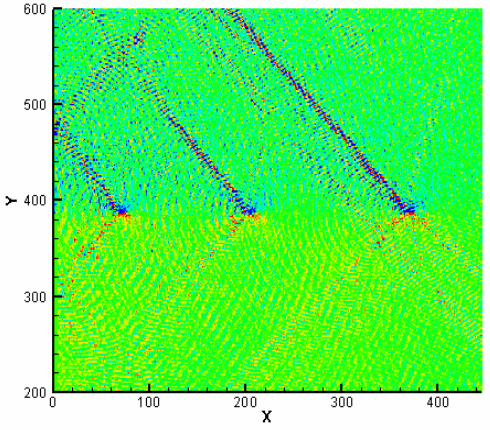
Fig. 6-3: Comparison of the velocity and energy distributions at $V_{x0} = 0.01$ for three break radii, r , namely, 1.2, 1.4, and 1.6



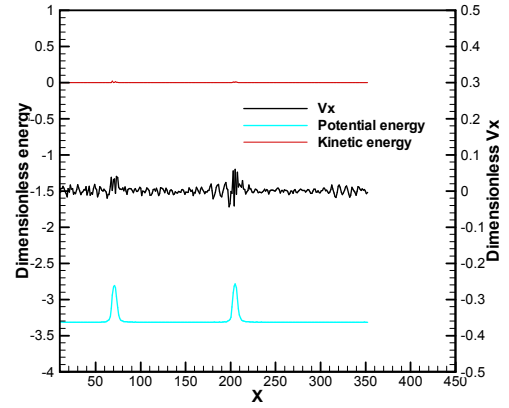
(a) $r = 1.6$



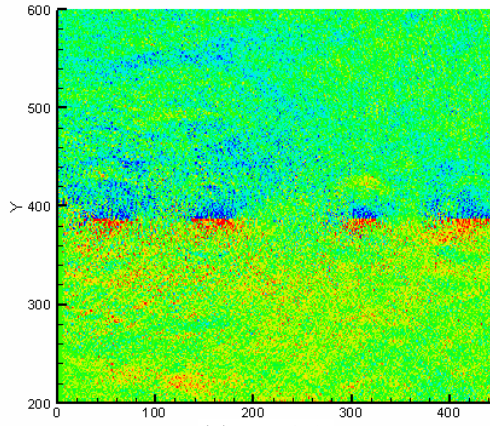
(b)



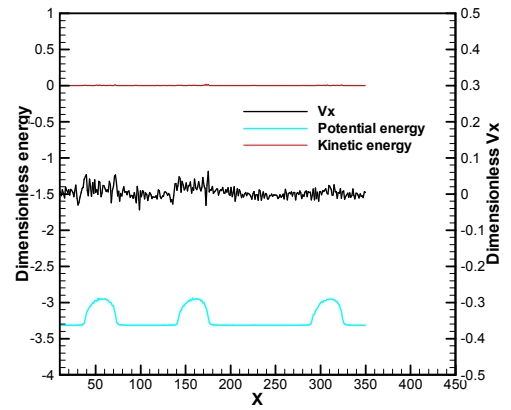
(c) $r = 1.4$



(d)



(e) $r = 1.2$



(f)

Fig. 6-4: Comparison of the velocity and energy distributions at $V_{x0} = 0.006$ for three break radii, r , namely, 1.2, 1.4, and 1.6

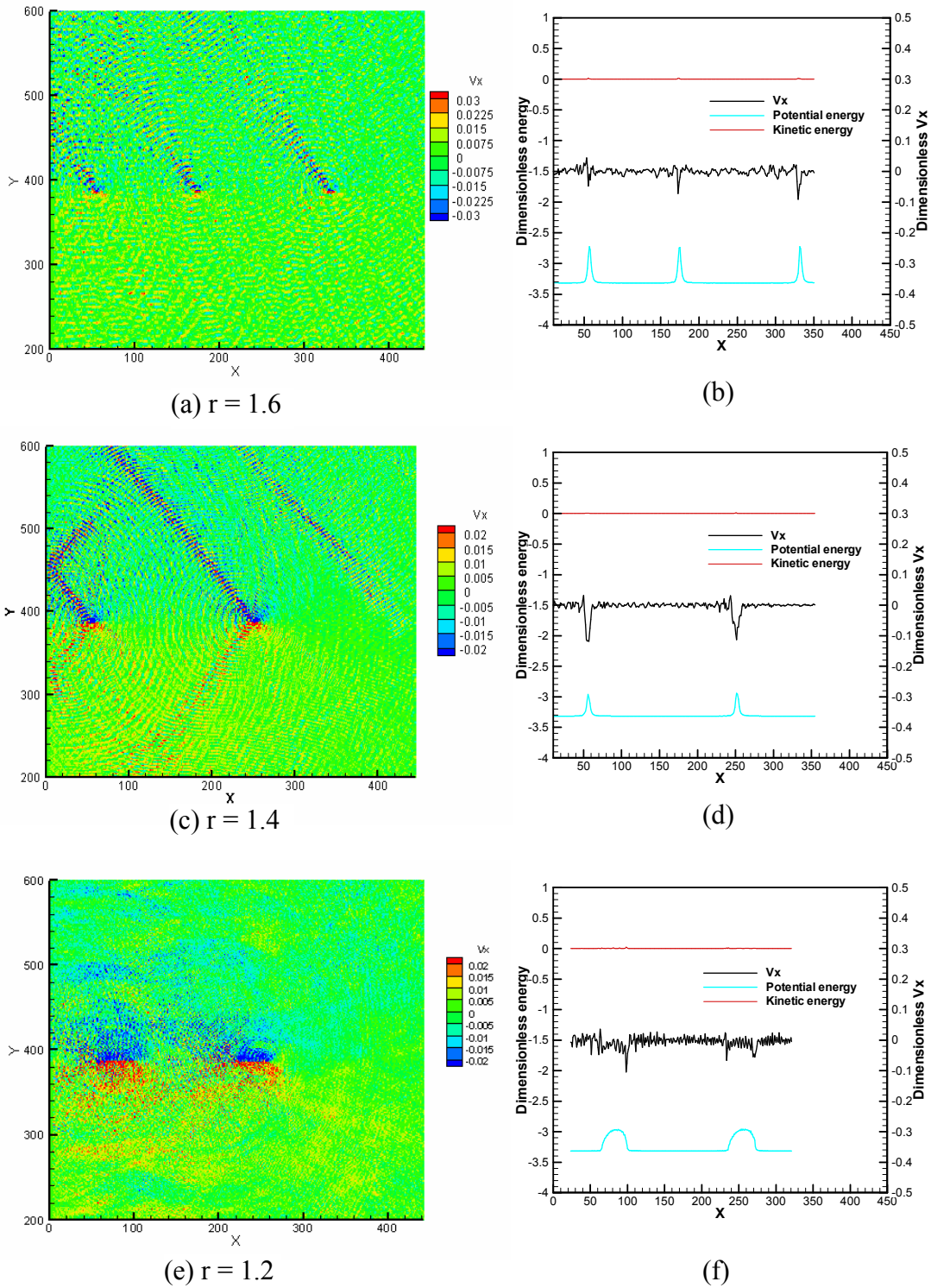


Fig. 6-5: Comparison of the velocity and energy distributions at $V_{x0} = 0.004$ for three break radii, r , namely, 1.2, 1.4, and 1.6

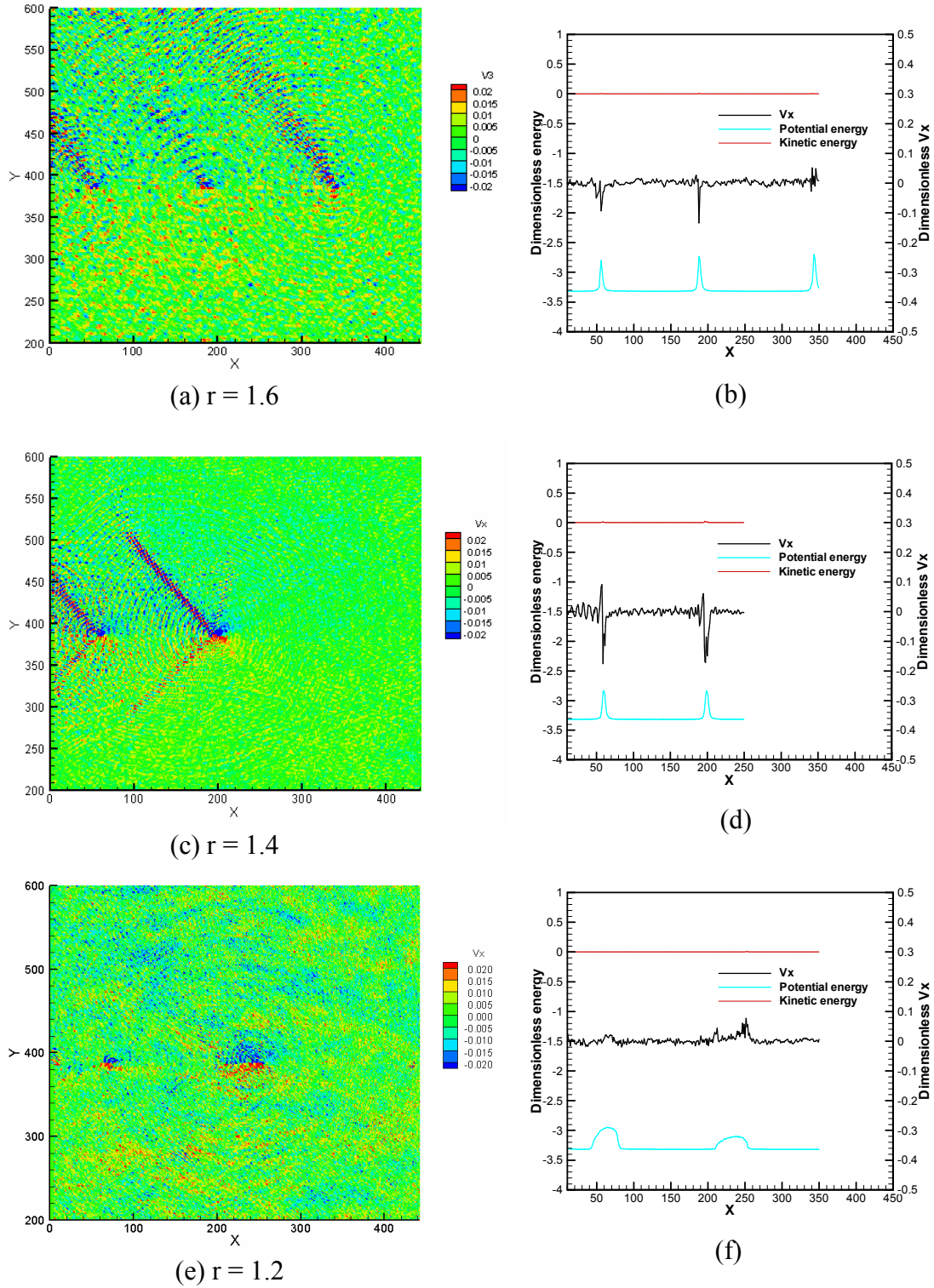
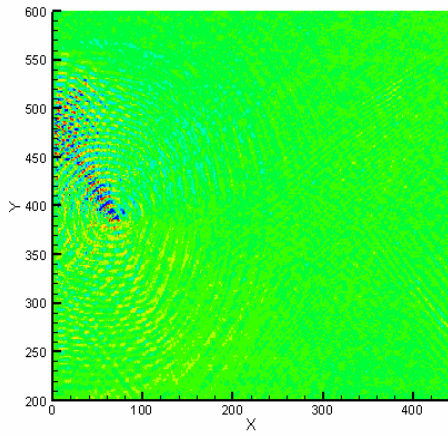
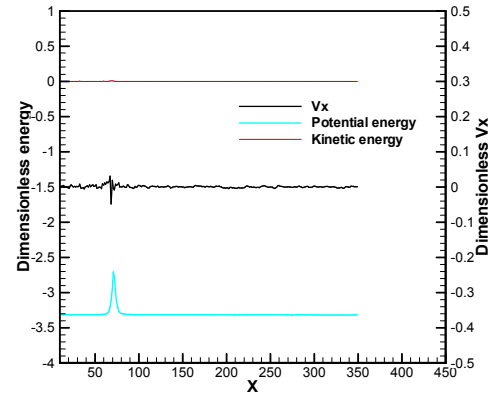


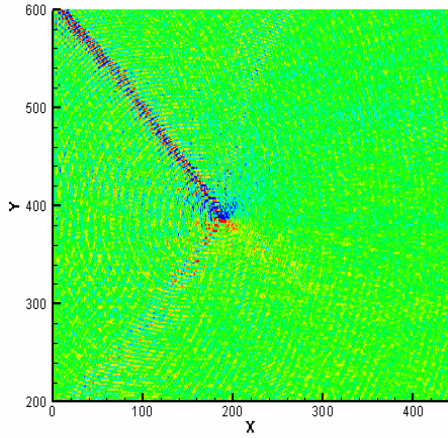
Fig. 6-6: Comparison of the velocity and energy distributions at $V_{x0} = 0.002$ for three break radii, r , namely, 1.2, 1.4, and 1.6



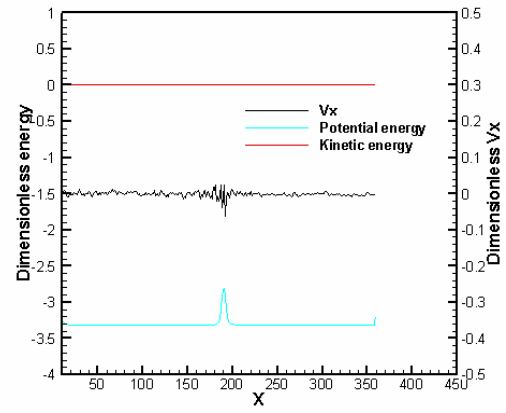
(a) $r = 1.6$



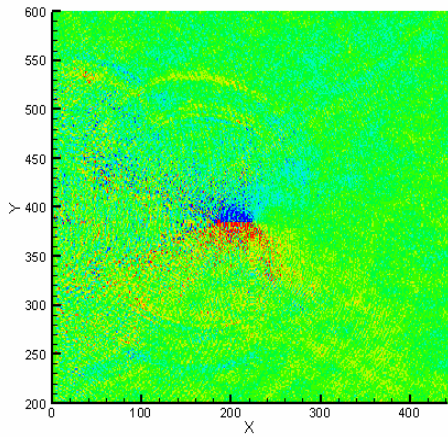
(b)



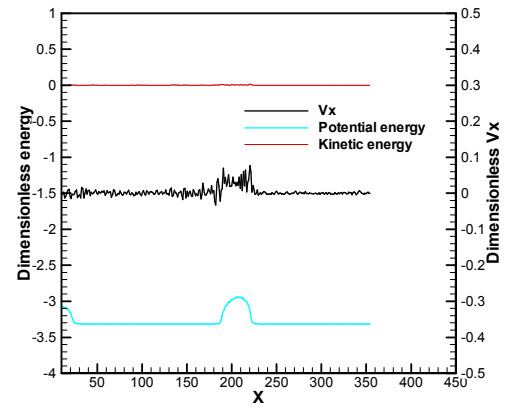
(c) $r = 1.4$



(d)



(e) $r = 1.2$



(f)

Fig. 6-7: Comparison of the velocity and energy distributions at $V_{x0} = 0.0005$ for three break radii, r , namely, 1.2, 1.4, and 1.6

at $r = 1.2$ for all four V_{x0} , slipping spots are wider than those obtained at $r = 1.6$ and $r = 1.4$. However, the slipping spots become more spaced out at smaller shearing velocity, i. e., with decrease in the shearing velocity, fewer slipping spots are generated. For example, there are five slipping spots in Fig. 6-3(c), three in Fig. 6-4(c), two in Fig. 6-5(c) and Fig. 6-6(c), and only one in Fig. 6-7(c). It may be noted that the stick-slip patterns are not perfectly symmetric with respect to the interface. The asymmetry of the applied boundary conditions might contribute to this. Further investigations are needed to determine the reasons for this.

It can be seen from Figs. 6-3 to 6-7 that at the same break radius, the qualitative shape of the velocity, potential, and kinetic energy curves as a function of sliding distance (x) remains virtually unchanged regardless of the shearing velocity, implying that the sliding mechanism is unchanged. In addition, it may be noted that the magnitude of the potential energy spikes does not significantly depend on the shearing velocity V_{x0} . For example, the height of the spikes in Fig. 6-3(d), Fig. 6-5(d), Fig. 6-6(d) and Fig. 6-7(d) is all ~ 0.6 and it is averaged at ~ 0.5 in Fig. 6-4(d). This indicates that there must be enough energy build-up to cause the interfacial atoms to slip in different directions. As the break radius decreases, the energy necessary to cause slip decreases and the relative velocity for the interfacial atoms is reduced.

6.4 Conclusions

In this chapter, the atomic friction between two plates of the same material (model material) at a temperature of 0°K was modeled using MD simulations. The interface was assumed to be atomically smooth and the friction/interaction was governed by the pairwise L-J interaction potential with a break radius that is significantly less than the

cut-off radius. Parametric studies on the simulation parameters, including the shearing velocity (V_{x0}) and break radius (r) are conducted numerically to investigate the frictional behavior at the interface of the two plates. Five different shearing velocities, varying from 0.0005 and 0.01, and three break radii varying from 1.2 to 1.6. As r decreases, the slipping spots tend to connect each other to form a sliding interface, probably indicating a transition from the stick-slip mode towards the full sliding mode. It was observed that at the same break radius, the qualitative shape of the velocity, potential and kinetic energy curves as a function of sliding distance (x) remains virtually unchanged regardless of the shearing velocity, implying that the sliding mechanism is unchanged. It may be noted that the magnitude of the potential energy spikes does not significantly depend on the shearing velocity V_{x0} .

Chapter 7

Conclusions and Future Work

Scaling laws governing the mechanical behavior of materials from atomistic (nano) to continuum (macro) via mesoplastic (micro) are very important to numerous applications, such as the development of a new class of aircraft engine material, or the manufacturing of numerous components for microelectro-mechanical systems (MEMS), mainly because the information on the mechanical behavior of materials at nanolevel is not presently available as inputs to nanotechnology. In this investigation, multiscale modeling and simulations of material properties are addressed considering nanoindentation as an example.

In the framework of multiscale modeling, two modeling techniques at the meso/micro scale are employed to study the mechanical behavior of single crystal materials under nanoindentation, namely, mesoplasticity and discrete dislocation. A combined finite element method (FEM)/nanoindentation approach has been developed to determine the material behavior of single-crystal copper incorporating the mesoplastic constitutive model. Nanoindentation on a single-crystal copper was modeled using mesoplasticity. Numerical and experimental investigations of nanoindentation on single crystal copper in three crystallographic orientations, i. e., (100), (011) and (111) using a spherical (3.4 μm radius) indenter and a Berkovich indenter were reported. Discrete dislocations are coupled with GIMP using the principle of superposition (van der Giessen

and Needleman, 1995). Simulations of indentation were performed on the (111) plane of copper using a wedge indenter. The effects of temperature on the indentation load-depth curves and nucleation of dislocations were investigated.

Two topics are proposed for future work. One is modeling of orthogonal metal cutting using the multiscale simulation model encompassing MD, DD, and GIMP, which is introduced in Chapter 5. The other one is to extend 2D multiscale simulation algorithm into 3D, discussed in Chapter 5, since 3D algorithm at each scale is available. First, generic conclusions based on the investigation of nanoindentation at various length scales encompassing atomistic to continuum via mesoplasticity will be presented followed by suggestion for future work.

7.1 Conclusions

1. At the mesoscale, nanoindentation process was simulated on single crystal copper on (100), (011) and (111) surfaces, using FEA incorporating mesoplasticity constitutive model with a spherical indenter and a Berkovich indenter. Appropriate mesoplastic parameters were determined by combined nanoindentation/FEA approach. Comparison of the results of load-depth curves, deformation patterns, and pile up profiles between nanoindentation tests and FEA results showed reasonably good agreement.

2. At the mesoscale, discrete dislocations were first coupled with GIMP using the principle of superposition (van der Giessen and Needleman, 1995). The scheme was tested with tension and bending. The algorithm was further coupled with MD to formulate a multiscale simulation model and it was used to simulate nanoindentation of (111) copper. Dislocation nucleation and subsequent propagation of dislocations were observed and the drops in the load-displacement curves were correlated to the slippage.

3. At the atomic scale, dynamic friction between two plates of identical material was simulated using the Lennard-Jones (L-J) potential. Parametric studies on the simulation parameters, including the shearing velocity and break radius are conducted through numerical simulations to investigate the frictional behavior at the interface of the two plates. Stick-slip patterns were observed and found to depend on the sliding velocity and state of the interface.

7.2 Multiscale simulation of orthogonal machining

Machining, as one of the primary manufacturing processes to remove materials to shape workpiece to desired geometry and surface finish, is a complex process involving thermal-mechanical interactions between cutting tool and the workpiece. With the emerging global trend toward miniaturization of manufacturing equipment and systems for microscale components and products, there is a global need for scientific understanding of the scaling laws for the design of manufacturing processes/equipment (Ehmann, 2005).

The multiscale modeling scheme was developed and verified in 2D indentation simulations with a wedge indenter in Chapter 5. Other problems, such as metal machining, can be simulated using the multiscale simulation method with the intension of understanding the micromachining using scaling laws. Metal machining is a complex manufacturing process which generally involves large plastic deformation (strain $\gamma \sim 2-5$) as the material undergoing separation from the workpiece, and high temperatures ($\sim 1000^\circ\text{C}$), as a result of friction at the interface of the tool and a workpiece, and plastic energy dissipation as heat. With the advent of effective numerical approaches such as FEM, coupled with emergence of modern computing capability, numerical analysis using

the FEM has been adopted to model metal cutting, as reviewed by van Luttervelt *et al.*(1998). However, FEM has limitations to model large deformations and high strain rates associated with the process, which will cause the background mesh to distort severely.

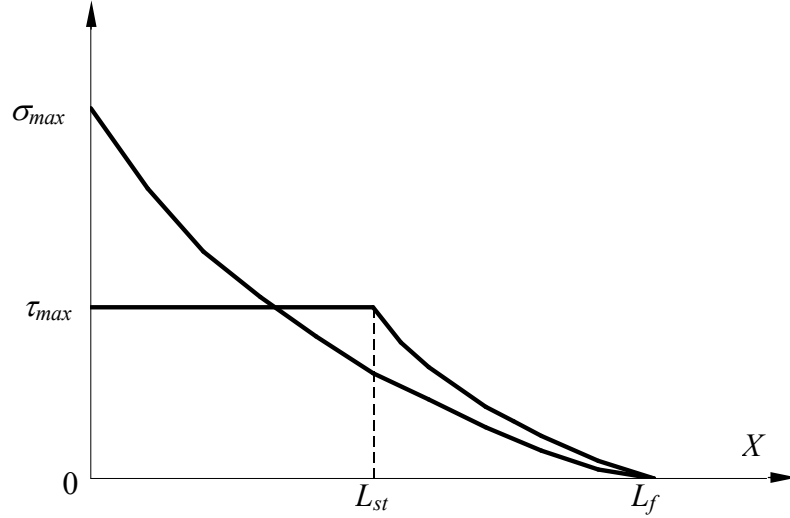


Fig. 7-1: The sticking-sliding friction law

Tool-chip interface friction is one of the most difficult aspects in modeling of the machining process. The sticking-sliding friction states that the tool-chip contact length is divided into two regions, namely, the sticking region ($0 < x \leq L_{st}$) and the sliding region ($L_{st} < x \leq L_f$) (Zorev, 1963), as shown in Fig. 7-1. The shear stress is a constant in the sticking region and the coefficient of friction, μ , is a constant inside the sliding region and it is computed by

$$\mu = \frac{\tau_f}{\sigma_y} \quad (7-1)$$

where τ_f is the shear strength, σ_y is the yield strength. Assuming a power law distribution along the contact surface the normal stress is given by,

$$\sigma(x) = \sigma_{\max} \left[1 - \left(\frac{x}{L_f} \right)^a \right] \quad (7-2)$$

where σ_{\max} is the maximum normal stress, x is the distance along the tool face from the point where the chip begins contact with the tool, L_f is the chip-tool contact length, and a is a constant.

$$\tau_{\max} = \tau_f \quad (7-3)$$

At $x = L_{st}$,

$$\mu\sigma(L_{st}) = \mu\sigma_{\max} \left[1 - \left(\frac{L_{st}}{L_f} \right)^a \right] = \tau_{\max} = \tau_f \quad (7-4)$$

We can get,

$$L_{st} = L_f \cdot \left[1 - \left(\frac{\tau_f}{\mu\sigma_{\max}} \right)^{\frac{1}{a}} \right] \quad (7-5)$$

To find σ_{\max} , first integrate Eq. (7-2) to find the normal force F_n acting on the tool face gives

$$F_n = \int_0^{L_f} w \cdot \sigma(x) dx = \sigma_{\max} L_f \frac{a}{1+a} \quad (7-6)$$

where w is the width of the cut. From Eq. (7-6), we get

$$\sigma_{\max} = \frac{F_n (1+a)}{w \cdot L_f \cdot a} \quad (7-7)$$

Substituting this equation into Eq. (7-5), L_{st} is computed. Then the friction law is given by:

$$\begin{cases} \tau = \tau_{\max} & 0 < x \leq L_{st} \\ \tau(x) = \mu\sigma(x) & L_{st} < x \leq L_f \end{cases} \quad (7-8)$$

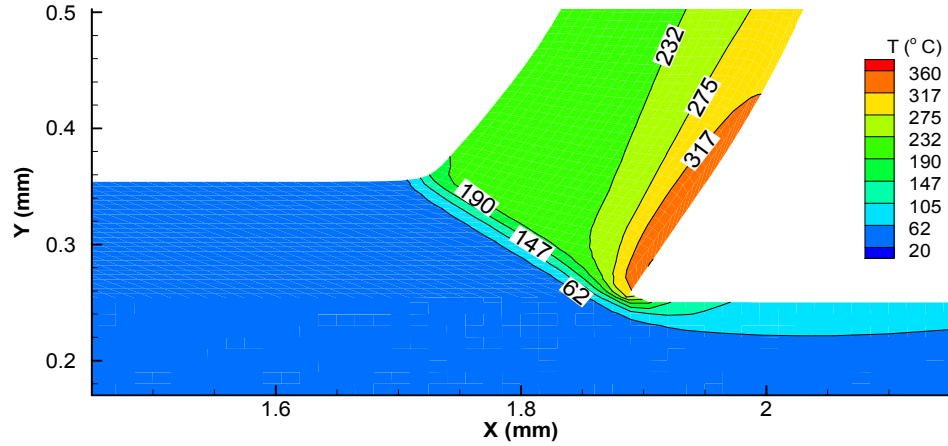


Fig. 7-2: The temperature distribution at the steady state at $\alpha = 33^\circ$, $v = 227$ m/min, $t = 0.1$ mm

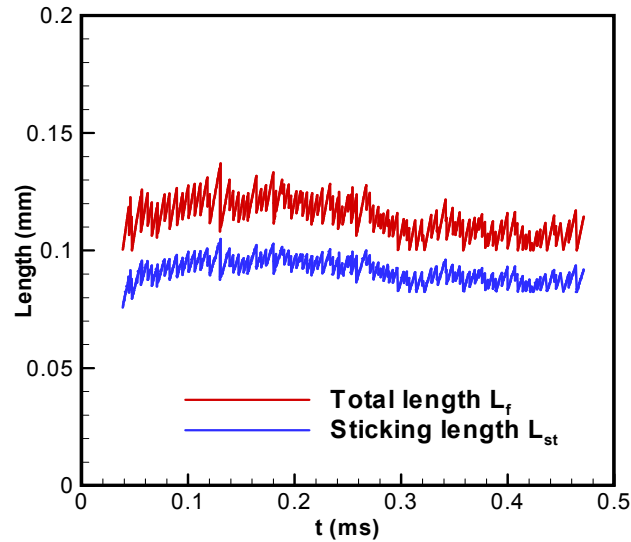


Fig. 7-3: The total contact length and the sticking length at the steady state for $\alpha = 33^\circ$, $v = 227$ m/min, $t = 0.1$ mm

In this investigation, the sticking-sliding friction law was implemented and applied to orthogonal cutting simulations using ABAQUS/Explicit. The contact length and sticking length were computed explicitly based on the theoretical derivation and intermediate contact conditions. The orthogonal cutting operation was simulated in air (under dry condition). The work material was AISI 1015 steel; the cutting speed 227

m/min, and depth of cut 0.1 mm and the rake angle α 33°. Temperature distribution is shown in Fig. 7-2, and the calculated sticking and sliding lengths are given in Fig. 7-3.

With the understanding of the sliding-sticking friction law using FEM, the friction law can be implemented into GIMP. MD simulation can model the material behavior accurately, if the potential function is appropriate. However, the modeling size is generally limited to the order of a few nanometers based on the current computer capability. With the multiscale modeling technique, the area in the vicinity of the tool tip can be modeled using MD and the rest of area can be modeled using GIMP and DD, as shown schematically in Fig. 7-4. This way, the advantages of MD simulation are preserved and the simulation time is affordable. In addition, GIMP is especially suitable for coping with large deformations associated with metal cutting because of the use of Lagrangian description for material points carrying physical quantities and the use of Eulerian description for convection of physical variables and solution of field equations. With DD, the dislocation nucleation mechanism at the tool tip and its propagation into the workpiece can be better understood.

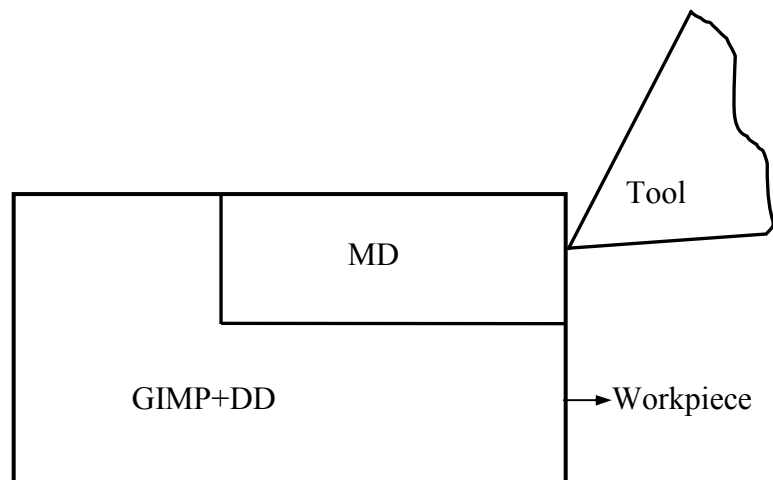
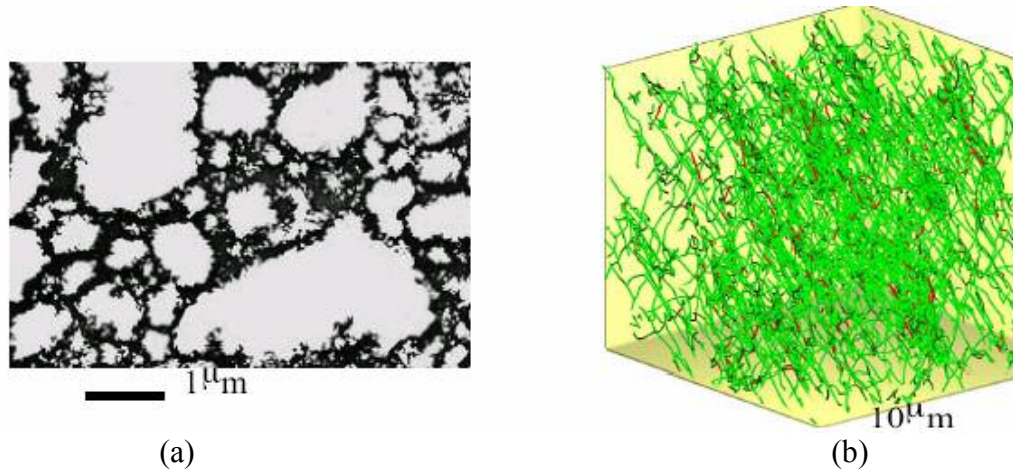


Fig. 7-4: Schematic of the setup of the orthogonal metal cutting

7.3 Extension of multiscale simulation to 3D

The 2D multiscale simulation algorithm that couples molecular dynamics (MD), discrete dislocations (DD) and GIMP can be extended into 3D. 3D GIMP and MD are readily available with the literature and 3D discrete dislocation modeling can be conducted with ParaDiS (Parallel Dislocation Dynamics Simulator), which is a massively parallel dislocation dynamics simulation code developed at the Lawrence Livermore National Laboratory. ParaDiS is specifically designed for investigating the collective behavior of large number of dislocation lines as required for understanding and accurate prediction of plasticity and strength in crystals. Fig. 7-5 shows a numerical example from ParaDiS of experimental and simulated dislocation microstructure.



(a) (b)
Fig. 7-5: Simulated dislocation microstructure (a) Dislocation microstructure developed in copper during plastic deformation, as observed in an electron microscope. Dark regions contain large number of dislocation lines, whereas light regions contain no dislocations. (b) Dislocation microstructure developed during plastic deformation in a dislocation dynamics simulation by ParaDiS (Bulatove, *et al.*, 2004)

It may however be noted that the computational cost for 3D simulations is significantly higher than for 2D. Parallel computing becomes very important and its effectiveness can sometimes determine the overall performance of the multiscale

simulation algorithm. To enhance the multiscale simulation algorithm at 3D, the following two approaches can be taken:

Dynamic multiscale refinement: This refinement includes two aspects. The first one is to refine and coarsen the continuum region (GIMP) dynamically during the simulation. Strain gradient criterion can be used in this case. The second one is to refine between GIMP and the MD atoms. Since the MD part of the simulation takes a large portion of the time and resources, the region away from the area of interest can be dynamically merged, i.e., equivalent GIMP particles are created and the atoms are deleted. GIMP particles can also be replaced by equivalent atoms, if necessary.

Dynamic load balancing: As the computational domain is dynamically refined and coarsened, each processor's computational load will change significantly, if the load is not balanced dynamically. SAMRAI provides an excellent interface to dynamic load balancing at the continuum level. The atom storage can also be moved to SAMRAI so that load balancing can be done within the same framework.

References

- ABAQUS User's Manual, 2003. Version 6.4, ABAQUS, Inc.
- Alder, B. and Wainwright, T., 1959. Studies in molecular dynamics: I. General method, J. Chem. Phys. 31 (2), 459.
- Allen, M.P. and Tildesley, D.J., 1989. Computer Simulation of Liquids, Oxford University Press.
- Amodeo, R. J. and Ghoniem, N. M., 1990. Dislocation dynamics. I. A proposed methododloty for deformation micromechanics. Phys. Rev. B, 41, 6958-6966.
- Asaro, R. J. and Needleman, A., 1985. Overview no. 42 Texture development and strain hardening in rate dependent polycrystals. Acta Metall., 33, 923-953.
- Bahr, D. F., Kramer, D. E., Gerberich, W. W., 1998. Non-linear deformation mechanisms during nanoindentation. Acta Mater., 46(10), 3605-3617.
- Bardenhagen, S. G. and Kober, E. M., 2004. The generalized interpolation material point method. Computer Modeling in Engineering & Sciences, 5(6), 477-496.
- Bassani, J. L. and Wu, T.-Y., 1991. Latent hardening in single crystals II. Analytical characterization and predictions. Philos. Trans. Roy. Soc. London A, 435, 21-41.
- Begley, M. R., Hutchinson, J. W., 1998. Mechanics of size-dependent indentation. J. Mech. Phys. Solids, 46(10), 2049-2068.
- Belytschko, T., Liu, W. K. and Moran, B., 2000. Nonlinear Finite Elements for Continua and Structures, John Wiley & Sons.
- Bernstein, N., Aziz, M. J. and Kaxiras, E., 2000. Atomistic simulations of solid-phase epitaxial growth in silicon. Phys. Rev. B, 61(10), 6696-6700.
- Brenner, D.W., Harrison, J.A., White, C.T. and Colton, R.J., 1991. Molecular dynamics simulations of the nanometer-scale mechanical properties of compressed Buckminsterfullerene. Thin Solid Films, 206, 220-223.
- Bulatov, V., Cai, W., Wei Cai, Fier, J., Hiratani, M., Hommes, G., Pierce, T., Tang, M., Rhee, M., Yates, K., Arsenlis, T., 2004, Scalable Line Dynamics in ParaDiS. Proceedings of the 2004 ACM/IEEE conference on Supercomputing.

- Cleveringa, H.H.M., van der Giessen, E. and Needleman, A. Discrete dislocation analysis of bending. *Int. J. Plast.*, 15(8), 1999, 837-868.
- Christopher, D., Kenny, S., Smith, R., Richter, A., Wolf, B. and King, B., 2003. Anisotropy of nanoindentation — A tool for the determination of nanocrystal orientation? *Mater. Res. Soc. Symp. Proc.*, 779, 147-152.
- Coker, D. Lykotrafitis, G. Needleman, A. and Rosakis, A.J., 2005. Frictional sliding modes along an interface between identical elastic plates subject to shear impact loading. *J. Mech. Phys. Solids* 53 (4), 884-922.
- Daw, M.S. and Baskes, M.I., 1984. Embedded-atom method: derivation and application to impurities, surfaces, and other defects in metals. *Phys. Rev. B*, 29, 6443-6453.
- Djuidje Kenmoe, G. and Kofane, T.C., 2007. Frictional stick-slip dynamics in a nonsinusoidal Remoissenet-Peyrard potential. *European Physical Journal B*, 55(4), 347-354.
- Duan, D. M., Wu, N. Q. Slaughter, W. S. Mao, Scott X., 2001. Length scale effect on mechanical behavior due to strain gradient plasticity. *Mater. Sci. Eng. A* 303, 241-249.
- Elmustafa, A. A. and Stone, D. S., 2003a. Size-dependent hardness in annealed and work hardened α -brass and aluminum polycrystalline materials using activation volume analysis. *Mater. Lett.*, 57, 1072-1078.
- Elmustafa, A .A. and Stone, D. S., 2003b. Nanoindentation and the indentation size effect: Kinetics of deformation and strain gradient plasticity. *J. Mech. Phys. Solids*, 51(2), 357-381.
- Fang, X. F. and Dahl, W., 1993. Investigation of the formation of dislocation cell structures and the strain hardening of metals by computer simulation. *Mater. Sci. Eng. A* 164, 300-305.
- Feng, G., Ngan, A. H. W., 2001. Creep and strain burst in indium and aluminum during nanoindentation. *Scripta Mater.*, 45(8), 971-976.
- Fivel, M. C., Robertson, C. F., Canova, G. R., and Boulanger, L., 1998. Three-dimensional modeling of indent-induced plastic zone at a mesoscale. *Acta Mater.*, 46, 6183-6194.

- Fleck, N. A. and Hutchinson, J. W., 1993. Phenomenological theory for strain gradient effects in plasticity. *J. Mech. Phys. Solids*, 41(12), 1825-1857.
- Fleck, N. A., Muller, G. M., Ashby, M. F. and Hutchinson, J. W., 1994. Strain gradient plasticity: theory and experiment. *Acta Metall. Mater.*, 42, 475-487.
- Flom, D. G. and Komanduri, R., 2002. Some indentation and sliding experiments on single crystal and polycrystalline materials. *Wear*, 252, 401-429.
- Fusenig, K. D., Nembach, E., 1975. Dynamic dislocation effects in precipitation hardened materials. *Acta Metall. Mater.*, 41, 3181-3189.
- Gaillard, Y. , Tromas, C., Woirgard, J., 2003. Study of the dislocation structure involved in a nanoindentation test by atomic force microscopy and controlled chemical etching. *Acta Mater.*, 51(4), 1059-1065.
- Gambin, W., Barlat, F., 1997. Modeling of deformation texture development based on rate independent crystal plasticity. *Int. J. of Plasticity* 13, 75-85.
- Gouldstone, A., Koh, H. J., Zeng, K. Y., Giannakopoulos, A. E. and Suresh, S., 2000. Discrete and continuous deformation during nanoindentation of thin films. *Acta Mater.*, 48(9), 2277-2295.
- Grillo, S. E., Ducarroir, M., Nadal, M., Tournie, E. and Faurie, J.-P., 2003. Nanoindentation of Si, GaP, GaAs and ZnSe single crystals. *J. Phys. D: Appl. Phys.*, 36(1), L5-L9.
- Groenou, V., Broese, A., and Kadijk, S. E., 1989. Slip patterns made by sphere indentations on single crystal MnZn ferrite. *Acta Metall.*, 37(10), 2613-2624.
- Groma, I. and Pawley, G. S., 1993. Role of the secondary slip system in a computer simulation model of the plastic behaviour of single crystals. *Mater. Sci. Eng. A* 164, 306-311.
- Gulluoglu, A. N., Hartley, C. S., 1993. Simulation of dislocation microstructures in two dimensions: II. Dynamic and relaxed structures. *Model. Simul. Mater. Sci. Eng.*, 1, 383-402.
- Hartley, C. S., 2003. A method for linking thermally activated dislocation mechanisms of yielding with continuum plasticity theory. *Philos. Mag.*, 83, 3783-3808.

- Hill, R. and Rice, J. R., 1972. Constitutive analysis of elastic-plastic crystals at arbitrary strain. *J. Mech. Phys. Solids*, 20, 401-413.
- Hirth, J. P. and Lothe, J., 1982. *Theory of Dislocations*. John Wiley & Sons, 2nd ed.
- Holian, B. L., Hammerberg, J. E. and Lomdahl, P. S., 1998. The birth of dislocations in shock waves and high-speed friction. *Journal of Computer-Aided Materials Design*, 5, 207-224.
- Huang, Y., 1991. A user-material subroutine incorporating single crystal plasticity in the ABAQUS finite element program. Mech. Report 178, Division of Applied Sciences, Harvard University, Cambridge, MA.
- Hutchinson, J. W., 1976. Bounds and self-consistent estimates for creep of polycrystalline materials. *Proc. Roy. Soc. London A*, 348, 101-127.
- Hutchinson, J. W., 2000. Plasticity at the micron scale. *Int. J. Solids Structures*, 37, 225-238.
- Jang, S. and Voth, G. A., 1997. Simple reversible molecular dynamics algorithms for Nosé-Hoover chain dynamics, *J. Chem. Phys.*, 107(22), 9514-9526.
- Kalidindi, S. R., Bronkhorst, C. A., and Anand, L., 1992. Crystallographic texture evolution during bulk deformation processing of FCC metals. *J. Mech. Phys. Solids*, 40, 537-569.
- Khan, M. Y., Brown, L. M., Chaudhri, M. M., 1992. Effect of crystal orientation on the indentation cracking and hardness of MgO single crystals. *J. Phys. D: Appl. Phys.*, 25(1A), A257-A265.
- King, W. E., Campbell, G., Gonis, T., Henshall, G., Lesuer, D., Zywickz, E., and Foiles, S., 1995. Theory, simulation, and modeling of interfaces in materials — bridging the length-scale gap: a workshop report. *Mater. Sci. Eng. A*, 191, 1-16.
- Komanduri, R., Chandrasekaran, N. and Raff, L. M., 2000. MD simulation of indentation and scratching of single crystal aluminum. *Wear*, 240, 113-143.
- Krupkowski, A., 1931. A. Proprietes Mecaniques du Cuivre. *Rev. Metall.*, 28, 641-652.
- Kubin, L. P. and Canova, G., 1992. The modelling of dislocation patterns. *Scripta Metall.* 27, 957-962.

- Kum, O., 2005. Orientation effects of elastic-plastic deformation at surfaces: nanoindentation of nickel single crystals. *Molecular Simulation*, 31, 115-121.
- Kysar, J. W., 2001. Continuum simulations of directional dependence of crack growth along a copper/sapphire bicrystal interface. Part I: Experiments and crystal plasticity background. *J. Mech. Phys. Solids*, 49, 1099-1128.
- Lee, W. B., To, S. and Cheung, C. F., 2000. Effect of crystallographic orientation in diamond turning of copper single crystals. *Scripta Mater.*, 42(10), 937-945.
- Liang, H., Woo, C. H., Huang, H., Ngan, A. H. W. and Yu, T. X., 2004. Crystalline plasticity on copper (001), (110), and (111) surfaces during nanoindentation. *CMES - Computer Modeling in Engineering and Sciences*, 6(1), 105-114.
- Lim, Y. Y., Bushby, A. J., and Chaudhri, M. M., 1998. Nano and macro indentation studies of polycrystalline copper using spherical indenters. *Mater. Res. Soc. Symp. Proc.*, 522, 145-150.
- Lim, Y. Y. and Chaudhri, M. M., 1999. The effect of the indenter load on the nanohardness of ductile metals: An experimental study on polycrystalline work-hardened and annealed oxygen-free copper. *Philos. Mag. A*, 79, 2979-3000.
- Lim, Y. Y. and Chaudhri, M. M., 2002. The influence of grain size on the indentation hardness of high-purity copper and aluminum. *Philos. Mag. A*, 82, 2071-2080.
- Liu, Y., Wang, B., Yoshino, M., Roy, S., Lu, H. and Komanduri, R., 2005. Combined numerical simulation and nanoindentation for determining mechanical properties of single crystal copper at mesoscale. *J. Mech. Phys. Solids*, 53(12), 2718-2741.
- Lu, H., Daphalapurkar, N. P., Wang, B., Roy, S., Komanduri, R., 2006. Multiscale simulation from atomistic to continuum - Coupling molecular dynamics (MD) with the material point method (MPM). *Phil. Mag.* 86 (20), 2971-2994.
- Ma, J., Lu, H., Wang, B., Hornung, R., Wissink, A. and Komanduri, R., 2006. Multiscale simulation using generalized interpolation material point (GIMP) method and molecular dynamics (MD). *Computer Modeling in Engineering & Sciences*, in press.
- Ma, J., Lu, H., Wang, B., Roy, S., Hornung, R., Wissink, A. and Komanduri, R., 2005. Multiscale simulations using generalized interpolation material point (GIMP) method

- and SAMRAI parallel processing. *Computer Modeling in Engineering & Sciences*, 8(2), 135-152.
- McElhaney, K. W., Vlassak, J. J., and Nix, W. D., 1998. Determination of indenter tip geometry and indentation contact area for depth-sensing indentation experiments. *J. Mater. Res.*, 13, 1300-1306.
- Meyer, E., 1908. Untersuchen ueber Haertepruefung und Haerte. *Z. Ver. Deutsche Ing.*, 52, 645-654.
- Nakamachi, E., Xie, C. L., Morimoto, H., Morita, K., Yokoyama, N., 2002. Formability assessment of FCC aluminum alloy sheet by using elastic/crystalline viscoplastic finite element analysis. *Int. J. of Plasticity* 18(6), 617-632.
- Needleman, A., 2000. Computational mechanics at the mesoscale. *Acta Mater.*, 48, 105-124.
- Nibur, K. A. and Bahr, D. F., 2003. Identifying slip systems around indentations in FCC metals. *Scripta Mater.*, 49 (11), 1055-1060.
- Nix, W. D. and Gao, H., 1998. Indentation size effects in crystalline materials: a law for strain gradient plasticity. *J. Mech. Phys. Solids*, 8, 411-425.
- Ogata, S., Lidorikis, E., Shimojo, F., Nakano, A., Vashishta, P., and Kalia, R., 2001. Hybrid finite-element/molecular-dynamics/electronic-density-functional approach to materials simulations on parallel computers. *Computer Phys. Commu.*, 138, 143-154.
- Ohzono, T. and Fujihira, M., 2000. Effect of an atomic scale protrusion on a tip surface on molecular stick-slip motion and friction anisotropy in friction force microscopy. *Japanese Journal of Applied Physics, Part 1: Regular Papers and Short Notes and Review Papers*, 39(10), 6029-6034.
- Oliver, W. C. and Pharr, G. M., 1992. An improved technique for determining hardness and elastic modulus using load and displacement sensing indentation experiments. *J. Mater. Res.*, 7, 1564-1583.
- Peirce, D., Asaro, R. J., and Needleman, A., 1982. An analysis of nonuniform and localized deformation in ductile single crystals. *Acta Metall.*, 30(6), 1087-1119.
- Peirce, D., Asaro, R. J., and Needleman, A., 1983. Material rate dependence and localized deformation in crystalline solids. *Acta Metall.*, 31, 1951-1976.

- Peralta, P., Ledoux, R., Dickerson, R., Hakik, M. and Dickerson, P., 2004. Characterization of surface deformation around Vickers indents in monocrystalline materials. *Metallurgical and Materials Transactions A: Physical Metallurgy and Materials Science*, 35(8), 2247-2256.
- Perry, M.D. and Harrison, J.A., 1995. Universal aspects of the atomic-scale friction of diamond surfaces. *Journal of Physical Chemistry*, 99(24), 9960-9965.
- Pharr, G. M., Tsui, T. Y. and Oliver, W. C., 1996. Indenter geometry effects on the measurement of mechanical properties by nanaindentation with sharp indenters. Report number A103233.
- Plimpton, S.J., 2005. Documentation for the LAMMPS Molecular Dynamics Simulator, Sandia National Laboratory.
- Poole, W. J., Ashby, M. F. and Fleck, N. A., 1996. Micro-hardness of annealed and work-hardened copper polycrystals. *Scripta Mater.*, 34(4), 559-564.
- Raffi-Tabar, H., Hua, L. and Cross, L., 1998. A multi-scale atomistic-continuum modeling of crack propagation in a two-dimensional macroscopic plate. *Journal of Physics: Condensed Matter*, 10, 2375-2387.
- Saha, R. and Nix, W. D., 2002. Effects of the substrate on the determination of thin film mechanical properties by nanoindentation. *Acta Mater.*, 50(1), 2002, 23-38.
- Saraev, D and Miller, R. E., 2006. Atomic-scale simulations of nanoindentation-induced plasticity in copper crystals with nanometer-sized nickel coatings. *Acta Mater.*, 54(1), 33-45.
- Schmid, E., 1931. Beiträge zur Physik und Metallographie de Magnesiums. *Z. Electrochem.* 37, 447-459.
- Shaw, M. C., and DeSalvo, G. J., 1972. The role of elasticity in hardness testing. *Metals Engineering Quarterly*, 12, 1-7.
- Shenoy, V. B., Miller, R., Tadmor, E. B., Rodney, D., Phillips, R., and Ortiz, M., 1999. Adaptive finite element approach to atomic-scale mechanics — the quasicontinuum method. *J. Mech. Phys. Solids*, 47, 611-642.

- Shiari, B.; Miller, R.E.; Curtin, W.A., 2005. Coupled atomistic/discrete dislocation simulations of nanoindentation at finite temperature. *Journal of Engineering Materials and Technology*. Transactions of the ASME, 127 (4), 358-368.
- Shilkrot, L. E., Curtin, W. A., and Miller, R. E., 2002. A coupled atomistic/continuum model of defects in solids. *J. Mech. Phys. Solids*, 50, 2085-2106.
- Shilkrot, L. E., Miller, R. E. and Curtin, W. A., 2004. Multi-scale plasticity modeling: coupled atomistics and discrete dislocation mechanics. *J. Mech. Phys. Solids*, 52, 755-787.
- Shimizu, J., Eda, H. Yoritsune, M. and Ohmura, E., 1998. Molecular dynamics simulation of friction on the atomic scale. *Nanotechnology*, 9(2), 118-123.
- Shu, J. Y. and Fleck, N. A., 1998. The prediction of a size effect in micro indentation. *Int. J. Solids Structures*, 35, 1363-1383.
- Smith, G. S., Tadmor, E. B., Bernstein, N., and Kaxiras, E., 2001. Multiscale simulations of silicon nanoindentation. *Acta Mater.*, 49, 4089-4101.
- Stelmashenko, N. A., Walls, M. G., Brown, L. M. and Milman, Y. V., 1993. Microindentations on W and Mo oriented single crystals: An STM study. *Acta Metall. Mater.*, 41(10), 2855-2865.
- Sulsky, D. and Schreyer, H. L., 1996. Axisymmetric foam of the material point method with applications to upsetting and Taylor impact problems. *Computer Methods in Applied Mechanics and Engineering*, 139, 409-429.
- Sulsky, D., Zhou, S. J. and Schreyer, H. L., 1995. Application of a particle-in-cell method to solid mechanics. *Computer Phys. Commu.*, 87, 236-252.
- Taylor, G. I. and Elam, C. F., 1923. The distortion of an aluminum crystal during a tensile test. *Proc. Roy. Soc. London A*, 102, 643-667.
- Tsuru, T., Shibutani, Y., 2007. Anisotropic effects in elastic and incipient plastic deformation under (001), (110), and (111) nanoindentation of Al and Cu. *Phys. Rev. B* 75 (3): Art. No. 035415.
- Tymiak, N. I., Kramer, D. E., Bahr, D. F., Wyrobek, T. J., Gerberich, W.W., 2001. Plastic strain and strain gradients at very small indentation depths. *Acta Mater.*, 49(6), 1021-1034.

- van der Giessen, E. and Needleman, A., 1995. Discrete dislocation plasticity: a simple planar model. *Model. Simul. Mater. Sci. Eng.*, 3, 689-735.
- Vlassak, J., and Nix, W. D., 1994. Measuring the elastic properties of anisotropic materials by means of indentation experiments. *J. Mech. Phys. Solids*, 42(8), 1223-1245.
- Wang, Y., Raabe, D., Kluber, C., and Roters, F., 2004. Orientation dependence of nanoindentation pile-up patterns and of nanoindentation microtextures in copper single crystals. *Acta Mater.*, 52, 2229-2238.
- Wei, Y., Shu, S., Du, Y., Zhu, C., 2005. Size, geometry and nonuniformity effects of surface-nanocrystalline aluminum in nanoindentation test. *Int. J. of Plasticity* 21(11), 2089-2106.
- Xu, Z. and Rowcliffe, D., 2002. Method to determine the plastic properties of bulk materials by nanoindentation. *Philos. Mag. A*, 82(10), 1893-1901.
- Yoshino, M., Shiina, T., and Shirakashi, T., 1997. FEM simulation of dislocation behavior in an FCC metal. *Computer Modeling and Simulation in Engineering*, 2, 218-226.
- Yoshino, M., Aoki, T., Chandrasekaran, N., Shirakashi, T., and Komanduri, R., 2001. Finite element simulation of plane strain plastic-elastic indentation on single crystal silicon. *Int. J. Mech. Sci.*, 43, 313-333.
- Yoshino, M., 2003. Theory of mesoplasticity. Unpublished.
- Zbib, H.M. and Diaz de la Rubia, T., 2002. A multiscale model of plasticity. *Int. J. Plast.*, 18(9), 1133-1163.
- Zbib, H. M., Rhee, M. and Hirth, J. P., 1998. On plastic deformation and the dynamics of 3D dislocations. *Int. J. Mech. Sci.*, 40, 113–127.
- Zhang, Y. W. and Bower, A. F., 1999. Numerical simulations of island formation in a coherent strained epitaxial thin film system. *J. Mech. Phys. Solids*, 1999, 47, 2273-2297.
- Zhu, T., Li, J., Van, V., Krystyn, J., Ogata, S., Yip, S., and Suresh, S., 2004. Predictive modeling of nanoindentation-induced homogeneous dislocation nucleation in copper. *J. Mech. Phys. Solids*, 52(3), 691-724.

- Zimmerman, J. A., Kelchner, C. L., Klein, P.A., Hamilton, J. C. and Foiles, S. M., 2001. Surface Step Effects on Nanoindentation. *Phys. Rev. Lett.*, 87(16), 165507-1-165507-4.
- van Luttervelt, C. A., Childs, T. H. C., Jawahir, I. S., Klocke, F. and Venuvinod, P. K., 1998. Present situation and future trends in modeling of machining operations. Progress report of the CIRP working group “Modeling of Machining Operations”. *CIRP Annals — Manufacturing Technology*, 47(2), 587-626.

VITA

Yang Liu

Candidate for the Degree of
DOCTOR OF PHILOSOPHY

Thesis: MULTISCALE MODELING AND SIMULATION: INCORPORATION OF
MESOPLASTICITY BETWEEN ATOMISTIC AND CONTINUUM

Major Field: Mechanical Engineering

Biographical:

Education: Received Bachelor of Engineering degree in Mechanical Engineering from Wuhan University of Technology in Wuhan, Hubei Province, P. R. China, in June 2000; received Master of Science degree with a major in Mechanical Engineering at Wuhan University of Technology in Wuhan, Hubei Province, P. R. China, in June 2003; completed Doctor of Philosophy degree with a major in Mechanical Engineering at Oklahoma State University in August, 2007.

Experience: Employed by Oklahoma State University, School of Mechanical and Aerospace Engineering as a graduate research assistant and teaching assistant, from August 2003 to present.

Name: Yang Liu

Date of Degree: December, 2007

Institution: Oklahoma State University

Location: Stillwater, Oklahoma

Title of Study: MULTISCALE MODELING AND SIMULATION: INCORPORATION
OF MESOPLASTICITY BETWEEN ATOMISTIC AND CONTINUUM

Pages in Study: 142

Candidate for the Degree of Doctor of Philosophy

Major Field: Mechanical Engineering

Scope and Method of Study: In the framework of multiscale modeling, two modeling techniques at the meso/micro scale, namely, mesoplasticity and discrete dislocation are employed to study the mechanical behavior of single crystal materials under nanoindentation. A combined finite element method (FEM)/nanoindentation approach has been developed to determine the material behavior of single-crystal copper incorporating the mesoplastic constitutive model. Nanoindentation on a single-crystal copper was modeled using mesoplasticity. Numerical and experimental investigations of nanoindentation on single-crystal copper in three crystallographic orientations, i. e., (100), (011) and (111) using a spherical indenter (3.4 μm radius) and a Berkovich indenter were reported. Discrete dislocations are coupled with GIMP using the principle of superposition (van der Giessen and Needleman, 1995). Simulations of indentation were performed on the (111) plane of copper using a wedge indenter. The effects of temperature on the indentation load-depth curves and nucleation of dislocations were investigated.

Findings and Conclusions: Nanoindentation on a single-crystal copper was modeled using mesoplasticity with a user subroutine in ABAQUS/Explicit software. For a spherical nanoindentation, distribution of the out-of-plane displacements at three crystallographic orientations, namely, (100), (011), and (111) show pile-ups with a topographical pattern of four-fold, two-fold, and three-fold symmetry, respectively in both experiments and simulations. No sink-in was observed due to the work hardened condition of the specimens. Furthermore, the comparisons between the nanoindentation and simulation on load-displacement relations and the pile-up profiles were found to be reasonably good, lending further credibility on the capability of the current model. It is concluded that the numerical model with the parameters determined is capable of predicting the single-crystal copper behavior of three orientations under nanoindentation. A multiscale simulation algorithm that couples MD, DD, and GIMP was developed and used to simulate the indentation on Cu (111) plane with a wedge indenter. Dislocation nucleation and subsequent propagation of dislocations are observed for the indentation simulation.

Advisor's Approval: Ranga Komanduri
